Installation and Maintenance of Weather Stations on High Voltage Pylons Using Unmanned Aerial Vehicles (UAV)

Zur Erlangung des akademischen Grades eines

DOKTORS DER INGENIEURWISSENSCHAFTEN
(Dr.-Ing.)

von der KIT-Fakultät für
Elektrotechnik und Informationstechnik
des Karlsruher Instituts für Technologie (KIT)

genehmigte

DISSERTATION

von

M.Sc. Na Shen
geb. in Shaanxi Provinz, VR China

Tag der mündlichen Prüfung:	11.11.2024
Hauptreferent:	Prof. Dr. rer. nat Wilhelm Stork
Korreferent:	Prof. Dr. rer. nat. Cornelius Neumann

Acknowledgments

Upon completing my master's degree at the Karlsruhe Institute of Technology, I faced a period of uncertainty regarding whether to pursue a career in industry or academia. It was during this time that I became actively involved in the field of scientific research through my role as a student assistant. This experience ignited my passion for scientific inquiry. Despite experiencing homesickness and a deep longing for family reunions while living in Germany, my parents wholeheartedly supported my decision to pursue a PhD. Their unwavering encouragement and love provided me with the strength to embark on this challenging journey, even though it meant several more years of separation from them.

First and foremost, I would like to express my deepest gratitude to my doctoral advisor, Prof. Dr. Wilhelm Stork (Willy), for affording me the invaluable opportunity to engage in this research journey. His patient guidance, countless discussions, and insightful suggestions on scientific research, physics, society, history, and everyday life have not only shaped my understanding of problem-solving but have also enriched my knowledge of the world at its core. These experiences have left an indelible mark on me and will continue to benefit me throughout my lifetime. Words alone cannot adequately convey the extent of my appreciation.

Furthermore, I extend my heartfelt appreciation to the "PrognoNetz" team at the Institut für Technik der Informationsverarbeitung (ITIV). Dr. Gabriela Molinar not only provided me with the initial opportunity to work as a Hiwi but also wholeheartedly recommended me for a doctoral position. Her unwavering support throughout the project, along with her guidance and mentorship, have been instrumental in my research journey. I would also like to acknowledge Mr. Christos Klamouris for his invaluable assistance in the project, including his help with the project report and his insightful discussions and advice on my research. Lastly, I express my gratitude to Mr. Lintao Toni Fan, a brilliant and creative colleague, for his outstanding contributions to the team.

I'm deeply grateful to my husband, Haohao Hu, for his unwavering support, both in my academic and daily life. His valuable scientific insights, discussions, and suggestions have been instrumental in shaping my research. This support has been particularly significant during the final phase of my doctoral journey, as I tackled the challenging task of writing this dissertation while also expecting our child. I would also like to take a moment to express my heartfelt gratitude to my daughter Emily. Her peaceful nights of sleep, sweet smiles, and warm hugs have been a constant source of encouragement and motivation throughout my journey to complete my PhD. Their unwavering belief in me has been a driving force behind my accomplishments.

Additionally, I would like to express my gratitude for the collaboration with students working on their bachelor's and master's theses or as research assistants. This partnership has been mutually beneficial, fostering valuable discussions and sparking inspiration. It has also significantly expedited the completion of work packages within projects and research topics.

Finally, I extend my gratitude for the financial support provided by the German Federal Ministry of Economic Affairs and Energy (BMWi) within the framework of the PrognoNetz project. This collaboration has been a highly successful partnership between KIT and industry partner companies, including UBIMET GmbH, Wilmers Messtechnik GmbH, unilab AG, Transnet BW GmbH, and GWU-Umwelttechnik GmbH.

Kurzfassung

Der rasante Zuwachs der dezentralisierten erneuerbaren Energieerzeugung - Windenergie im norden Deutschland, Photovoltaik im Süden - zusammen mit dem wachsenden internationalen Energiehandel stellt die Übertragungsnetzbetreiber vor Herausforderungen - Netzengpässe. Um die temporäre Abschaltung der Erneuerbare-Energien-Anlagen zu verhindern sowie die Übertragungssicherheit sogar beim höhen Energiebedarf zu gewährleisten, ist ein erheblicher Ausbau des Übertragungsnetzes erforderlich. Im Rahmen von PrognoNetz wird ein wetterabhängiges Überwachungssystem als kurzfristige Lösung entwickelt, das die Möglichkeit bietet, die vorhandene Netzinfrastruktur effizienter zu nutzen. Ein selbstlernendes Sensornetzwerk ermöglicht die Steigerung der Übertragungskapazität durch die Modellierung des lokalen Kühleffekts und der Wetterbedingungen entlang der Übertragungsleitungen sowie die Prognose der Strombelastbarkeit basierend auf historischen Wettermessungen.

Diese Dissertation präsentiert einen systematischen Ansatz für die methodische Installation und Wartung eines Wetter-Sensornetzwerks im Stromnetz unter Einsatz von unbemannten Luftfahrzeugen (UAVs), um den Verteilungsprozess zu beschleunigen. Der Entwurf und die Konstruktion der mechanischen Befestigung der Sensorausrüstung sowie die Implementierung eines adaptiven Greifsystems am UAV ermöglicht die Installation von Wetterstationen an Übertragungsmasten in Höhe der Hochspannungsleitungen und mindern die vorübergehende Abschaltung der Übertragungeinrichtungen im Vergleich zum direkten Installtionsbetrieb auf den Leitungen. Die Machbarkeit dieser Konzepte wird durch umfangreiche Laborversuche und Feldtests eingehend überprüft und verbessert. Vor dem Einbau wurde ein photovoltaik basiertes, autarkes Stromversorgungssystem für die drahtlose Wettermessung entworfen, so dass die Messeinheit in den strahlungsärmeren Monate und sogar Autonomietage ohne Energiezufuhr überstehen kann. Dies wurde durch die Ermittlung der optimalen Azimut- und Neigungswinkel der Solarpaneele unter Berücksichtigung lokaler und historischer Metadaten der Sonneneinstrahlung erzielt. Jedoch hat sich gezeigt, dass die Schwebegenauigkeit des Fahrzeugs für die Bestimmung der Betriebszeit in den Feldversuchen von wesentlicher Bedeutung ist. Daher wurde ein semi-autonomes Flugsteuerungssystem eingesetzt, um das technische Personal während des Betriebs zu unterstützen und das Schwebeflugmanöver des Fahrzeugs gegen Windstörungen zu verbessern. Ein GPS-basiertes Navigationssystem ist vorteilhaft, um die Orientierung und die Entfernung zum Zielort unter Berücksichtigung der Hindernisvermeidungsfunktion einzustellen und zu überprüfen. Eine autonome Erkennung des Strommasts und die Anpassung der Flugsteuerung, um die vorgegebene Installationsposition auf einem der Mastfußeckstiele anzusteuern, bietet eine gute Führung für den Piloten in homogenen Umgebung. Der Erkennungs- und Flugsteuerungsalgorithmus zum Aufstellen und Abholen der Wetterstation für Reparatur- oder Erweiterungszwecken wurde fieldversucht und optimiert. Der Automatisierungsprozess macht die Verteilung und Wartung des Sensornetzes über tausende von Kilometern effizienter, mit der hohen Flexibilität kann der Zeit- und Personalaufwand um mindestens 50% reduziert werden, insbesondere bei schwer zugänglichen Installationsorten.

Abstract

The rapid increase in decentralized renewable energy production, such as wind energy in northern Germany and photovoltaics in the south, combined with the growing international energy trade, presents a significant challenge for transmission system operators - grid congestion. To avert the curtailment of renewable energy plants and ensure transmission security, especially during periods of high supply, substantial expansion of the transmission grid becomes imperative. In response to this issue, the PrognoNetz initiative aims to develop a weather-dependent monitoring system as a short-term solution, enabling efficient utilization of the existing grid infrastructure. This system incorporates a self-learning sensor network capable of modeling the cooling effect on transmission lines based on ambient weather conditions. Furthermore, it facilitates capacity forecasting by analyzing historical weather measurements, thereby enhancing transmission capacity planning and management.

This dissertation presents a methodical approach for the systematic installation and maintenance of a weather sensor network in the electrical grid, leveraging Unmanned Aerial Vehicles (UAVs) to expedite the distribution process. The design and construction of mechanical attachments for sensor equipment, along with the implementation of an adaptive gripper system on the UAV, facilitate the installation of weather stations on transmission towers at the height of high-voltage lines, mitigating the risk of temporary shutdown of transmission facilities as opposed to direct operation on conductors. The feasibility of these concepts is rigorously verified and enhanced through labor-experiments and field tests. Furthermore, a photovoltaic-based self-efficient power supply system tailored for remote sensing application of weather stations is designed. This system ensures the measurement units can endure challenging months with reduced solar radiation and sustain autonomy for extended periods without external energy input. The accomplishment of this self-sufficiency is realized through the determination of the optimal inclination of the solar panels, based on local and historical solar irradiance metadata. The precise hovering capability of the vehicle is a critical factor in determining the operational efficiency during field-tests. To address this, a semi-autonomous flight control system is employed to augment the technical staff's efforts. This integration aims to enhance control efficiency and optimize the vehicle's maneuverability, especially in the presence of wind disturbances. A GPS-based navigation system is utilized to adjust and inspect the vehicle's orientation and distance relative to the target location while incorporating an obstacle avoidance function. Moreover, an autonomous detection system for transmission towers, coupled with flight control adjustments to approach the specified installation position on one of the mast corner legs, provides valuable guidance to the pilot, particularly in homogeneous environments. The detection and flight control algorithms employed for the installation and retrieval of weather stations, aimed at repair or extension purposes, undergo comprehensive evaluation and refinement. The automation of these processes yields substantial enhancements in the distribution and maintenance of the sensor network, which spans vast distances, covering thousands of kilometers. The implementation of such automation offers a high degree of flexibility, leading to a reduction in time and human costs by a minimum of 50%, particularly in installation locations characterized by challenging access conditions.

Contents

Acronyms and symbols

Acronyms

IHE	Institute for High Frequency Technology and Electronics
KIT	Karlsruher Institute for Technology
TSO	Transmission System Operator
DWD	Deutscher Wetterdienst
OLMS	Overhead Line Monitoring System
NWP	Numerical Weather Prediction
FEM	finite element method
RC	radio-controlled
DoF	degrees of freedom (DoF)
CAD	Computer-Aided Design (CAD)
ROS	Robot Operating System
SDK	Software Development Kit
IDE	Integrated Development Environment
UCS	UAV coordinate system
FOV	Field of View

CNN	Convolutional Neural Network
DBSCAN	density-based spatial clustering of applications with noise
DOE	Design of Experiments
GUI	Graphical User Interface
ROS	Robot Operating System
PSH	peak sun hours
MOGA	multi-objective genetic algorithm
MLF	Multi-layer feed-forward neural network
SLAM	Simultaneous Localization and Mapping
SSD	Single-Shot multibox Detection
LSD	Fast Line Segment Detector
SIFT	Scale-Invariant Feature Transform
SURF	Speeded-Up Robust Features
SSD	Single Shot multibox Detector
YOLO	You Only Look Once

1 Introduction

1.1 Motivation

Global warming is currently a significant challenge, exposing human beings to evident and potential dangers. To mitigate the consequences and perils linked to climate change, the European Commission introduced the Paris Agreement, which established a long-term objective of limiting the rise in global average temperature to below 2°C (1). In line with the European Union's proposals and concerns over hazardous energy sources, nuclear power plants are slated for gradual decommissioning, with complete phase-out of the remaining stations expected by 2022 (2).

The feed-in management of energy production from renewable installations contributes to a reduction of 40% greenhouse gas emissions in the energy sector. It is anticipated that a 100% renewable electricity supply system will be achieved technically and economically by 2050 in Germany (3). The electricity supply in Germany is becoming more environmentally friendly and sustainable. Solar and wind power are the most prevalent and significant renewable sources in the country. Notably, the large amount of wind energy generated in northern Germany is transmitted over long distances to the consumption centers in southern Germany and across Europe (4).

A large portion of electricity derived from renewable green energy encounters challenges while being forwarded through the transmission grid. This is attributed to the decentralized installations, necessitating the integration of energy into the electricity grid and its subsequent supra-regional transportation. However, the existing transmission grid was designed for traditional purpose, centered around centralized energy production in proximity to consumption centers to meet the demand. Consequently, the energy transition introduces notable regional imbalances and grid congestion (bottlenecks) as the transmission lines reach their limits and demonstrate insufficient transmission capacity (5).

The Transmission System Operators (TSOs) are obligated to safeguard the grid against overload damage and potential blackouts. A key measure to address grid congestion is re-dispatch, wherein power plants are scheduled in advance using day-ahead solutions to increase or decrease electricity generation in response to demand (6). However, the frequent requirement for re-dispatch measures has resulted in a rapid increase in costs over the years, for instance, from 132.6 million euros in 2013 to over 1 billion euros in 2020 (7). Ultimately, these costs are passed on to consumers as part of the electricity fee.

The increasing costs associated with measurements and fluctuations arising from decentralized renewable energy sources underscore the urgency for expanding the transmission grid. This expansion would facilitate improved supra-regional transportation and feed-in of green energy into the grid. However, the decision-making process regarding the construction of new power lines and the selection of route corridors lies under the jurisdiction of the Federal Network Agency. Multiple suggested routes and each corridor are subjected to examination by TSOs and are publicly assessed in terms of their environmental impact and effects on local communities. Furthermore, the successful implementation of planned grid expansion heavily relies on the high acceptance and comprehensive participation of citizens (8). These multi-stage procedures for approval and citizen support contribute to a slow grid expansion process.

The German Federal Network Agency has mandated the NOVA principle, which emphasizes the optimization of existing transmission grids before undertaking grid strengthening or further expansion (9). This principle guides TSOs to pursue efficient and optimized usage of the current transmission grid. Presently, overhead lines are standardized to withstand worst-case conditions, such as "high summer weather," characterized by ambient temperatures of 35°C and wind speeds of

0.6m/s (10). Indeed, real-time monitoring of the conductor's operational temperature presents a viable opportunity for enhancing transmission capacity. This can be accomplished using either contact or non-contact methods, such as infrared temperature measurement.

However, cooler temperatures during the night and other seasons, or stronger winds, can lead to a more favorable cooling effect and thus increase the transmission capacity. For instance, monitoring the ambient weather conditions along overhead lines enables the capacity to exceed the standard level. DLR offers a grid optimization method, wherein the maximal transmission capacity is heavily reliant on the ambient weather conditions, as severe weather occurrences are infrequent for most of the year. The Overhead Line Monitoring System (OLMS) necessitates real-time monitoring of the current conductor temperature and line sag to enhance transmission capacity without risking overloading. DLR is determined by the operation temperature, which can be calculated based on the surrounding weather data along the overhead lines and initial conductor properties (11).

Nevertheless, most of the temperature or DLR based OLMS available in the market can only monitor real-time transmission capacities. To fulfill the specific requirements of TSOs, incorporating ampacity forecasting in conjunction with weather forecasting becomes imperative for grid congestion stabilization in advance. This capability empowers TSOs to arrange and make decisions on electricity trade one to two days ahead, especially for the cross-border energy market. To ensure the precision of mid-term and long-term ampacity forecasting, high-resolution local weather forecasting along the overhead lines is essential. Improved forecast accuracy leads to reduced grid congestion. Some weather phenomena, such as strong convection, can only be accurately obtained with a spatial resolution below 2 km, which requires the utilization of numerical weather models (12)(13).

The regional ICON-D2 model from Deutscher Wetterdienst (DWD) provides an improved forecast model, particularly suitable for predicting hazardous weather conditions. It offers a fine horizontal resolution of 2.2 km and provides forecasts up to +27 hours at 3-hour intervals(14). Nonetheless, providing a detailed vertical description of weather changes relevant to the height and sag of overhead lines remains a challenge for OLMS. While the influence of fine-scaled topographic effects, such as ground fog and flash floods, is observable, irregular topographies like mountains or forests located near the overhead lines can induce wind turbulence effects and consequently lead to significant weather changes. Describing these phenomena accurately in atmospheric models remains a challenge. (15).

The main challenges for energy transition are as follows:

- Decentralized renewable energy production leads to increased congestion in the electricity transmission grid due to regional imbalances and the need for supra-regional transmission.
- The multi-stage process of discussing, deciding, and selecting overhead line corridors, as well as gaining acceptance and participation from involved citizens, contributes to the slow expansion of the electricity grid.
- The existing electric grid operates on static line ratings, wherein a conservative transmission capacity limit is uniformly defined for the entire grid, accounting for worst-case weather conditions that occur only infrequently throughout the year(16).
- The management of congestion is currently predominantly achieved through re-dispatch and feed-in management, with related national costs surpassing 1.2 billion euros in 2019 and 1.4 billion euros in the previous year. These costs are ultimately passed on to consumers through electricity fees(17).
- Grid congestion poses a significant obstacle to the feed-in and efficient utilization of renewable energy, resulting in a considerable number of renewable power plants being unable to operate optimally. For instance, approximately 78 percent of the curtailed electricity generated by onshore wind power plants could not be fed into the power grid, while the corresponding figure for offshore wind in Germany in 2019 was approximately 18 percent(17).
- Most of the currently available weather-dependent monitoring systems primarily focus on providing and monitoring the real-time transmission status

of overhead lines. However, efficient electricity management requires the ability to anticipate changes one to two days ahead. Consequently, the development of a weather-dependent capacity forecasting system becomes imperative to meet these requirements.

- The existing Numerical Weather Predictions (NWP) provide weather forecasts with limited fine-scaled horizontal and time resolution, and they do not adequately model the influence of ambient topography (forests, mountains, rivers, etc.) along the overhead lines in the NWP.

Thus, energy sustainability necessitates an urgent short-term alternative to achieve a flexible, risk-free, and efficient usage of the current grid. Real-time monitoring of transmission lines is crucial to prevent overloading. Meanwhile, the development of an appropriate capacity forecasting system is imperative to optimize energy production and proactively reduce congestion. This forecasting system should be commercially and technically viable, competitively affordable, and exhibit high system performance.

1.2 PrognoNetz - Enhancing Energy Transmission Through an Intelligent Capacity Forecast System

The rapid expansion of decentralized renewable energy, along with increasing international electricity trade, is pushing the power transmission capacity of overhead lines to its limits. To effectively manage grid congestion, increase the feed-in of renewable power, and prevent temporary shutdowns of power plants, Transmission System Operators (TSOs) are pursuing the development of an intelligent capacity prediction system. Therefore, a weather-dependent grid monitoring and forecasting system, integrated with three-dimensional meteorological models, is crucial to enhance transmission capacity, taking into account the significant influence of surrounding topography near transmission lines, such as forests and mountains. As presented in Figure 1.1, the research project "PrognoNetz" aims to build capacity prognosis models using artificial intelligence. The historical weather data is collected and processed at the central station, utilizing distributed weather sensor networks positioned along overhead lines.

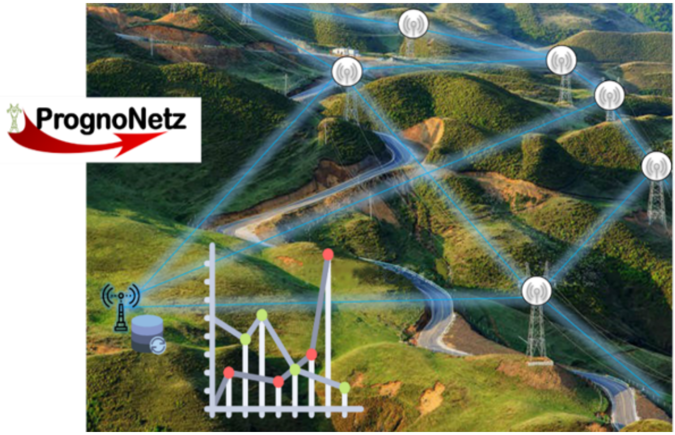

Figure 1.1: Within the framework of PrognoNetz, a self-learning real-time power load monitoring and forecasting system is under development. This system facilitates weather-dependent operation of overhead lines, enabling Transmission System Operators to achieve enhanced efficiency and reliability in decentralized green energy transmission.
Source: The Institute for Information Processing Technologies(ITIV),KIT

As part of the PrognoNetz initiative, the Karlsruhe Institute of Technology (KIT) is collaborating with five industrial partners. This collaboration is supported and funded by the German Federal Ministry of Economic Affairs and Energy[1]. The project is scheduled to run from January 2019 to March 2022. Wilmers Messtechnik GmbH is responsible for the development, installation, and maintenance of wireless communicated weather stations. UBIMET Deutschland GmbH is dedicated to the development of three-dimensional real-time and predicted meteorological models with high resolution along the transmission lines, utilizing

---

[1] Bundesministerium für Wirtschaft und Energie, BMWi

selectively distributed weather measurements. The IT company unilab AG provides the graphical user interface (GUI) for visualizing the collected weather measurements, predictions, and capacity forecasts. The associate partners, Transnet BW GmbH (TSO) and GWU Umwelttechnik GmbH (weather sensors), contribute their expertise and provide approval for the utilization of the grid infrastructure for field tests.

The main research tasks at KIT within PrognoNetz are:

- The research focuses on the development of a self-learning monitoring and forecasting system, leveraging distributed weather measurements along high-voltage lines. Simultaneously, the system aims to identify and determine the number and positions of "Hotpots," which represent transmission routes with minimal transmission capacity.
- This dissertation focuses on the installation and maintenance of weather stations on transmission towers employing unmanned aerial vehicles. Conventionally, technical personnel are required to ascend the towers to install and replace sensors, a process that proves particularly costly and time-consuming, especially in complex and demanding terrains like mountain valleys. By adopting UAVs for these tasks, notable improvements in efficiency can be achieved, leading to substantial reductions in both time and costs involved in deploying weather stations across the entirety of the electric grid.
- The development of a laser-based, turbulence-free wind sensor is proposed for measurements along the transmission lines. As the weather station is installed on the transmission tower, it generates turbulence in the airflow, which can disrupt wind speed and direction measurements. However, these errors can be minimized by conducting observations at locations far away from the tower and at positions along the line sag. This approach allows for more accurate and turbulence-free measurements of wind parameters, critical for determining conductor temperature and capacity.

1.3 Research Problem

The implementation of a secure and reliable OLMS necessitates the use of fine-scaled horizontal and vertical meteorological models, derived from local weather measurements taken along the line-spans. Specifically, the inclusion of ambient complex terrains such as forests and hilly areas is vital for the efficiency of the meteorological models. This dissertation focuses on studying an efficient and cost-effective approach for the installation and maintenance of the distributed weather sensor network.

Research Question 1 *What is the operational mechanism behind the mechanical attachment of a weather station to a transmission tower, and what specific design criteria must be met to guarantee its operational functionality and long-term durability?* (Chapter 2)

The mechanical attachment of the weather station to the transmission tower necessitates careful consideration of the UAV's aerodynamic properties to endure continuous position variations caused by the vehicle and withstand disturbances from the wind. During the design process, various attachment concepts undergo rigorous analysis to evaluate their functionality and feasibility. Additionally, field tests are conducted to validate the performance of these concepts. A self-adjustment function of the mounting equipment is developed, to accommodate the diverse corner leg profiles of transmission towers, which reduces assembly costs and enhances functionality. The carrying capacity of the UAV is a crucial consideration in the design process. To address this, a lightweight construction approach for the equipment is explored using Finite Element Method (FEM) analysis.

Research Question 2 *What are the optimal design considerations for a UAV gripper system intended for the manipulation, transport, and release of sensor equipment* (Chapter 3)

The primary challenge during installation is related to the intrinsic aerodynamic properties of the UAV, which make it difficult to achieve precise hovering with high accuracy below the centimeter level. This presents a significant obstacle for the gripper system on the UAV, particularly during the release maneuver, which must be executed within a very brief time frame. Additionally, the aerodynamic forces, weather conditions, and various flight operations, such as acceleration and forward/backward motion, cause the UAV's body to incline, resulting in inconsistent loading on the gripper system. Measuring or quantifying this inconsistency remains a challenging task. To address these challenges, various constructions of the gripper system will be explored, analyzed, and field-tested.

Research Question 3 *How can we formulate the design and dimensioning of a self-sustaining solar power supply system for weather stations to endure harsh weather conditions effectively* (Chapter 4)

Creating a self-sufficient solar power system for remote weather sensing is essential due to practical limitations. This design process considers local weather conditions, operational requirements, and energy storage for adverse situations. It aims to size solar power adequately, optimize panel angles for energy capture, and determine battery capacity for uninterrupted operation. Input parameters include the tower's GPS location and hourly solar irradiance data from Deutscher Wetterdienst (DWD).

Research Question 4 *How can computer vision-based semi-autonomous flight control enhance pilot assistance during installation operations?* (Chapter 5)

At the altitudes where weather conditions are observed, typically exceeding 30 meters above ground level, UAV pilots encounter substantial difficulties in discerning the orientation of the mounting corner leg on transmission towers and executing precise maneuvers with the UAV within this visually uniform environment. To address this challenge, a solution is found in the development of semi-autonomous flight control algorithms that rely on computer vision. These advanced algorithms provide the pilot with essential information concerning the orientation of the tower structure, the detection of the installation site, and precise depth identification. This, in turn, facilitates accurate vehicle positioning for the installation process. Importantly, the utilization of multiple depth cameras for depth perception necessitates extrinsic calibration to ensure alignment with the UAV's reference coordinate system. Furthermore, the assurance of safety in autonomous flight control is of paramount concern. In this regard, provision is made for the pilot at the ground station to deactivate the autonomous flight control process at any moment, with manual control always retaining the highest priority.

2 Mechanical Design of the Installation System on Transmission Tower by using UAV

This chapter elucidates the mechanical attachment design for securing sensor equipment onto the specified corner leg of transmission towers. The proposed solution prioritizes both security and adaptability to accommodate the diverse geometrical configurations and dimensions of electricity towers. To address this challenge, an ingenious self-adjustment mechanism has been integrated into the attachment system. Furthermore, the chapter delves into the intricacies of lightweight construction techniques for the installation equipment, thus guaranteeing a minimal payload for the UAV during deployment.

2.1 Related Work in the Installation of Weather Stations within Electrical Grids

In the PrognoNetz project, a distributed sensor network is deployed along two high voltage lines, situated at the same height as the line sag. These sensor networks operate self-sufficiently, ensuring continuous functionality even in severe weather conditions and autonomously transmit critical data wirelessly to the control center. The capacity forecast, derived from weather prognosis, empowers the TSOs to efficiently manage renewable power production and electricity trade up to two days in advance, thereby securing a reliable and sustainable energy supply. Additionally, the project enables the observation and analysis of topographic influences on weather conditions through the utilization of historical weather data. This comprehensive approach enhances the monitoring and forecasting capabilities, leading to improved grid performance and a more resilient energy transmission system.

Nowadays, weather measurements along overhead lines are primarily divided into two distinct approaches:

- For over half a century, meteorologists have utilized masts or towers for conducting continuous profile measurements with high vertical resolution. These standard infrastructures are equipped with various sensors to facilitate different experimental measurements (18). However, the construction of meteorological measurement masts involves several challenges, including the selection, decision-making, and obtaining permission for ground locations, as well as the need for comprehensive cooperation and acceptance from the relevant citizens. In contrast, the installation of weather stations in irregular terrains allows for a swift and efficient erection of weather masts.
- In addition to avoiding the need for extra land usage, existing electrical towers present suitable and sustainable alternative infrastructures for weather station installation. However, due to the potential danger involved in tower climbing and sensor mounting, technical staff require specific training to ensure safety during these operations. As illustrated in Figure 2.1, the weather station is affixed to one corner leg of the tower, situated at the height corresponding to the lowest position of the line sag above the ground, enabling the measurement of adverse weather conditions. Nevertheless, the tower structure can induce the "turbulence effect," causing fluctuations in the speed and direction of airflow and, consequently, leading to inaccuracies in wind measurements. To mitigate this issue, a mounting cantilever with a length of 2 meters is introduced, relocating the wind measurements away from the tower structure, the turbulence influence is notably diminished, resulting in an impressive measurement accuracy of 96% (19).

Figure 2.1: Field tests were conducted along two high-voltage lines as part of the PrognoNetz project to gather crucial ambient weather data required for artificial intelligence-based power load forecasting. The weather stations, indicated by the yellow rectangular boxes, were manually installed on one of the corner legs of the mast by trained technical personnel who climbed the towers following comprehensive safety training.

2.2 Mechanical Attachment Mechanism

The implementation of UAV technology provides a more efficient and streamlined approach for the installation and maintenance of the sensor network in the electricity grid, particularly in locations that are difficult for human access. As depicted in Figure 2.1, the incorporation of a sensor mounting cantilever is crucial to reduce the turbulence effect caused by the tower structure. To achieve this, a modular assembly process is executed with the UAV, encompassing the following steps:

1. A passive and permanent attachment of the sensor mounting cantilever onto the predefined corner leg of the transmission tower.

2. After successful verification of the cantilever's installation, the sensor nodes can be securely mounted and easily retrieved for maintenance in the designated holder on the cantilevers.

The utilization of UAV-based installation and maintenance procedures significantly enhances the overall efficiency of weather station deployment, offering increased accessibility to challenging locations and ensuring timely and reliable data collection for more effective grid management and enhanced decision-making processes. This approach provides valuable insights for improved weather monitoring and forecasting capabilities within the electrical grid infrastructure.

2.2.1 Mechanical Attachment of Sensor Mounting Cantilever on the Transmission Tower

This section begins by presenting the construction of the cantilever, focusing on its fixation mechanism, specifically designed for the transmission tower with an L-shape-profile corner leg. Subsequently, the adaptability of the cantilever to accommodate diverse profile shapes will be explored in the following section.

The comprehensive assembly comprises two primary elements: the cantilever and the weather station. The cantilever is purposefully designed for permanent affixation to the transmission tower, serving as the foundational platform for the sensor holder. Furthermore, the cantilever plays a crucial role in maintaining a secure distance between the tower and the UAV, thus preventing potential collisions during both installation and operation.

Due to the inherent flight characteristics of the UAV, coupled with considerations regarding variable weather conditions, achieving precise and sustained UAV hovering at a specific position proves to be feasible only for a limited duration. Consequently, the cantilever installation process must be conducted with promptness immediately following its attachment to the tower. In this endeavor, the utilization of guidance instruments becomes imperative to either initiate or steer the attachment mechanism effectively.

The installation procedure of the cantilever is illustrated in Fig.2.2.1. Initially, the UAV's gripper carries the cantilever to the designated mounting position. Once the cantilever is securely attached to the L-profile, it will be clamped and fixed onto the tower leg. At this point, the gripper will release the cantilever, completing the installation process.

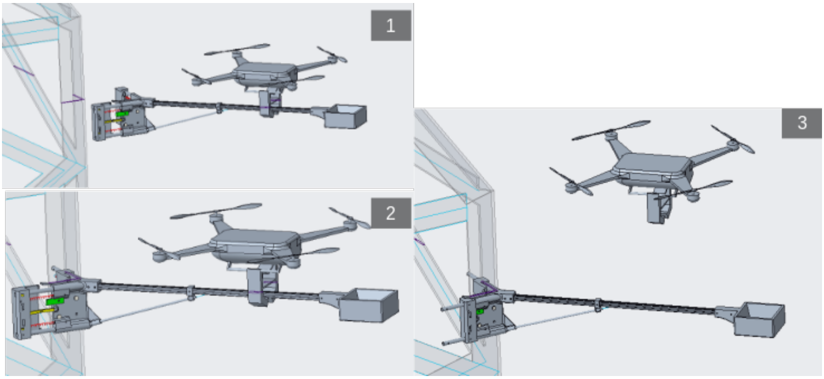

Figure 2.2: The assembly of the cantilever is performed by a drone: (1) the drone carries the cantilever to the designated location on the transmission tower. (2) the cantilever is meticulously affixed to the L-profile corner leg. (3) the clamp is subsequently engaged, ensuring the secure and steadfast fastening of the cantilever.
Source: Reprint from accepted patent by author (1) ©2022 Germany

Figure 2.2.1 illustrates the construction of the cantilever, which comprises two main components. The attachment part is responsible for the installation and fixation of the cantilever onto the corner leg of the transmission tower. Additionally, an integrated holder facilitates the installation and retrieval of the weather station for maintenance purposes. The subsequent sections will provide a detailed explanation of the attachment mechanism.

As depicted in Figure 2.2.1, the cantilever is composed of two essential components that facilitate alignment and fixation on the transmission tower. Precise control and stable hovering of the UAV at the desired mounting position can be challenging, especially under varying weather conditions. To address this challenge, the cantilever incorporates the use of magnets. When the UAV carries

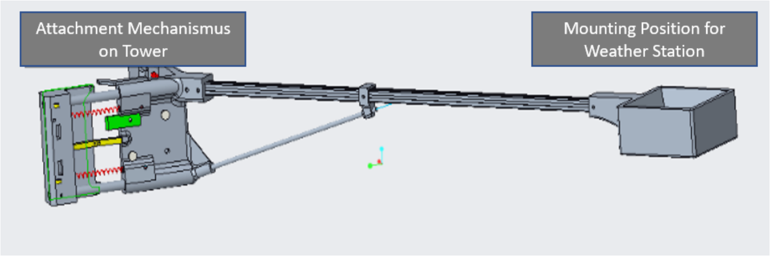

Figure 2.3: The cantilever consists of two main components: the attachment part and the sensor mounting holder.
Source: Reprint from accepted patent by author (1) ©2022 Germany

the cantilever close to the mounting profile, the magnet force comes into play, ensuring accurate alignment as the cantilever is guided to the corner leg of the transmission tower. This magnetic alignment mechanism facilitates the secure and proper positioning of the cantilever for installation. Meanwhile, movable clamps are employed to securely enclose and adjust the attachment part onto the transmission tower's profile, ensuring a reliable and robust installation. The clamps are instrumental in mitigating any torque that may be generated during the mounting of the sensor node at the opposite end of the cantilever. This comprehensive approach ensures the effective and stable deployment of the weather station on the transmission tower, providing a sturdy and enduring installation solution.

Figure 2.2.1 depicts the cantilever in both open and closed configurations. The tensioned springs, shown in red, play a crucial role in preserving the open state of the clamps. The tension force exerted by these springs is substantial enough to effectively center and enclose the cantilever onto the L-profile. It is also possible to replace these springs with alternative elastic components, by employing various methods including electrical, mechanical, pneumatic, or hydraulic components. Following the engagement of the open clamps, a snap component, highlighted in yellow, or support bolt/fastening pins can be employed. To mitigate the potential loosening of the clamps following closure, a self-lock connection is incorporated, as denoted by the green indication. Additional locking mechanisms, including the utilization of a spring pin or a servo motor-driven bolt, are also viable alternatives

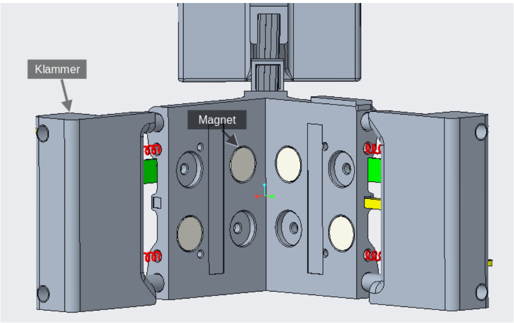

Figure 2.4: The cantilevers, which are initially unsealed, feature an additional enhancement in the form of magnets. These magnets, often pot magnets, serve a dual function. Firstly, they aid in aligning the cantilever with the power pole, ensuring precise positioning. Secondly, they serve as the initial connection points before the clamps are engaged, providing temporary attachment.
Source: Reprint from accepted patent by author (1) ©2022 Germany

that could be considered. The cantilever, as it approaches the mounting corner leg, effectively employs beveled clamps to achieve a self-centering function.

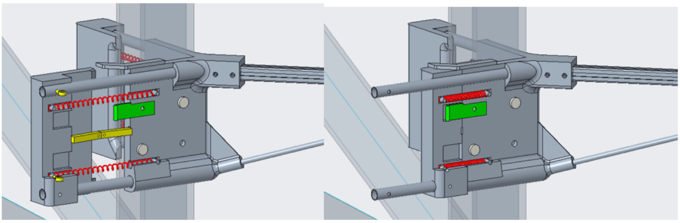

Figure 2.5: Cantilever with opened (left) and closed (right) clamp.
Source: Reprint from accepted patent by author (1) ©2022 Germany

Figure 2.2.1 provides a top view of one variation. In this depiction, the UAV has already transported and attached the cantilever to the designated mounting position. Retaining pins are inserted in the attachment section to maintain the open state of the clamps. In the course of operation, these pins can be disengaged by a drive unit on the UAV, leading to the enclosure and subsequent locking of the clamps, facilitated by the tension generated by the springs.

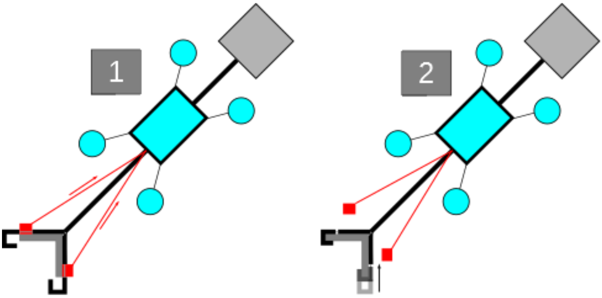

Figure 2.6: An alternative method for removing the retaining pins entails the application of a servo motor, while the drone remains attached to the cantilever. As depicted in (1), the retaining pins are inserted in the opening clamps. Subsequently, in (2), the drone disengages and removes the holding pins, thereby facilitating the closure of the clamps.
Source: Reprint from accepted patent by author (1) ©2022 Germany

Furthermore, the corner leg of the mast is furnished with periodic intersecting crossarms, as illustrated in Fig. 2.2.1. This structural component adds an extra layer of installation security, specifically aimed at preventing vertical slide-down movement of the cantilever.

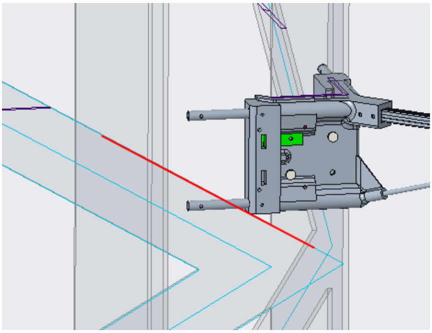

Figure 2.7: Utilizing the traverse on the transmission mast, with the edge of the traverse highlighted in red, primarily serves to prevent the downward displacement of the cantilever.
Source: Reprint from accepted patent by author (1) ©2022 Germany

2.2.2 Installation and Maintenance of the Weather Station on the Cantilever by using VAV

This section provides an exposition of the installation methodology for the weather station on the cantilever. The application requirements prior to development are essential to be defined here:

- Ensuring the primary measurement functions of the sensors, particularly the wind sensor, mandates consistent and unwavering operation devoid of vibration across a range of diverse weather conditions. This requirement involves constraining all six degrees of freedom (DoF) to uphold the precision and accuracy of sensor measurements.
- Taking into account the potential disturbances caused by airflow and UAV vibrations, achieving precise control of the UAV at specific position becomes challenging. Consequently, the installation and maintenance retrieval processes must be designed to be both feasible and resilient against significant vibrations.
- As previously mentioned, the release and retrieval processes need to be executed swiftly. Therefore, the duration for which the vehicle maintains its relative position to the sensor holder position on the cantilever during weather station deployment should be minimized.

The installation and maintenance procedure is visually depicted in Figure 2.2.2. As discussed earlier, the secure attachment of the cantilever is a fundamental requirement. Subsequently, the weather station is carefully maneuvered and guided to the specified sensor-holder position on the integrated cantilever. It's worth noting that precise centimeter-level flight control is not necessary in this phase. Once in position, the gripper arm affixed to the UAV is released or opened, allowing the weather station to be placed into the holder under the influence of gravity. Similarly, for maintenance purposes, the weather station is retrieved using the same process.

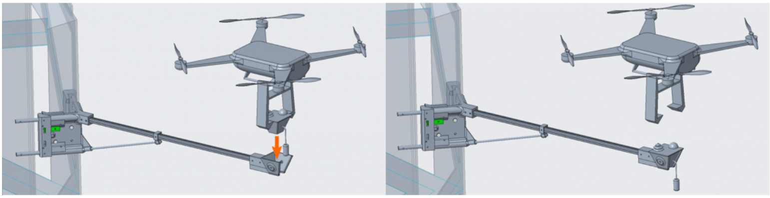

Figure 2.8: By activating the opening mechanism, the gripper arm on the UAV releases the sensor station, allowing it to be smoothly positioned within the holder under the influence of gravity. During this phase, the UAV guides the sensor station above the holder region, eliminating the need for precise hovering in centimeters and ensuring sufficient space for flight control.
Source: Reprint from accepted patent by author (1) ©2022 Germany

Figure 2.2.2 displays both an open and closed configuration of a quadrangular pyramid variant. In this design, mounting magnets are affixed to the interior wall of the payload holder, serving to enhance installation security through the introduction of additional frictional force. Alternatively, these magnets can also be positioned at the bottom of the holder. Moreover, the design must account for the inclusion of water outlets to prevent water accumulation within the holder.

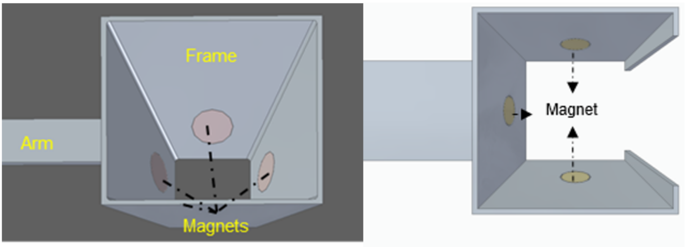

Figure 2.9: An open and a closed sensor holder configuration are illustrated for the weather station on the cantilever.
Source: Reprint from accepted patent by author (1) ©2022 Germany

Various alternative locking mechanisms, including servo motors and spring pins, offer potential avenues for implementation. In Figure 2.2.2, two distinct design configurations are showcased, each presenting different arrangements for the placement of sensors (such as temperature sensors, humidity sensors, antennas, etc.) on the housing. Notably, the depiction illustrates the weather station in both closed and open holder positions on the cantilever. Additionally, precise dimensions of the weather station are meticulously established to meet specified criteria, particularly to ensure sufficient internal volume for accommodating the data logger.

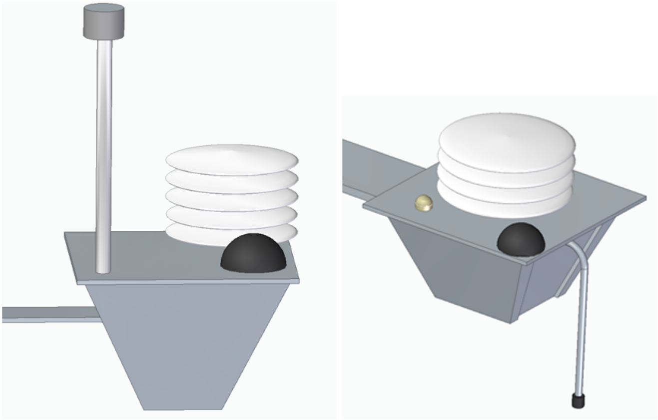

Figure 2.10: Housing for the weather station
Source: Reprint from accepted patent by author (1) ©2022 Germany

Typically, the geometry of the sensor holder varies in shape, predominantly influenced by specific application requisites. Examples of alternative holder forms are presented in Fig. 2.2.2. The critical consideration is to design the geometry in a manner that restrains both rotation and translation along the six DoF. As depicted, the prismatic shape effectively curbs rotation and horizontal translation. Additionally, vertical translation is hindered by gravity in conjunction with supplementary fixation mechanisms. Multiple payload mounting holders, situated on the cantilever, can be tailored to accommodate diverse payloads. These payloads may encompass a sensor array, solar panel, or battery.

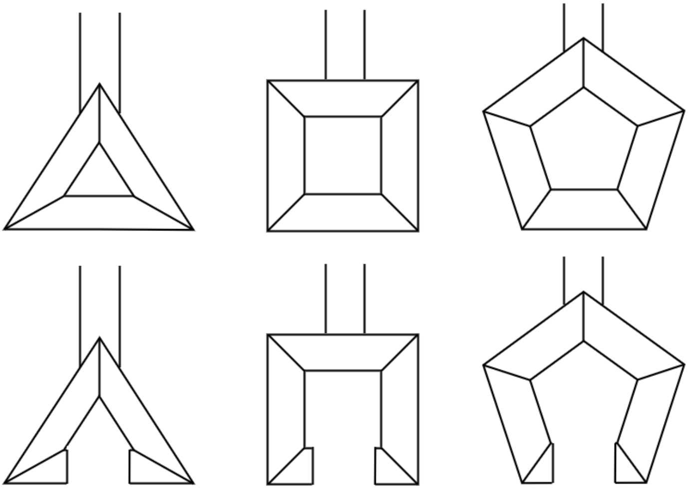

Figure 2.11: A range of distinct shapes can be employed for the payload holder to prevent rotation and translation along all six DoFs.
Source: Reprint from accepted patent by author (1) ©2022 Germany

2.2.3 Demonstrator in Labor

A prototype was constructed at the research institute to validate the feasibility of the attachment concept. Various tests were subsequently conducted to assess its functionality and performance:

- The attachment of the cantilever was subjected to testing using both magnets and a closed clamp mechanism, as depicted in Figure 2.12. A 1kg load (sandbag) was positioned in the sensor holder, and the cantilever successfully maintained its position on the simulated L-profile mast corner leg without any displacement. Notably, the fixation was found to be reliable even in the absence of magnets, demonstrating the effectiveness of the closed clamping mechanism.
- A test involving the attachment of the cantilever solely using magnets and an open clamp device was conducted. While the cantilever exhibited horizontal

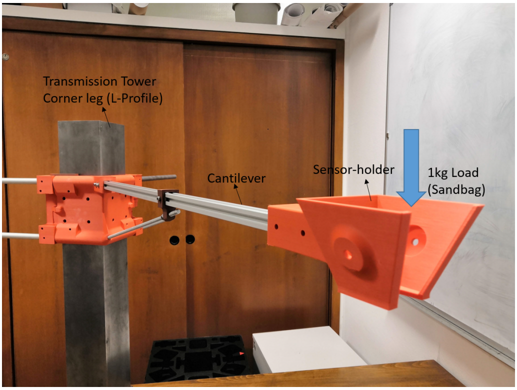

Figure 2.12: The attachment of the cantilever onto a simulated corner leg of a transmission tower demonstrated a secure fixation, effectively mitigating any risk of sliding. This assurance is attributed to the combined influence of magnetic attractive force and the clamp mechanism.

stability without any additional load, the introduction of a 1kg weight in the sensor holder resulted in a partial detachment from the mast profile. This outcome is attributed to the limited shear force exerted by the magnets, as illustrated in Figure 2.13. The results of this test underscore the necessity of a clamping mechanism.

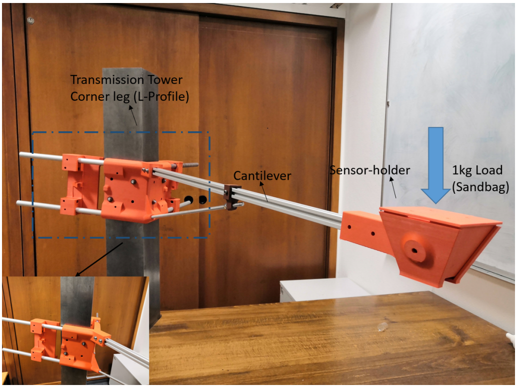

Figure 2.13: The exclusive reliance on magnetic attachment for the cantilever resulted in detachment due to insufficient shear force.

2.3 Design of a Self-Adjusting Cantilever System

In practical implementation, developing an adaptive cantilever accounts for the specific mast's geometry and dimensions. However, the varied cross-sectional profiles and dimensions of transmission tower corner legs necessitate individualized cantilever designs, which can be time-consuming and costly. To tackle this challenge, a concept of creating a self-adjusting cantilever has been proposed. This approach seeks to offer an efficient solution capable of accommodating the diverse profiles of corner legs for electricity towers. This section provides a thorough analysis of the self-adjustment prerequisites, including the examination of distinct corner leg geometries.

2.3.1 Analysis of Self-Adjustment Requirements

As above mentioned, a common question is asked here: what are the concrete requirements to fulfill during design, in order to achieve the goal of self-adjustment? In this subsection, three main types of requirements will be explained respectively, which mainly related to the length, width adjustment, as well as angle adjustment.

2.3.1.1 Profiles and Dimensions of Transmission Tower

In prior research endeavors, numerous scholars have devoted their attention to material analysis, vibration characteristics, and the overall mechanical response of electricity tower structures under wind loads or adverse weather conditions. However, scholarly literature concerning the intricate structural aspects remains relatively scarce. The current inquiry aims to address this gap by delving into the design of an adaptable cantilever capable of accommodating diverse types of electricity towers. This necessitates the exploration and compilation of a comprehensive product database encompassing various corner leg profiles.

In the context of project implementation in Germany and the critical imperative to acquire empirical data, the initiation of the "PrognoNetz" initiative encompassed a field survey along the high-voltage line 7510. The overarching objective of this survey was to comprehensively capture the ambient geographical attributes of the relevant transmission towers and their associated lines. Moreover, this endeavor aimed to facilitate the discernment and methodical documentation of the distinct mounting leg profiles employed. The insights garnered from these survey undertakings significantly contribute to a judicious evaluation of the localized installation environment. Furthermore, these findings served as a foundation for the deliberate selection of installation towers, particularly those characterized by intricate or notably intriguing geographical conditions. Such selected tower placements assume a paramount role in the accurate modeling of three-dimensional weather conditions along the designated lines.

As commonly understood, the positioning of the cantilever and weather sensors is intended to occur at the height corresponding to the lower point of line sag, while also being oriented along the trajectory of the power line. During the field survey conducted along route 7510, two predominant corner leg profiles prevalent in the German electricity infrastructure were identified. These profiles, namely the L-profile and the X-profile, hold widespread usage. The visual representation in Figure 2.14 showcases the transmission towers featuring an L-profile (depicted in the left image), a jointed X-profile (illustrated in the middle image, comprising two L-profiles), and a conventional X-profile (depicted in the right image).

Figure 2.14: Visual depiction of predominant tower leg profiles suitable for installation: L-profile (left image), jointed X-profile (middle image), and standard X-profile (right image).

Moreover, the dimensional attributes of the tower profiles are documented, as depicted in Figure 2.15. The red dashed circles prominently indicate the suitable outward-oriented mounting positions on the transmission towers. Additionally, variations in the length of a single wing and the thickness of the profiles are measured. While the determination of upper and lower limits is imperative to establish the adjustment range, it is worth noting that the scarcity of statistical data on profile dimensions precludes definitive conclusions at this stage. Consequently, the research predominantly focuses on the realization of the overarching objective, deferring a comprehensive delineation of the adjustment range until such data becomes available. In summary, the adjustment parameters encompass length, thickness, and profile angle, the latter being either 270° for the L-profile or 90° for the X-profile.

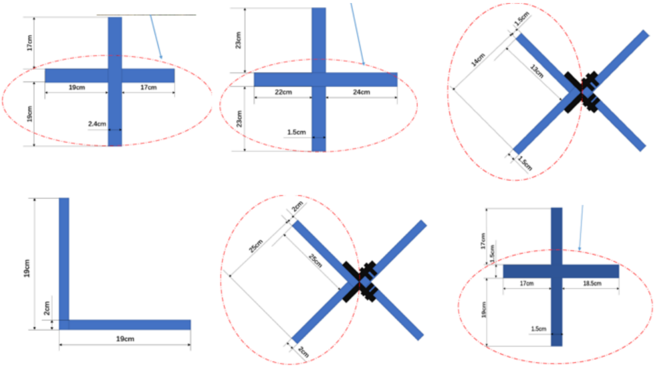

Figure 2.15: Dimensional attributes of the tower profiles, the red dashed circles prominently indicate the suitable outward-oriented mounting positions on the transmission towers.

2.3.1.2 Mast Inclination Angle at Measurement Height

The cantilever is affixed to the tower structure below the cross arm, a position strategically selected to align with the minimum height of the line sag above ground level, as depicted in Figure 2.16. Concurrently, the meticulous measurements at varying vertical heights significantly augment the holistic comprehension of the geographical impact on weather phenomena. This multifaceted data aids in the intricate modeling of three-dimensional weather patterns along the course of the line sag.

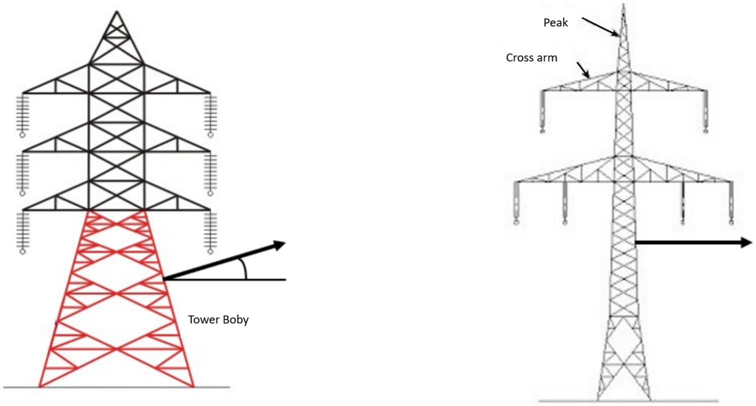

Figure 2.16: Mast Inclination angle at installation height

The pyramid-shaped tower structure depicted in Figure 2.16 necessitates the horizontal installation of the cantilever, primarily to ensure accurate wind measurements. The orientation perpendicular to the tower profile indicates the horizontal inclination angle. To evaluate the feasibility of achieving a horizontal cantilever installation, it is essential to determine a suitable range of inclination angles. Scholars have delineated the inclination angle as an optimization parameter in the context of topology construction, with its upper limit set at 8° (20). Consequently, a adjustment range for the angle spans from 0° to 10°, an interval underpinning feasibility considerations to be explored further in the ensuing section.

2.3.2 Implementation of an Adaptable Cantilever

Following the delineation of functional requisites, Figures 2.17 and 2.18 illustrate the adjustable cantilever concept for X-profile and L-profile, respectively.

Subsequent sections will provide an in-depth elucidation of the concrete realization of the corresponding adjustable functionalities. It is essential to note that the presented design blueprint represents a potential configuration and does not necessarily constitute the ultimate optimal design. As such, iterative refinement of this fundamental concept is plausible, aiming to enhance its alignment with prevailing design constraints.

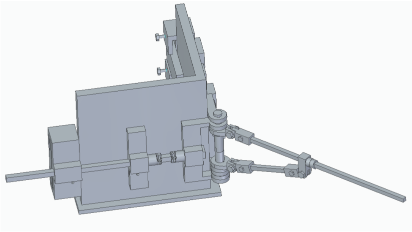

Figure 2.17: Assembly Configuration for L-profile with 270°

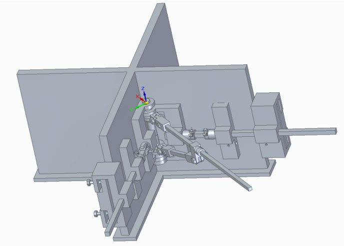

Figure 2.18: Assembly Configuration for L-profile with 90°

2.3.2.1 Adjustment of Length and Thickness

Exploiting the intrinsic symmetry of the paired wings, the Computer-Aided Design (CAD) depiction of an individual wing is portrayed in Figure 2.19. This illustration serves to elucidate the procedural intricacies of the length adjustment process. Facilitating a versatile adaptive adjustment spanning a substantial range necessitates the integration of a mobile component along a horizontal rail. Furthermore, a fastening mechanism is employed to secure the position of the connecting and adjustment segments.

The assembly procedure of the connecting element (Part 1) occurs along the axis of the cylinder, coupled with the alignment of two supplementary adjustment elements (Part 2 and Part 3) onto the supporting rail (Part 5). Characterized by its prismatic configuration, the support rail effectively curtails any rotational motion of the mobile components. The clamp part, comprising Parts 3, 4, and

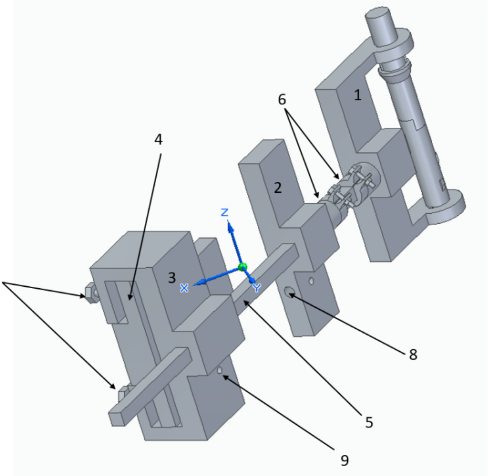

Figure 2.19: The CAD depiction detailing the length adjustment process in accordance with the profile's dimensions involves the incorporation of a sequence of mobile components along a horizontal rail.

7, integrates spring inserts within aligned apertures (No. 8) on Parts 2 and 3. These springs facilitate controlled manipulation of the clamp, enabling controlled opening and closure under tension. Following the removal of the bolt situated within aperture No. 9, responsible for securing the clamp in its designated location along the rail, the clamp undergoes horizontal displacement along the rail towards the adjustment element (Part 2) of the wing. In summation, the attainment of length and thickness adjustments is realized by means of:

- The inclusion of hinges, as illustrated by Part 6, plays a pivotal role in securely anchoring the adaptable components, specifically Part 2 and Part 3, in precise alignment along the designated motion rail, denoted as Part 5. This configuration is critical in controlling the spatial separation between Part 1 and Part 2, consequently determining the extensive range customized for length adjustment. Alternatively, to forestall horizontal movement, a bolt can be inserted within the rail structure.

- An uncomplicated method for implementing the thickness adjustment function entails the use of a screwing mechanism, as illustrated in Part 7. This mechanism is employed to precisely position and regulate the clamp component, identified as Part 4, to a suitable thickness location. Alternatively, an adaptable gasket solution can be employed to finely adjust the thickness, aligning it with the thickness dimension of the tower profile.

2.3.2.2 Profile Angle Adjustment

The pivotal component that enables profile angle adjustment is the axis, as depicted in Figure 2.20. This axis comprises two interconnected elements: the upper and lower components. After the assembly of the two wings and the cantilever arm onto it, these two axis components can be securely linked using a screw-nut mechanism or other appropriate alternatives. The axis incorporates four pairs of grooves, which serve to impose directional constraints on the wings and cantilever. Each pair of grooves is symmetrically configured, with opposing sides sharing identical geometric attributes. As depicted, the axis is outfitted with two pairs of grooves that govern the orientation of the mounting arm on the cantilever. Conversely, the lower portion of the axis accommodates two pairs of grooves that dictate the alignment of the two wings affixed to the corner leg. This imposition ensures a precisely perpendicular configuration of 90° between the two wings.

The top view of the axis is graphically portrayed in Figure 2.21, prominently highlighting the cantilever-arm orientation, denoted by the prominent black arrow, which establishes the stipulated reference direction. Conspicuously evident is the presence of two grooves, meticulously arranged at angles of $+45^\circ$ and -45°. These grooves correspond harmoniously with the intended assembly configuration of the wings, particularly tailored for the X-profile, vividly elucidated through the alignment with the accompanying black arrows. This symmetric arrangement of grooves, in conjunction with the corresponding notches within the inner wall of the wing assembly axis, facilitates a reversible assembly 270° variation for the L-profile, as illustrated by the red arrows. Moreover, an alternate approach

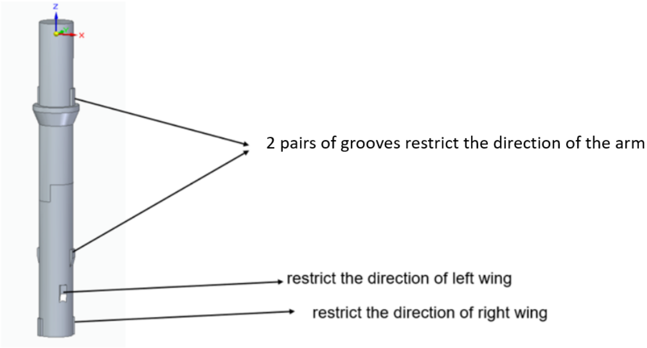

Figure 2.20: The axis functions as a crucial element in the assembly and directional adjustment of the two wings affixed to the corner leg and cantilever.

to achieving angle adjustment entails the utilization of joint grooves with predetermined fixed angles, thereby enabling precise angle manipulation between the wings.

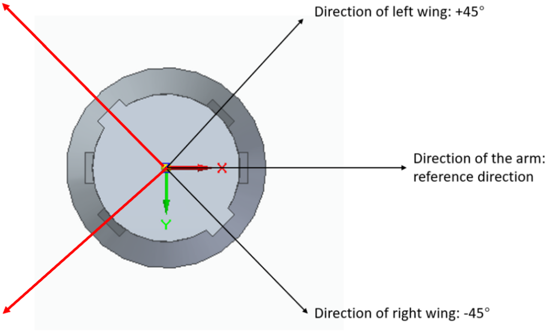

Figure 2.21: The top view of the axis. when the wings are attached to an X-profile corner leg on the transmission tower, where the angle is 90° open, the wings are indicated by the black arrow. Conversely, it also enables mounting on an L-profile corner leg with an angle of 270°, as represented by the red arrows.

2.3.2.3 Adjustment Suited to Mast Inclination Angle

With the upper limit for the mast inclination angle set at 10°, achieving horizontal alignment of the cantilever requires a strategic approach involving rotational constraints at a specified height. It's worth noting that the vertical adjustment range for the weather station side on the cantilever spans approximately up to 34.7 cm, which is calculated as 2 meters multiplied by $sin10^\circ$. This significant adjustment range highlights the cantilever's adaptability. Additionally, it's crucial to recognize that the horizontal deployment of the cantilever covers a minimum length of 2 meters. This configuration demands careful consideration due to the perpendicular gravitational forces exerted by the weather station, leading to torque and rotational tendencies, which may ultimately result in arm deformation.

In the context of outdoor application, the consistent deformation exhibited by the cantilever during operational scenarios significantly impacts measurement reliability. Consequently, the imperative to mitigate or minimize such deformation becomes paramount, thereby ensuring the requisite precision of operations and safeguarding the cantilever against potential disruptions. Illustrated in Figure 2.22, the CAD depiction underscores the conceptual framework, wherein a triangular frame is employed as a fundamental measure to augment stability and curtail structural deformation.

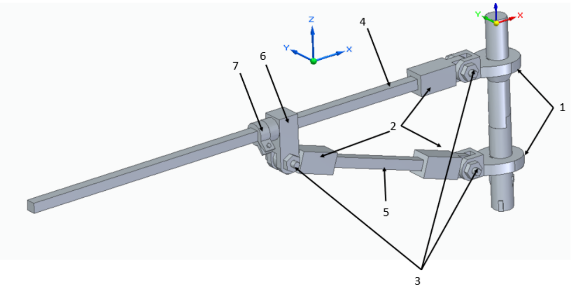

Figure 2.22: The Cantilever CAD structure assumes the pivotal responsibility of facilitating adjustments tailored to accommodate the Mast Inclination angle, thus enabling the maintenance of a horizontal weather station installation.

Three sets of kinematic joints, specifically pin joint connections, have been meticulously incorporated to exclusively permit relative rotation along a singular axis. This intricate geometric configuration is succinctly illustrated in Part 3. These joint connections inherently possess a sole degree of freedom (DoF), which enables the rotational adjustment of the cantilever component (Part 4) to achieve a horizontal orientation.

Furthermore, this innovative design seamlessly integrates the manipulation of Part 5 through rotation, facilitating the simultaneous translational displacement of Part 6 along the cantilever. Of particular note, Part 5 is endowed with the remarkable capability of adjusting its length. Consequently, the triangular framework's geometry effortlessly conforms and adapts, ultimately achieving a horizontal orientation for the arm designated as Part 4, all while compensating for the tower's inclination angle.

Once this meticulous alignment is achieved, Part 6 can be securely affixed in place through the utilization of a screwing mechanism. Alternatively, the insertion of a bolt within the strategically positioned apertures on the arm can effectively thwart any undesired horizontal translation.

2.4 Lightweight Construction of the Cantilever

In the context of the PrognoNetz project, the initial objective was to install weather stations along two high-voltage transmission lines. This strategic initiative served a dual purpose: firstly, to gather the necessary data for creating a three-dimensional model of weather conditions along the designated line sag, and secondly, to accumulate data for training a neural network responsible for predicting transmission capacity.

In light of these objectives, a significant question arose regarding the geometric configuration of the cantilever used for the manual installation process. Concurrently, the development of an automated UAV-based installation attachment was also actively explored, with this aspect evolving continuously throughout the duration of this study. It is important to note that the investigation into an automated UAV-based installation attachment was an ongoing trajectory during the course of this research.

This study introduces a systematic approach to the design and fabrication of a lightweight cantilever. The design emphasizes achieving a delicate balance between robust stiffness, enduring durability, and cost-effective material utilization. The critical objective of addressing functional requirements is met by outlining and optimizing distinct structural parameters while adhering to defined constraints.

It is essential to underscore that the current effort does not intend to reach the final state of the cantilever. Instead, this work represents an initial exploration into the realm of lightweight solutions, poised for potential expansion and refinement leading to the eventual realization of the cantilever fixation paradigm. In practical field applications, the proposed structure has been seamlessly integrated for manual installation purposes, enduring rigorous operational assessment over an elapsed period of nearly two years, thereby confirming its effectiveness.

2.4.1 Related Work

Topology optimization was employed to achieve optimal material distribution. Concurrently, shape optimization endeavors were conducted to ameliorate the stress distribution in the suspension cover of automobiles, thereby precipitating a remarkable weight reduction of 35.203% (21). The process of shape optimization harnessed the capabilities of NASTRAN, a finite element software program, encompassing a modular approach for structural analysis (22). A gradient-based shape optimization entails the utilization of the T-spline isogeometric boundary method (IGABEM). This method, characterized by its inherent attribute of dispensing with the necessity for mesh generation or subsequent post-processing procedures, embodies an iterative optimization process. Notably, the resulting structural enhancements are seamlessly incorporated within a CAD program (23).

The investigation delved into the application of a gradient-based discrete adjoint method to optimize the configuration of the inclined hole within the combustor wall, with the primary aim of attaining optimal cooling effectiveness. Subsequent functional evaluation was conducted through computational fluid dynamics (CFD) analysis, employing the Reynolds-Averaged Navier-Stokes framework (24). Optimization of beam blank design parameters was facilitated through the utilization of a multi-objective genetic algorithm (MOGA). Noteworthy in this endeavor was the imperative collaboration between finite element analysis using Ansys and MATLAB, establishing an interface to seamlessly facilitate this iterative optimization process (25).

In prior studies, a modular approach was common for lightweight construction, often requiring interfaces between software components. In contrast, our study exclusively employs Ansys, a Finite-Element-Method (FEM) based software, for cantilever geometry. This reliance allows explicit parameter definition, dynamic geometry changes, and aligns with a multi-objective genetic algorithm (MOGA) problem due to set constraints. Furthermore, the deployment of a Multi-layer Feed-forward neural network (MLF) is harnessed to discern and comprehend the intricate correlation between design parameters and structural responses. This utilization of MLF serves to expedite the subsequent pursuit of an optimal lightweight structure by enabling an accelerated search within the design space.

2.4.2 Algorithm Overview

2.4.2.1 Multi-layer Feed-forward Neural Network

The Multi-layer Feed-forward neural network (MLF), a back-propagation learning algorithm(26), is a key component of our approach. As depicted in Figure 2.23, we utilize a three-layer MLF due to its effective simplicity and good performance. In this architecture, the input layer's neuron count corresponds to geometric optimization parameters, e.g., cantilever thickness or width. Similarly, output layer neurons represent structural response parameters like solid mass or maximal deformation. Defining design ranges for each structural parameter is crucial, and the number of design parameters depends on geometry complexity. However, the volume of geometries grows exponentially with rising design parameters and resolution, imposing a significant computational burden for simulating numerous geometries and their structural parameter combinations.

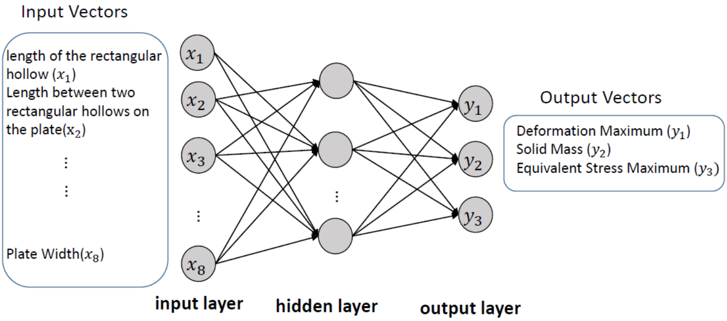

Figure 2.23: The employed neural network architecture, encompasses a three-layer feed-forward design.
Source: Reprint from previous publication by author (1) ©2020 IEEE

Indeed, the necessity to alleviate computational loads through MLF emerges due to the inherently non-linear character of the involved mathematical interrelationships. MLF is well-suited for encapsulating and unraveling these intricate dependencies. Prior to the training phase, a dataset encompassing structural responses and design parameters is generated within the Ansys software. Subsequent to data compilation, the integrated MLF model within Ansys is engaged to execute the training regimen.

2.4.2.2 Multi-Objective Genetic Algorithm

In the realm of multi-objective functions associated with the cantilever, encompassing metrics such as mass and deformation, the concurrent optimization often reveals inherent conflicts within the ambit of prescribed inequality or equality constraints (27). This quandary delineates a quintessential scenario aligned with the contours of a typical MOGA model, wherein the endeavor pertains to the concurrent maximization or minimization of multiple objectives.

Mathematically, the multi-objective functions can be articulated as follows(28):

$$minimize : y = [f_1(x), f_2(x), ...f_n(x)] \tag{2.1}$$

which subjected to the constraints:

$$g_i(x, y) \leq 0, i = 1, 2, ..., m; \tag{2.2}$$

$$h_j(x, y) = 0, j = 1, 2, ..., l; \tag{2.3}$$

where y: multi-objective function; n: the number of the objective functions; x: optimization variables.

It is important to note that simultaneous optimization of all objective functions is often rare. In practice, enhancing one function could potentially lead to the deterioration of others, as demonstrated by Rathore et al. (29). In the context of defined design constraints, the MOGA seeks to identify Pareto-optimal solutions. These solutions constitute sets of designs that optimize at least one objective function without compromising others. To facilitate this process, the hybrid elitism Non-dominated Sorted Genetic Algorithm-II (NSGA-II) (30) is employed, effectively navigating the search space to uncover global solutions.

2.4.3 Implementation

The schematic depiction of lightweight construction is presented in Figure 2.24. Prior to commencing the optimization procedure, the selection of appropriate materials assumes a paramount role to meet the specified design requisites. Following the geometric construction within Ansys, the structural parameters are likewise defined, influencing the resultant shape of the cantilever. Each parameter is assigned a designated design range, facilitating the simulation of numerous shapes. These distinctive configurations, collectively constituting a repository

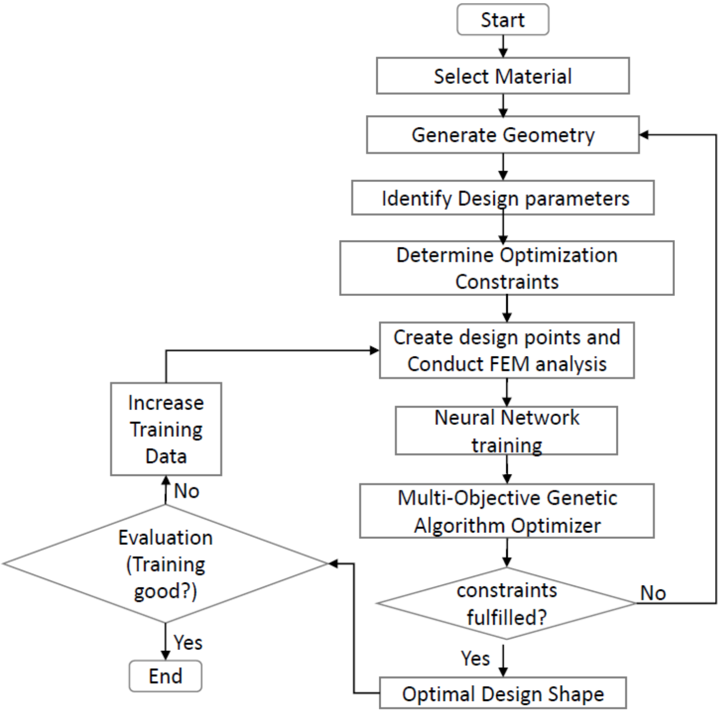

Figure 2.24: Overview of Lightweight Construction.
Source: Reprint from previous publication by author (1) ©2020 IEEE

of mechanical responses, serve as the foundation for the training of the MLF. Subsequently, this neural network is harnessed for the purpose of predicting mechanical responses associated with individual geometries. The exploration of the optimal structure through the MOGA unfolds, substantiating its efficacy through simulation-derived validation of the mechanical response. Notably, the precision of the MLF emerges as a critical facet, underscored by the requisite alignment between simulated responses of Pareto-optimal solutions and their corresponding predicted values.

2.4.3.1 Material Selection

In the context of this outdoor application, the cantilever is purposed to endure a minimum operational span of two years, facilitating the acquisition of meteorological data at elevated altitudes adjacent to high-voltage transmission lines. As a consequence, the meticulous process of material selection is compartmentalized into a sequential quartet of stages: requirement delineation, materials categorization, hierarchical assessment and ultimate material designation.

2.4.3.1.1 requirement delineation Given the outdoor application and the imperative of load-bearing capacity, a comprehensive compendium of paramount prerequisites, coupled with their corresponding material attributes, has been meticulously compiled and hierarchically sequenced. The ensuing enumeration epitomizes this classification, with a numerical annotation (1 denoting preeminent priority) assigned to each requirement, as delineated below:

Table 2.1: The prioritization of material requirements and their corresponding properties
Source: Reprint from previous publication by author (1) ©2020 IEEE

Ranking	Application Requirements	Material Properties
1	light and strong construction	Strength/Density
2	stiffness to weight ratio	Specific Young's modulus
3	outdoor working environment	Corrosion Resistance

Nevertheless, it is noteworthy that the delineated requirements are not rigid and can be adjusted based on project constraints, such as budgetary considerations. The enumerated requirements should be recognized as a comprehensive guide rather than a definitive solution for material selection. Particularly in the context of harnessing UAVs for installation and maintenance, a pivotal factor pertains to the admissible payload weight. This parameter is intricately linked to various factors, including the presence of onboard computer systems, gripper mechanisms, and the cantilever's intrinsic properties. Consequently, the weight of the cantilever necessitates meticulous regulation within predefined bounds. In tandem, this imperative aligns the material selection and shape optimization processes, forging an interdependent relationship. Should the weight of the cantilever, following the trajectory of shape optimization, fail to conform to stipulated criteria, recourse to an alternative material becomes imperative.

2.4.3.1.2 Select the material category Within the realm of engineering, materials find classification into four overarching categories: metals, polymers, ceramics, composites, and glasses. Deliberation over material attributes and production cost culminates in the preference for the metals category. Notably, metals are esteemed for their attributes of high tensile strength, mitigating susceptibility to fracture, coupled with elevated Young's modulus, serving as a deterrent against deformation(31).

2.4.3.1.3 Ranking and select the material Table 2.2 presents a comprehensive comparison of potential metallic materials. After meticulous analysis, aluminum alloy (Al-alloy) has been deemed the most fitting choice for cantilever fabrication, primarily due to its favorable cost-efficiency. Within the realm of aluminum alloys, various grades were deliberated. Notably, Alloy 2011 emerges as the preferred selection owing to its excellent formability and heightened strength characteristics, aligning seamlessly with the stipulated requirements (32).

2.4.3.2 Structural Parameters

Based on empirical observations, the triangular configuration has demonstrated exceptional stability when subjected to heavy loads, rendering it an optimal design choice. The fundamental structural parameters dictate the geometry and behavior of the cantilever. These parameters encompass crucial attributes like thickness, width, and length, which collectively determine the overall form and performance of the structure. Given the pronounced impact of mass on deformation, the pursuit of weight reduction assumes paramount significance within the context

Table 2.2: Assessment and comparison of explicit properties of various potential materials (31)

Material	ρ [$\frac{kg}{m^3}$]	**E [MPa]**	R_m **[MPa]**	**Expansion Length** [$\frac{E}{(g \cdot \rho)}[km]$]	**Breaking Length** [$\frac{R_m}{(g \cdot \rho)}[km]$]	**Price**
Steel-Alloy	7850	210000	700	2675.16	8.92	Low
Al-Alloy	2700	70000	400	2592.60	14.80	Low
Mg-Alloy	1740	45000	300	2586.07	17.24	Mid
Ti-Alloy	4500	110000	1000	2444.44	22.22	High

of rational shape design. This endeavor not only engenders streamlined material utilization and production practices but also aligns with the broader goal of cost optimization. To this end, the integration of hollow sections is embraced within the design paradigm. The schematic depiction of the cantilever's geometry is presented in Figure 2.25. Notably, the cantilever spans a length of 2 meters, with a gravitational force applied in an opposing direction along the z-axis. This configuration serves to emulate the effects attributable to the mass of the weather station.

In the realm of shape optimization, a set of multi-objective functions has been formulated:

Solid Mass, Total Deformation Maximum, Equivalent Stress Maximum

These objectives are governed by the material's "Yield Strength" constraint, represented as $\sigma \leqslant \sigma^{Yield}$.

The selection of structural parameters, which wield substantial influence over the aforementioned multi-objective functions, has been executed. Notably, an increase in the number of defined variables corresponds to escalated computational demands and augmented training data prerequisites. As a judicious compromise, a total of eight structural variables have been identified, each accompanied by corresponding lower and upper bounds:

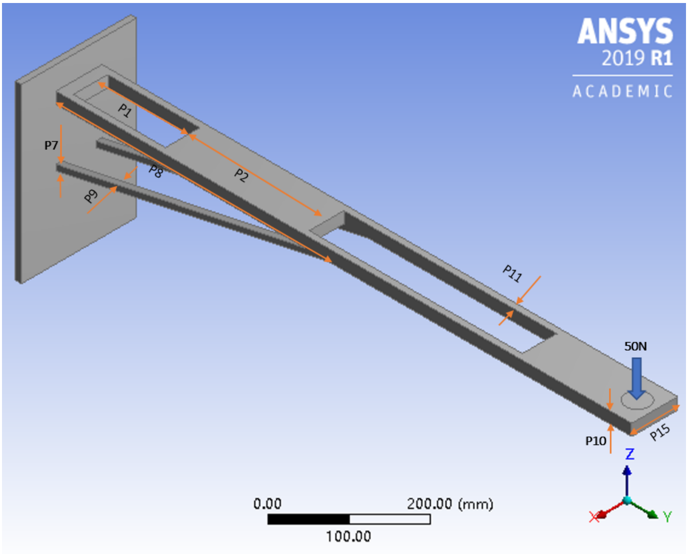

Figure 2.25: Cantilever Geometry and Design Parameters
Source: Reprint from previous publication by author (1) ©2020 IEEE

p_1: Length of the rectangular hollow: $10mm \leqslant p_1 \leqslant 1400mm$

P_2: Length between two rectangular hollows on the cantilever: $10mm \leqslant p_2 \leqslant 200mm$

P_7: Thickness of both support struts: $5mm \leqslant p_7 \leqslant 40mm$

P_8: Horizontal length of the support strut: $500mm \leqslant p_8 \leqslant 1950mm$

P_9: Width of the support strut: $5mm \leqslant p_9 \leqslant 30mm$

p_{10}: Thickness of the cantilever: $10mm \leqslant p_{10} \leqslant 40mm$

p_{11}: Half-width of the cantilever in the region with hollows: $2mm \leqslant p_{11} \leqslant 30mm$

P_{15}: Width of the cantilever: $60mm \leqslant p_{15} \leqslant 140mm$

2.4.3.3 Parametric Modeling

Given the predetermined ranges for each design parameter, the generation of initial points representing diverse geometries with distinct combinations of structural parameters necessitates the application of the Design of Experiments (DOE) function within Ansys. Employing the Central Composite Design DOE type, a total of 82 sample points are systematically generated. This comprehensive suite of sample points entails 82 simulations of mechanical responses, which can be effectively quantified through the observation of the stipulated multi-objective functions: Solid Mass, Maximum Equivalent Stress, and Maximum Deformation.

In sequence, the investigation employs three distinctive Response Surface methodologies, denoted as the "2^{nd} order polynomial", "Kriging", and "Neural Network". These techniques are integral in establishing a comprehensive and accurate mapping of the intricate correlation or mathematical interrelation existing between the defined design parameters and their corresponding mechanical responses. Subsequently, the Multi-Objective Genetic Algorithm (MOGA) is engaged to tackle the inherent non-linearity of the problem, seeking out Pareto-optimal solutions that encapsulate the optimal structural configurations. These solutions are derived based on the calculated or predicted mechanical responses obtained from the Response Surface techniques. Specifically, in the context of the "Neural Network" fitting model, the configuration features a hidden layer with 3 neurons, chosen due to its demonstrated superior performance.

2.4.3.4 Fatigue Life

In addition to shape optimization, the assessment and prediction of fatigue life constitute vital considerations for evaluating the prospective operational lifespan. Fatigue life, characterized as the number of loading cycles before the occurrence of failure due to fracture(33), holds significant import. Preceding mass production or experimental testing, the simulation-based analysis of fatigue life during the design phase is a pragmatic approach. Ansys offers the Fatigue Module, facilitating the simulation of stress cycles and subsequent analysis based on established fatigue theories such as "Goodman", "Soderberg", or "Gerber". Given the favorable performance of the Gerber theory in relation to ductile materials, it is leveraged to predict fatigue life, formulated as an expression(34):

$$\frac{\mathrm{N}\sigma_{\mathrm{a}}}{\mathrm{s_e}}+(\frac{\mathrm{N}\sigma_{\mathrm{m}}}{\mathrm{s_u}})^2=1 \tag{2.4}$$

where N: safety factor for loading cycle, s_u: ultimate tensile strength, s_e: endurance limit of the material. Meanwhile, mean stress σ_m, alternating stress σ_a are defined(34):

$$\sigma_m=\frac{(\sigma_{\max}+\sigma_{\min})}{2} \tag{2.5}$$

$$\sigma_a=\frac{(\sigma_{\max}-\sigma_{\min})}{2} \tag{2.6}$$

2.4.4 Optimization Result

The computational framework for this study employed an Intel i7-8700K CPU with a clock speed of 3.7GHz. Notably, the modeling of mechanical responses for the 82 sample points necessitated approximately 3 hours, constituting the most time-intensive phase of this investigation. Following this, the mathematical modeling and training of the response surfaces were accomplished within approximately 10 minutes. Subsequently, the pursuit of Pareto-optimal solutions through MOGA was completed in less than 10 minutes.

2.4.4.1 Effect of Inputs on MLF Performance

Within this context of non-linear mathematical modeling, the impact of individual inputs, specifically the design parameters, on the performance of the MLF is scrutinized, as visually depicted in Figure 2.26. Evidently, parameters such as P_2 (length between two rectangular hollows on the cantilever) and p_{10} (thickness of the cantilever) demonstrate pronounced influence on mass, given their determinant role in effecting the incremental or decremental alteration of the cantilever's weight, particularly concerning the heavy component of the horizontal plate. Concomitantly, P_8 (the horizontal length of the support strut) and p_{10} (plate thickness) emerge as paramount contributors to maximal deformation, attributable to their significant agency in shaping the cross-sectional configuration of the cantilever. It is worth highlighting that the effect exerted by P_1 (the length of the rectangular hollow) on deformation and stress is relatively subdued. This phenomenon aligns with a design insight that advocates a significant reduction in overall structural mass without compromising the inherent structural robustness.

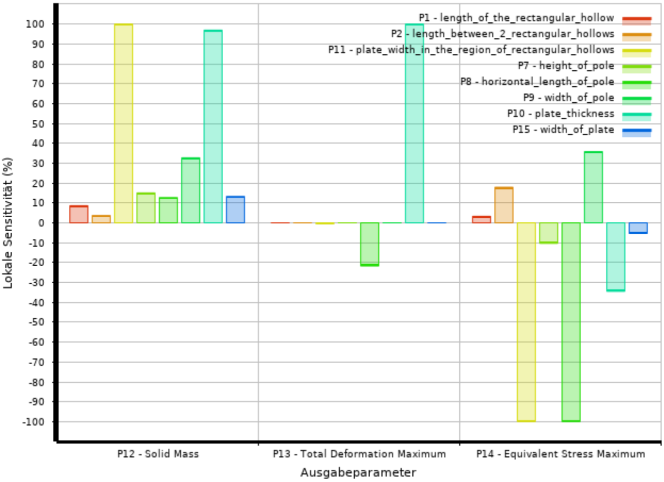

Figure 2.26: The sensitivity of response performance concerning the design parameters of the Neural Network Response Surface
Source: Reprint from previous publication by author (1) ©2020 IEEE

Figure 2.27 illustrates the variation of maximal deformation concerning cantilever thickness. Up to approximately 20mm, an increase in thickness results in a rapid reduction in deformation, attributed to the heightened cross-sectional area of the cantilever, particularly in the context of supporting heavier loads. Beyond this threshold, further increments exhibit diminishing returns in terms of enhancing stiffness, concurrently leading to amplified weight and material consumption. Figure 2.28 depicts the trend of maximal equivalent stress in relation to plate

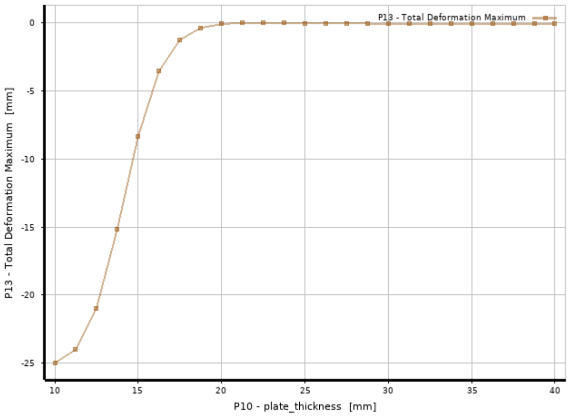

Figure 2.27: The variations in maximal deformation corresponding to changes in cantilever thickness of the Neural Network Response Surface
Source: Reprint from previous publication by author (1) ©2020 IEEE

thickness. As postulated, augmenting cantilever thickness and, correspondingly, stiffness, precipitates a decrease in maximal equivalent stress. Nevertheless, upon surpassing a certain threshold, stress exhibits an inverse correlation with augmented thickness, attributable to the resultant increase in the overall structure's mass. Thus, this analysis bears substantive significance, furnishing guidance toward the realization of a more cost-effective and robust construction approach.

2.4.4.2 Optimization Result

Following the establishment of the response surface model, the configuration parameters for the MOGA are defined, encompassing 1800 samples per iteration, ultimately generating a total of 9000 cantilever structures in the initial phase. After a cumulative evaluation of 18963 instances, a set of Pareto-optimal solutions is identified, as illustrated in Figure 2.29. This configuration indicates that, within these solutions, at least one objective function exhibits improvement without compromising others. Given the relatively higher priority attributed to

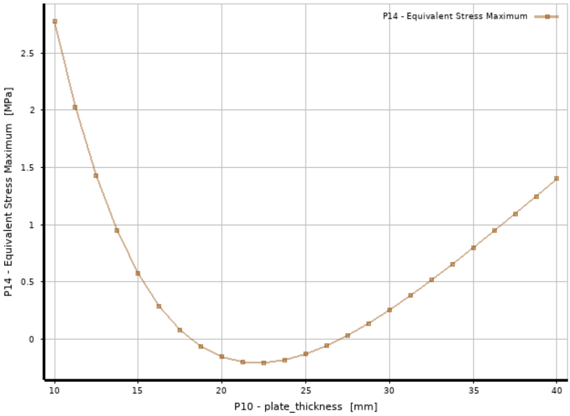

Figure 2.28: The variation of maximal equivalent stress in relation to cantilever thickness of the Neural Network Response Surface
Source: Reprint from previous publication by author (1) ©2020 IEEE

the maximal equivalent stress and deformation in comparison to mass, solutions located proximate to the P14-axis are sought after.

Evidently, a cluster of Pareto-optimal solutions is concentrated around the P14-axis. From this set, a selection is made based on the relative significance of the objective functions. Illustrated in Figure 2.30, a distinct structure resulting from the amalgamation of MOGA and MLF manifests itself, featuring its constituent design parameters alongside the predicted mechanical responses (left column), juxtaposed with their respective evaluated or simulated counterparts (right column). Notably, the Neural Network Response Surface exhibits commendable efficacy in forecasting mass and maximal equivalent stress. However, a discernible deviation exceeding 1mm in the prediction of deformation is observed. To enhance the predictive capacity of the MLF, an augmentation of the sample dataset is advocated. Nevertheless, given its favorable static structural attributes, typified by minimized deformation and well-distributed stress, this solution garners acceptance.

The Standard Response (2^{nd} order polynomial) and Kriging Response Surface methodologies are also applied using the 82 sample points, serving as a benchmark

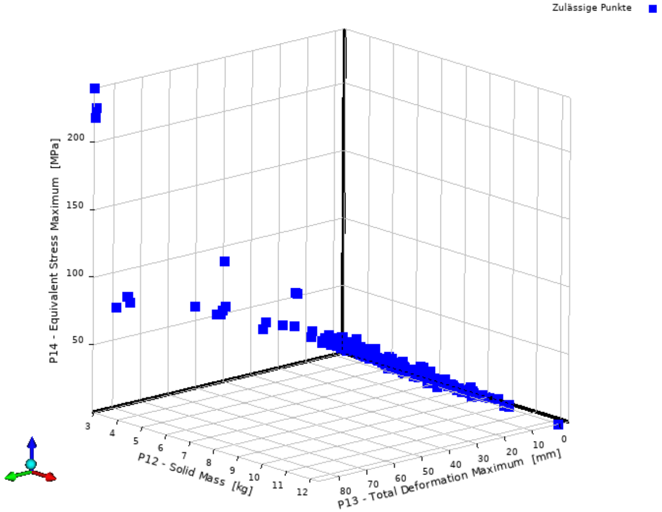

Figure 2.29: Pareto-Optimal solutions in relation to Multi-Objective Functions
Source: Reprint from previous publication by author (1) ©2020 IEEE

for conventional mathematical modeling. A solution is presented subsequent to the application of the Kriging response surface and MOGA-driven shape optimization, as depicted in Figure 2.31. However, due to its pronounced deficiency in deformation, exceeding 6mm, and substantial disparity between predicted and evaluated values, this outcome is deemed unacceptable. Similarly, the solution derived from the application of the Standard Response Surface, despite featuring a lighter mass, exhibits inferior deformation characteristics and significantly heightened stress levels. Evidently, the MLF outperforms the aforementioned non-linear modeling techniques. This underscores the paramount importance of the accuracy of mathematical modeling in attaining an optimal cantilever shape.

In the field of engineering, assessing the fatigue life of a product holds paramount significance in gauging its suitability during the design phase, preemptive to both experimental testing and mass production. In this context, the fatigue life of the chosen structure is prognosticated and scrutinized within Ansys, revealing an estimated value of 2.778e+005 hours based on the Gerber fatigue theory.

⊟ Kandidatenpunkte

	Kandidat 1	Kandidat 1 (bestätigt)
P1 - length_of_the_rectangular_hollow (mm)	16.697	
P2 - length_between_2_rectangular_hollows (mm)	25.15	
P11 - plate_width_in_the_region_of_rectangular_hollows (mm)	9.1292	
P7 - height_of_pole (mm)	10.772	
P8 - horizontal_length_of_pole (mm)	1864	
P9 - width_of_pole (mm)	5.7292	
P10 - plate_thickness (mm)	19.682	
P15 - width_of_plate (mm)	71.211	
P12 - Solid Mass (kg)	★★★ 3.5359	★★★ 3.3853
P13 - Total Deformation Maximum (mm)	★★ 0.45582	★ 1.4705
P14 - Equivalent Stress Maximum (MPa)	★★★ 9.4347	★★★ 7.383

Figure 2.30: Optimal shape configuration following MOGA optimization and its predicted structural performances using MLF (left column) and verified values (right column)
Source: Reprint from previous publication by author (1) ©2020 IEEE

⊟ Kandidatenpunkte

	Kandidat 1	Kandidat 1 (bestätigt)
P1 - length_of_the_rectangular_hollow (mm)	1021.1	
P2 - length_between_2_rectangular_hollows (mm)	187.02	
P11 - plate_width_in_the_region_of_rectangular_hollows (mm)	11.258	
P7 - thickness_of_support_strut (mm)	5.2865	
P8 - horizontal_length_of_support_strut (mm)	1884.3	
P9 - width_of_support_strut (mm)	5.7404	
P10 - plate_thickness (mm)	10.252	
P15 - width_of_plate (mm)	68.496	
P12 - Solid Mass (kg)	★★★ 1.2305	★★ 2.1505
P13 - Total Deformation Maximum (mm)	★★★ 2.1456	★★★ 6.086
P14 - Equivalent Stress Maximum (MPa)	★★★ 5.9266	★★★ 15.645

Figure 2.31: Optimal shape configuration following MOGA optimization and its calculated structural performances using Kriging (left column) and verified Values (right column)
Source: Reprint from previous publication by author (1) ©2020 IEEE

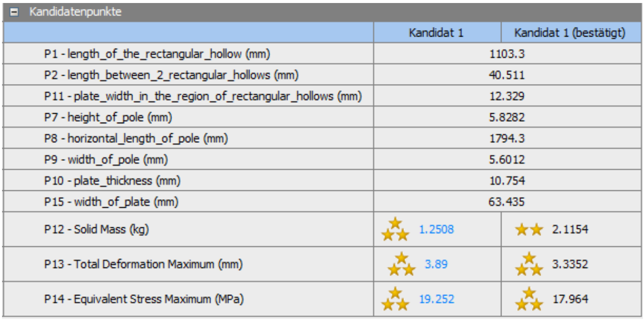

⊟ Kandidatenpunkte

	Kandidat 1	Kandidat 1 (bestätigt)
P1 - length_of_the_rectangular_hollow (mm)	1103.3	
P2 - length_between_2_rectangular_hollows (mm)	40.511	
P11 - plate_width_in_the_region_of_rectangular_hollows (mm)	12.329	
P7 - height_of_pole (mm)	5.8282	
P8 - horizontal_length_of_pole (mm)	1794.3	
P9 - width_of_pole (mm)	5.6012	
P10 - plate_thickness (mm)	10.754	
P15 - width_of_plate (mm)	63.435	
P12 - Solid Mass (kg)	★★★ 1.2508	★★ 2.1154
P13 - Total Deformation Maximum (mm)	★★★ 3.89	★★★ 3.3352
P14 - Equivalent Stress Maximum (MPa)	★★★ 19.252	★★★ 17.964

Figure 2.32: Optimal shape configuration following MOGA optimization and its calculated structural performances using Standard Response Surface (left column) and verified values (right column)
Source: Reprint from previous publication by author (1) ©2020 IEEE

3 Mechanical Design of the Gripper System for Unmanned Aerial Vehicles

Leveraging UAV technology presents an innovative and efficient approach to the installation and maintenance of weather stations within the electrical grid. To facilitate this, the design and fabrication of a UAV-based gripper system become imperative. This system serves the following purpose: firstly, to ensure the stable transportation of weather stations to transmission towers, maintaining their integrity; and secondly, to reliably install sensors on electrical towers. Additionally, the gripper system allows the UAV to retrieve the entire weather station setup for maintenance and expansion.

Within this chapter, a comprehensive exposition of distinct gripper concepts' operational tenets is presented. Moreover, the imperative of establishing a harmonious and congruent design framework between the cantilever and the weather station is emphasized, given its pivotal role in facilitating seamless installation procedures. These concepts are materialized through meticulous 3D modeling, followed by laboratory assembly using 3D printing technology. Subsequently, the viability and efficacy of these solutions are methodically scrutinized through comprehensive evaluations and rigorous field testing procedures.

Given the application context, the imperative of a reliable remote control model tailored to the gripper system emerges. This model is tasked with ensuring precise and accurate control over the processes of payload carrying, grasping, and releasing. These actions are orchestrated from a ground station to achieve the designated installation height and position. Within this context, two distinct equipment variations are under consideration, each tailored to address the unique requisites of this application:

- The concept of an independent remote control system entails that despite the gripper being physically affixed and integrated into the UAV, its operational control is conducted remotely by technical personnel stationed at the ground control center. This operational control remains distinct and separate from the overall UAV control. A practical embodiment of this approach involves the utilization of a radio-controlled model (RC model) equipped with a receiver and transmitter boasting a sufficient operational range. Commercially available products catering to this purpose offer a range of advantages, including compactness, lightweight design, affordability, energy efficiency, and dependable performance.
- The paradigm of an integrated remote control system entails the incorporation of a control interface within the existing UAV remote control setup. This design approach facilitates the remote management of the affixed gripper system by means of a dedicated control button, which can be configured or seamlessly integrated into the UAV remote control, thereby enabling the remote operation of the attached gripper system. This innovative configuration offers several inherent advantages, including seamless data transmission, congruent transmission ranges, and harmonious integration within the established control infrastructure.

  The integrated configuration is visually elucidated in Figure 3.1. For the purpose of field testing, the DJI Matrice 600 Pro UAV is selected as the platform. This UAV offers a substantial payload capacity of up to 5 kg and boasts an operational range extending to 5 km. Moreover, the platform is equipped with the Robot Operating System (ROS) interface, which seamlessly integrates with the DJI onboard Software Development Kit (SDK). In alignment with the installation and inspection objectives, the UAV is outfitted with an onboard computer, depth cameras, and a gripper system. This comprehensive setup facilitates users in accessing essential sensor data such

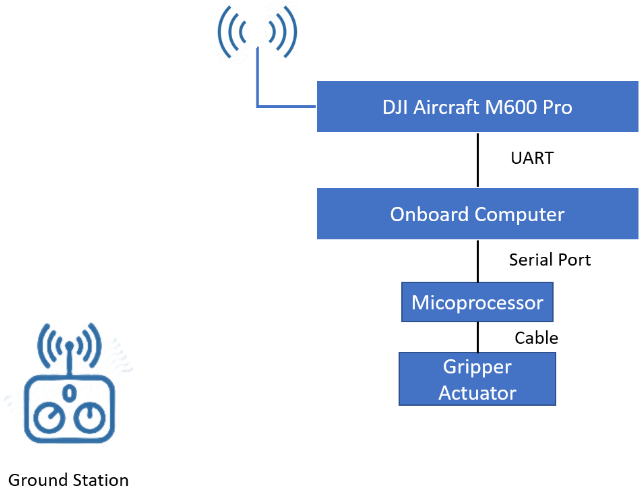

Figure 3.1: The optimal implementation of the remote gripper control system is realized through the utilization of a pre-defined button on the UAV's remote control. This approach ensures the provision of a reliable data transmission mechanism with congruent and appropriate transmission ranges.

as IMU and GPS readings, while also affording visual capabilities crucial for inspection tasks and operational oversight.

As previously elucidated, the implementation of the integrated remote control system involves the incorporation or setting of a dedicated control button within the UAV's remote control unit. Upon activation, the control command is transmitted through the designated data transmission mechanism to the aircraft. This command is subsequently disseminated as a ROS-topic on the onboard computer. This topic is then accessible for subscription and processing within the Integrated Development Environment (IDE) of a microprocessor, such as Arduino or Raspberry Pi. This microprocessor consistently interprets the remote control command for the gripper and establishes communication via the serial port with the associated microcontroller. Through this orchestrated sequence, the micro-controller executes the programmed commands to effectuate the desired and pre-defined gripper maneuvers.

3.1 Concept 1: Magnet-based Gripper

Given the UAV's aerodynamic characteristics, the gripper's actuation must occur promptly to prevent any deviation of the vehicle's accurate position and orientation amidst dynamically changing wind conditions. Electromagnetic actuators, characterized by their rapid modulation of magnetic fields or forces via swift electrical current adjustments, hold particular promise in achieving swift gripper release and retrieval. This section elucidates and designs three electromagnetic-based solutions, followed by validation through rigorous laboratory and field testing procedures.

3.1.1 Proposal A: Gripper by using Electromagnet and Iron

3.1.1.1 Working Principle

As depicted in Figure 3.2, the gripper concept's 3D model is showcased, wherein electromagnets and standard iron components are employed in this fundamental approach. The upper groove serves the purpose of securing the electromagnet onto the UAV via screwing. The number of electromagnets to be employed is contingent upon the desired attractive force, typically corresponding to the aggregate payload weight on each side. This quantity can be customized based on specific application requirements. The iron block is affixed to the cantilever. The operational principle is straightforward: upon energizing the electromagnet, the entire cantilever or weather station can be securely held, and conversely released when the power supply is disengaged. Within this operational framework, successful cantilever attachment and release were demonstrated through laboratory experimentation.

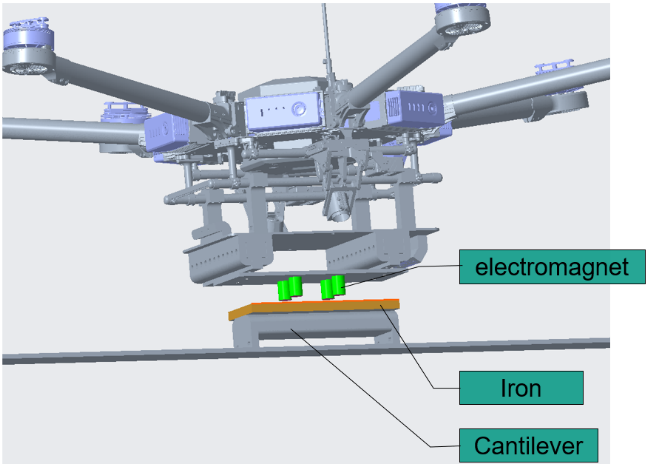

Figure 3.2: 3D model representing the gripper concept, incorporating a synergistic amalgamation of an electromagnet and standard iron components.

3.1.1.2 Encountered Problems in the Experimental Phase

While the conceptual working principle and implementation of this approach are straightforward, the feasibility of this method was refuted during the experimental phase. As depicted in Figure 3.3, a critical issue emerged. The electromagnets necessitate continuous energization throughout the grasping process. Given that the maximum operational time of the UAV for installation and maintenance procedures is limited to 20 minutes, the coils within the electromagnet experienced consistent heating due to prolonged electrical current supply. This drawback became particularly evident, as the electromagnet's magnetism weakens continuously with increasing temperatures due to heat generation. During the experimentation, it was observed that the electromagnets began to heat up within 4 minutes, jeopardizing the grasping stability and leading to the untimely detachment of the cantilever and the weather station before the installation process could be effectively completed.

Hence, an alternative solution is imperative to circumvent this inherent drawback. This entails restricting the energization of the electromagnets solely to the instant of the releasing maneuver, thereby averting the heat generation and consequent weakening of the magnetism caused by prolonged operation.

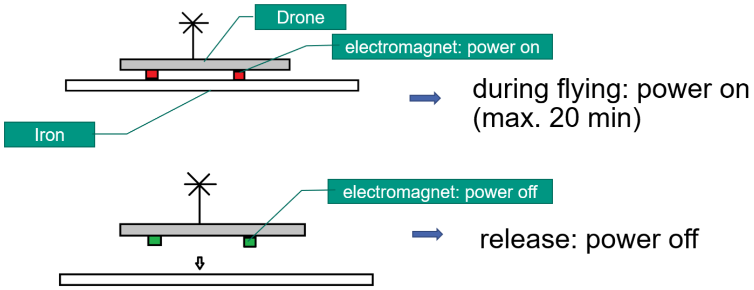

Figure 3.3: A 2D representation of the electromagnet-iron composite gripper illustrating the grasping and releasing sequences faced issues due to excessive heat generation and subsequent loss of magnetism caused by prolonged electromagnet energization.

3.1.2 Proposal B: Gripper by using Electromagnet and Permanent Magnets

3.1.2.1 Working Principle

The central challenge associated with the electromagnet lies in its propensity for heat generation during extended operational periods. To mitigate this drawback, a solution integrating both an electromagnet and a permanent magnet has been pursued. This conceptual amalgamation is depicted in Figure 3.4, wherein a comprehensive 3D rendering of the mechanism is presented. The electromagnets are securely affixed onto the gripper structure through screw-fastening mechanisms. Correspondingly, an equivalent number of permanent magnets are strategically positioned on the cantilever.

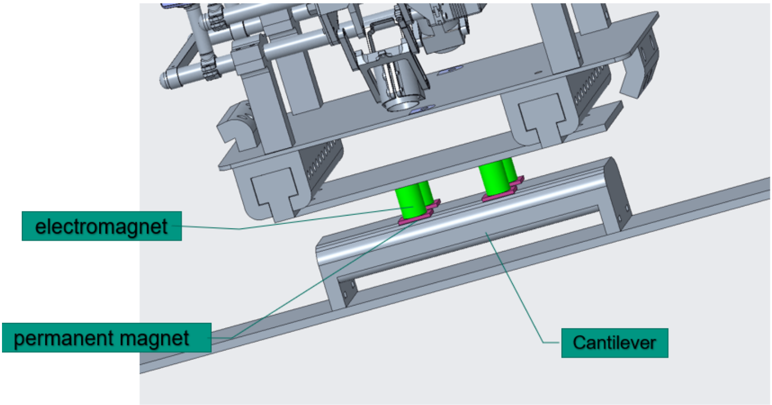

Figure 3.4: The three-dimensional model depicting the gripper concept showcases integration of electromagnets and conventional permanent magnets

The operational mechanism is visually illustrated in Figure 3.5. During the transportation phase of the equipment to the designated target, the electromagnets are intentionally deactivated, effectively functioning as standard iron components. Consequently, they can securely attach to the permanent magnets situated on the cantilever. Once the vehicle is precisely positioned, the remote control is engaged, prompting the activation of the gripper. This activation leads to the polarization of the electromagnets in a manner aligning their polarity with that of the corresponding permanent magnets on the equipment. Consequently, a repelling force is generated, facilitating the separation of the gripper from the equipment.

3.1.2.2 Encountered Problems in the Experimental Phase

After the fabrication and assembly of the installation equipment using 3D printing, a comprehensive assessment of this concept is undertaken within a laboratory setting. Preliminary trials have exposed the impracticability of this approach, primarily attributed to disparities between the inherent attributes of UAVs and

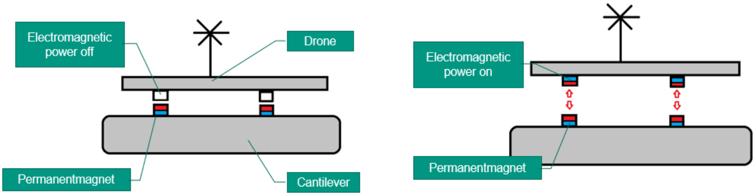

Figure 3.5: Two-dimensional visual representation depicting the sequential grasp and release processes inherent to the electromagnet-permanent magnet amalgamated gripper concept

the operational demands of the concept. Several key factors contribute to this outcome, as detailed below:

- The magnetic attractive force must exceed the combined gravitational forces of the cantilever and weather station to enable secure grasping and transportation. This requirement stems from two primary considerations: firstly, the ever-changing wind conditions could induce shaking or instability during the gripper's operational phase; secondly, inherent vibrations within the UAV resulting from aerodynamic effects contribute to this dynamic behavior. Consequently, the gripper system must be engineered to withstand and counteract these additional forces. Correspondingly, the repulsive force must also exceed the cumulative gravitational effects; otherwise, there is a risk of premature release due to UAV-induced vibrations before precise installation is achieved.

  However, determining the precise magnitude of the requisite repulsive force is a complex undertaking, primarily due to the unpredictable and variable nature of wind conditions and UAV vibrations. The absence of precise estimations for these influential factors currently renders the determination of the optimal repulsive force for successful release uncertain. The prospect of either premature or delayed releases underscores the potential for significant failures and introduces substantial safety hazards throughout the installation process.

- According to Coulomb's Law, the magnetic force can be mathematically expressed as(35):

$$\vec{F} = \frac{\mu_0 m_1 m_2}{4\pi \mathrm{r}^2}\hat{r} \tag{3.1}$$

In this equation, $\vec{F}$ represents the magnetic force, $\mu 0$ stands for the permeability of free space, $m1$ and m_2 denote the magnetic pole strengths, r represents the distance between the poles, and $\hat{r}$ signifies the unit radial vector.

As observed, the magnet force follows an inverse square relationship with distance. Figure 3.6 visually illustrates the correlation between magnet force and distance, highlighting the rapid change in force with slight variations in distance. As previously discussed, the manipulation of both attraction and repulsion forces for payload manipulation necessitates the adjustment of the distance between the electromagnet and the permanent magnet. However, achieving an extremely precise adjustment of this distance proves to be challenging and intricate, as it is essential to meet the dual criteria of generating adequate attractive force for transportation and repulsive force for a successful release.

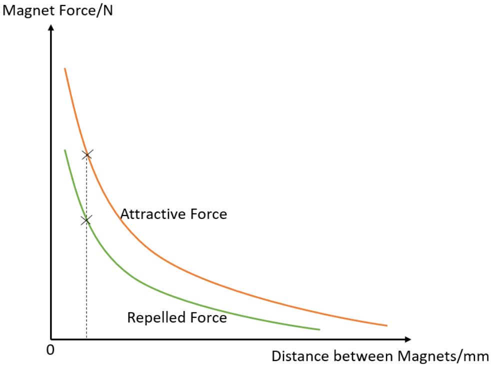

Figure 3.6: The attractive and repulsive forces undergo fluctuations in response to alterations in distance, thereby posing a challenge in achieving the highly precise distance adjustment necessary to ensure secure and safe grasping and releasing functions.

3.1.3 Proposal C: Solenoid-actuated Gripper Concept

3.1.3.1 Working Principle

Previous investigations into gripper concepts that relied on magnet force to counteract gravity and the additional loads induced by UAV wind and vibrations proved unfeasible. This section presents an alternative approach that focuses on overcoming frictional forces rather than gravitational effects. This novel perspective has led to the exploration of solenoid-based solutions. A solenoid, in this context, comprises a movable steel or iron slug housed within an electromagnetically inductive coil. The coil is intricately wound around a plunger that can be extended or retracted within the central space of the coil.

Figure 3.7 illustrates the solenoid-based gripper mechanism designed to accommodate two gripping positions, ensuring horizontal cantilever orientation during grasping and installation. This arrangement utilizes four vertically oriented arms strategically placed to prevent horizontal rotation. Four pull solenoids, indicated by the red circle, operate in a non-energized state, allowing the plungers to extend for a secure grip on the cantilever. In coordination, a corresponding ridgepole attached to the cantilever, spanning the entire distance between the two gripping locations, serves as a stabilizing element. The four fingers, connected by horizontal side blocks affixed to the ridgepole, firmly grasp it. Simultaneously, the vertical arms make contact and apply pressure to the cantilever during the gripping of the ridgepole, contributing to the balance of the cantilever.

This mechanical cohesion ensures a resilient connection, effectively curtailing any potential lateral movement along the length of the cantilever. This meticulous design effectively constrains the cantilever's 6 DoF during transportation. For release, the energized solenoids momentarily retract the plungers into the coil space, as depicted in Figure 3.8. This opening action of the gripper facilitates a seamless release of the payload.

Moreover, in the interest of expeditious adaptability to accommodate payloads of varying widths, the integration of a fully rigid gripper proves less suitable.

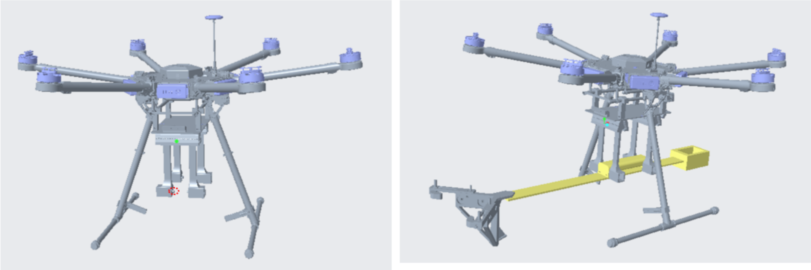

Figure 3.7: The gripper consists of 4 pull solenoids, construct two gripping positions on the cantilever for balance.

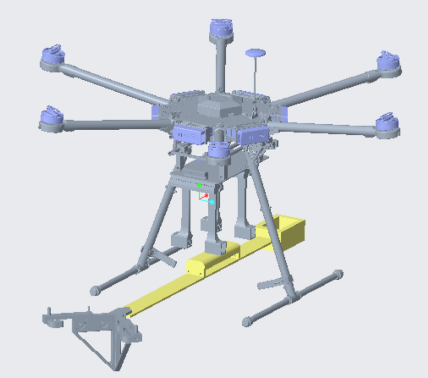

Figure 3.8: Upon energizing the solenoid system, the plungers are retracted, thereby facilitating the instantaneous release of the payload.

The notion of an electrically adjustable gripping distance is also disregarded to streamline the design and construction process. Illustrated in Figure 3.9, a modified configuration is presented, wherein the gripper's distance can be readily adjusted within grid dimensions. Achieved through strategically positioned holes along the groove rails, the gripper's positioning can be securely fixed using elongated screws and nuts.

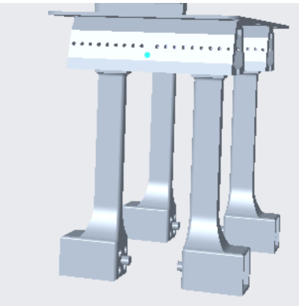

Figure 3.9: Rapid adaptation of the gripper's distance to accommodate varying payload widths is achieved through a grid-based approach.

3.1.3.2 Circuit Design

Prior to delving into the examination of the gripper concepts' feasibility, a prudent course of action dictates the initiation of field tests on a modest scale. These initial tests will be conducted on a level terrain as opposed to directly on a transmission tower, where a simulated corner leg profile of the transmission tower will be deployed. To facilitate this endeavor, the establishment of a reliable and steadfast power supply strategy assumes paramount significance. This entails the determination of the power requirements for the pertinent electronic components. In the interest of realizing a secure and seamless release mechanism, the selection of solenoid products boasting a force capacity of 30N has been made. Furthermore, the envisioned power requisites encompass the following specifications: Solenoids operating at 12V, Microcontroller Arduino Nano operating at 5V, and an RC receiver operating at 3.3V. Given the substantial current demands associated with the pull solenoids, notably at the 12V threshold, reliance on a battery-based power supply would inevitably amplify the gripper's weight burden on the UAV, consequently curtailing its operational endurance. It is therefore imperative to explore alternative and stable power supply avenues.

The UAV is equipped with two accessible power outputs dedicated to supplying power to both its onboard computer and external attachments. This power provisioning system is characterized by a voltage output of 18V and is capable of delivering a current of at least 10A. To cater to the voltage requirements of various electronic components, which conventionally demand 3.3V, 5V, and 12V, voltage conversion becomes imperative. Employing DC/DC converters for voltage conversion is favored due to their compactness, energy efficiency, and cost-effectiveness. To ensure consistent power delivery devoid of undesirable fluctuations, an electrolytic capacitor of 270µF is strategically incorporated in each conversion pathway to amplify the output power continuously and mitigate ripple effects. For a visual representation of the circuit layout, refer to Figure 3.17.

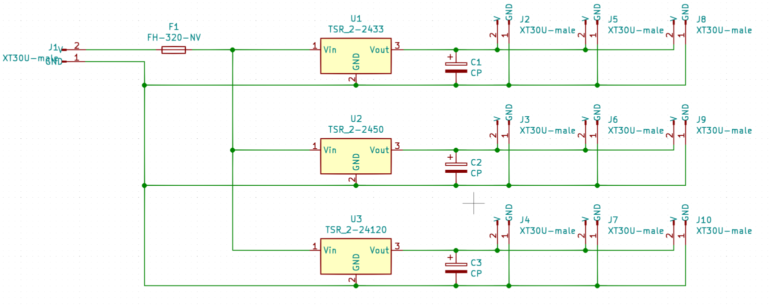

Figure 3.10: Circuit Design: Transformation of UAV Power Source (18V) into Requisite 3.3V, 5V, and 12V Outputs

Figure 3.11 presents the comprehensive control circuit diagram of the gripper, comprised of the following integral electronic components: an RC Receiver, Arduino Nano, solid-state Relay, Diode, and Solenoids. The operational dynamics are initiated by the technical personnel situated at the ground station, who wield an RC transmitter controller. The designated control buttons within the RC transmitter correspondingly activate the opening or closing actions of the gripper remotely. Propagating through a dedicated 433MHz data link, the control signals interface with the RC receiver, prompting the associated pin to transition to a HIGH state upon the engagement of a remote control button. This signal change is detected and processed by the Arduino Nano, thereby initiating the pull action of the solenoids via a galvanically isolated solid-state relay. Notably, the galvanic isolation between the control circuit and the solenoids is imperative for safeguarding both the UAV and the electronic components from potential backflow currents, stemming from the induction of magnetic fields within the central regions of the wound coils. In countermeasures, diodes are judiciously integrated into the circuit configuration to effectively counteract this undesired effect.

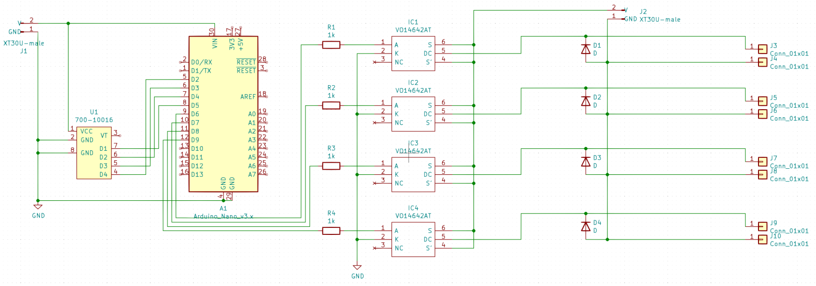

Figure 3.11: Remote control circuit for the solenoid-based gripper system

3.1.3.3 Field Test

During the field tests, an iron L-profile fabricated from two metal sheets is employed to emulate the geometric characteristics of the mounting position on a transmission tower. This structure offers both shape fidelity and transport flexibility. The UAV is equipped with an onboard computer, cameras, and the developed gripper system. As depicted in Figure 3.12, the UAV successfully transported and affixed the test cantilever onto the simulated mast profile. This accomplishment validates the feasibility of the gripper concept, demonstrating its capability to securely grasp, transport, and precisely release the payload for installation purposes. Here, the initial adhesion mechanism was exclusively magnetic in nature. The test cantilever weighs approximately 1.5 kg and comprises PLA-filament printed components along with carbon plates.

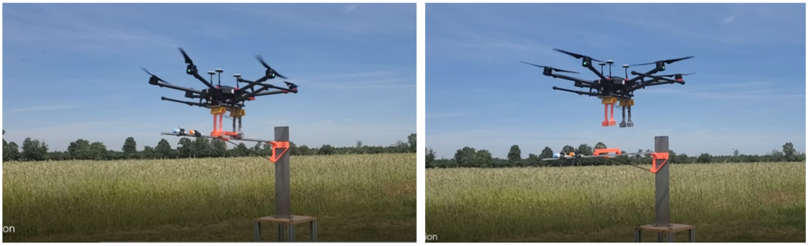

Figure 3.12: The test cantilever is effectively conveyed and securely affixed to a simulated L-profile mast with the assistance of the solenoid-based gripper system.

Moreover, the UAV effectively transported a test weather station and securely affixed it to the holder on the cantilever, as depicted in Figure 3.13. Ensuring sufficient interior space for the weather station's electronics, its upper edge exhibits a length surpassing 20cm. Consequently, should the gripper directly grasp the station's upper edge, the requisite range for adjusting the gripper width must also exceed 20cm. This extension necessitates a proportional elongation of the length of the groove rails, consequently leading to an increase in the overall weight load of the gripper mechanism.

Considering the lightweight construction of the gripper system, the incorporation of a weather station endowed with a handle emerges as a rational convenience, facilitating efficacious grasping and releasing actions for installation endeavors. Nevertheless, the exigency for meticulous UAV control precision becomes apparent, particularly in the context of docking with the sensor station's handle and subsequently retrieving it for maintenance requisites, particularly when sensor or electrical anomalies arise. Consequently, the strategic integration of an adjunct hook-shaped gripper materialized, serving to streamline UAV control procedures. As visually depicted in Figure 3.13, the vehicle adeptly navigated the sensor station into the specifically designated position above the prearranged holder, effectuating a seamless and controlled release process. Additionally, the successful removal of the station was accomplished with equal finesse through the discerning utilization of the hook-shaped gripper. The chronological enactment of the described installation and dismantling sequences transpired manually, facilitated by the adept manipulation of remote control mechanisms.

Figure 3.13: The release of the weather station is executed employing the solenoid-based gripper, while the subsequent dismantling process is facilitated through the utilization of the hook-shaped gripper.

Throughout the operational phase, several noteworthy practical insights emerge:

- Given the provided technical specifications of the DJI Matrice 600 Pro, its vertical and horizontal hovering accuracy is documented at $\pm 0.5m$ and $\pm 1.5m$ respectively in the P-GPS control mode (36). However, owing to the persistent variability of wind conditions, sustaining precise positioning or hovering of the aerial vehicle within the $\pm 1.5m$ horizontal accuracy range becomes challenging, often resulting in prolonged task completion times. To enhance installation efficiency, a concerted effort to optimize UAV stability is imperative. Consequently, the development of a computer vision-based flight control system is anticipated. This system is primed to assist pilots in orchestrating UAV control to uphold a desired relative pose concerning the mounting position during operational procedures, thereby enhancing overall flight stability.
- To avert any potential collisions between the UAV and the transmission tower, the maintenance of a secure distance is of paramount importance. Consequently, the preferred gripping position on the cantilever is positioned distal to the attachment site. Moreover, owing to the intrinsic complexity

and greater mechanical componentry within the attachment portion, this region possesses a weightier characteristic in comparison to the sensor holder side. This differential weight distribution is visually elucidated in Figure 3.14. During field testing, a perilous scenario emerged in which the foremost fingers of the gripper remained inadvertently closed during release requests. To preempt such contingencies, a critical intervention is mandated. A counterbalance mechanism is proposed, entailing the strategic placement of a mass on the cantilever. This mass is subsequently tautly affixed to the UAV via a cable, as depicted in Figure 3.14, thereby effectively counteracting the unbalanced load distribution across the gripper. Once the installation is accomplished, the mass object is promptly transported away as the UAV takes flight.

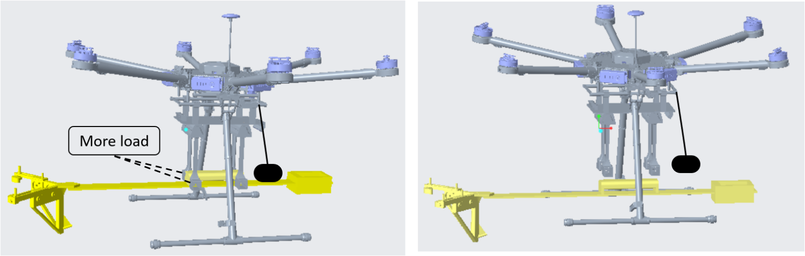

Figure 3.14: The gripping position on the cantilever is intentionally situated at a distance from the attachment point to ensure a safe separation between the UAV and the transmission tower. To achieve an even load distribution, a mass is carefully attached to the cantilever and secured with a taut cable linked to the UAV.

- The movement and orientation of UAV flight are primarily controlled through Pitch, Roll, and Yaw maneuvers. For example, the Roll maneuver causes a lateral tilt of the UAV along its longitudinal axis, resulting in lateral movement to the left or right based on rotor power and speed variations. However, this tilt poses a challenge during the grasping action, as it can prevent certain solenoids from fully retracting their plungers due to increased load. This creates a potential risk of compromised release operations, which is a critical safety concern. To address this issue, two complementary strategies are proposed: Firstly, enhancing the current pull force of individual solenoids, currently rated at 30N, through substitution with more potent magnets. Secondly, in order to address the scenario an innovative concept is proposed. This concept involves enabling an opening mechanism that operates in a rotational manner as opposed to horizontal translation.

- In the context of the stated application, the collective net weight of the solenoids alone amounts to 1.6kg, notwithstanding the inclusive gripper framework and associated electrical circuitry. The pursuit of stronger solenoids to accommodate augmented pulling force unavoidably contributes to an increased overall gripper mass. Given that commercial heavy-lift UAVs are bound by specific payload constraints, the endeavor to curtail gripper weight assumes substantial significance. Hence, it becomes imperative to devise a lightweight alternative based on the foregoing practical insights.

3.2 Concept 2: Servomotor-based Gripper with Rotate Opening Function

This section delineates the introduction of a novel servomotor-based gripper concept, tailored to address the limitations inherent in the solenoid-based counterpart. The proposed concept presents a judicious compromise, affording a harmonious amalgamation of reliability and a lightweight structural configuration.

3.2.1 Working Principle

The construction of the gripper solution is elegantly delineated in Figure 3.15, ultimately crystallizing into a motor-based conceptualization. Comprising a quartet of L-shaped grasping fingers, each under the purview of an individual servomotor, this paradigm emerges as a testament to its augmented stability and enhanced feasibility relative to alternative configurations.

Specifically, the apparatus elevates a given payload by triumphing over gravitational forces, realized through the synchronized rotational articulation of its four fingers during the release sequence. This orchestrated maneuver guarantees a smooth payload release, eliminating the risk of entanglement with the fingers, as opposed to the Solenoids-gripper concept. Consequently, it results in a rapid and controlled release process. Notably, during the phase of payload conveyance, the four fingers securely entwine with the ridgepole on the cantilever, thus circumscribing the system's DOF.

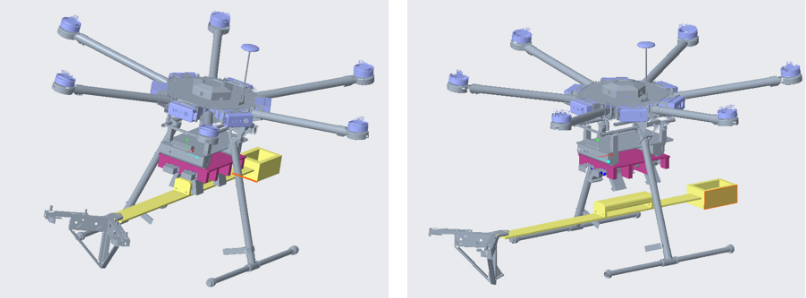

Figure 3.15: the CAD illustration of the servomotor-based gripper: grasp action (left), release action (right).

As delineated in Figure 3.16, the torque exerted by the servomotor is elucidated as the cross product of the distance vector r and the force vector f (37). The force f is expressed as a function of the coefficient of friction μ and the perpendicular force F applied to the friction surface. Adhering to the governing formula:

$$\tau = r \times f = rf\sin(\theta) = r \times (\mu F) \tag{3.2}$$

The selection of the appropriate servomotor is contingent upon various factors, including the construction specifics such as the length of r, the normal force

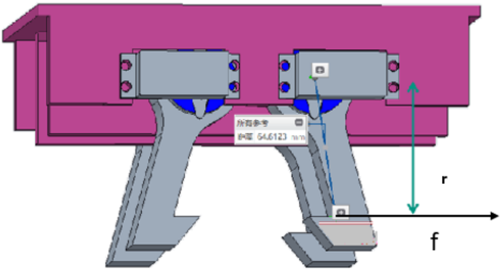

Figure 3.16: Torque exerted by the servomotor is dictated by the distance vector r and force vector f.

F, and the coefficient of friction μ. Additionally, employing a friction contact lubricated with oil or grease can effectively diminish the value of μ, resulting in a concomitant reduction in the required torque exerted by the servomotors as well as their overall weights. To specify the required torque accurately, a conservative opening force of approximately 70N has been chosen, along with a corresponding length r of 10cm.

Considering the acknowledged friction coefficients, assuming both the cantilever and gripper are constructed from steel, the coefficient of friction (μ) is determined to be 0.23 when using light mineral oil as indicated by (38). This requirement mandates the use of servomotors with a torque capacity of 161N*cm, calculated as 0.23 * 70N * 10cm. In both laboratory and external trials, under oil-oil contact conditions, the gripper consistently accomplishes smooth payload release, with a probe-cantilever weighing 1.5kg. Notably, in comparison to the solenoid-based paradigm, this design renders the gripper system significantly more practical, reliable, and lightweight, with each individual servomotor with torque 210N*cm weighing a mere 70 grams.

3.2.2 Circuit Design

As previously deliberated, the integration of the UAV's power output stands as a viable avenue for accommodating the energy requirements of the electronic constituents. This ensemble comprises a Microprocessor (Arduino Uno), four Servomotors, an RC module, and a Servomotor driver, as illustrated in Figure 3.17. Upon the engagement of a remote control button within the RC module, the corresponding pin, namely pin 5 or 6 on the Arduino, is set to a HIGH state, consistently registering the signal from the RC receiver. This ensuing control signal is then routed to the servomotor driver, thereby instigating the synchronized rotational movement of all servo motors. This synchronization of operation necessitates meticulous management of parameters encompassing operation duration and rotational orientation. The incorporation of the servomotor driver is of paramount importance, attributed to the identified desynchronization observed in the opening and closing maneuvers of the gripper's fingers during laboratory-based trials.

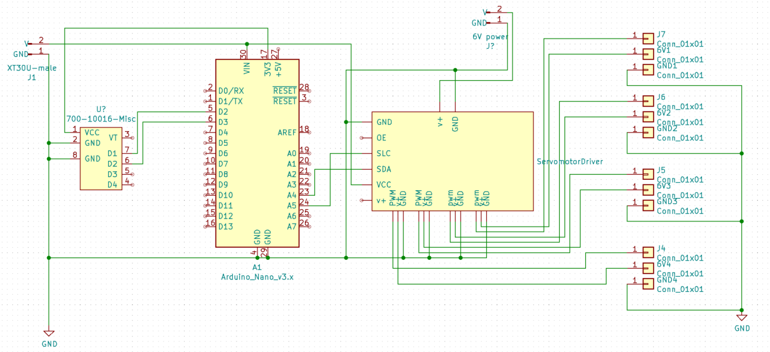

Figure 3.17: Remote Control Circuit for Servomotor-Based Gripper

4 Self-sufficient Energy Supply System for Remote Weather Stations

Within the PrognoNetz framework, despite the weather stations' intended placement on transmission towers, establishing direct connections to high-voltage infrastructure for weather measurement power supply proves both inefficient and inconvenient. Consequently, the imperative role of a remote and self-sustaining sensing system emerges within the context of this weather-dependent monitoring system. A highly viable solution involves harnessing the renewable and self-sustaining attributes of solar energy, rendering it an ideal candidate for powering such outdoor applications.

Antecedent to its application, the solar energy supply system dimensions for weather stations necessitate a resilient operation that endures even in the most adverse conditions. This encompasses establishing the autonomy days, signifying the minimum operational span without any energy storage replenishment. To achieve this, the incorporation of fundamental components such as photovoltaic (PV) panels, regulators, and batteries is paramount. Additionally, the prevailing local weather dynamics, including solar irradiance contingent on geographical coordinates, as well as seasonal and diurnal variations, underscore the significance of precisely sizing the power system.

This study introduces a systematic design methodology wherein the sizing of solar panels and batteries is automated based on the GPS coordinates of the installation mast. This automation facilitates effective solar energy harvesting, particularly during months characterized by reduced irradiance, as well as self-sustenance throughout the designated autonomy period without external energy replenishment. Central to this approach is the judicious selection of the optimal inclination of the solar panels, encompassing both azimuth and tilt angles. A case study conducted at Schnarrenberg in Germany exemplifies the application of this methodology, wherein orientation and dimension parameters for the solar energy supply system are determined using open metadata sourced from the Deutscher Wetterdienst (DWD) for the period spanning 2013 to 2017.

4.1 Theoretical Framework

4.1.1 Dimensional parameters of a self-sufficient solar energy supply system

Undoubtedly, the self-sufficiency attribute assumes a pivotal role within the wireless monitoring system, obviating the necessity for operational maintenance, which in turn forestall potential monitoring malfunctions and the subsequent incurring of supplementary repair costs. Consequently, the selection of component specifications is paramount, necessitating alignment with stipulated criteria such as product lifecycle expectations. Batteries, in particular, confer the system with an "autarkic" capability, signifying their pivotal role in storing energy to sustain sensor functionality over the defined autonomy duration T_{aut} devoid of external energy inflow. Ergo, the determination of the battery's storage capacity emerges as a fundamental parameter, calculable by the ensuing equation(39):

$$C = \frac{E_{\mathrm{tot}}}{V_{\mathrm{dc}}} \times \frac{T_{\mathrm{aut}}}{DOD_{\mathrm{max}}} \tag{4.1}$$

where
C: battery storage capacity in ampere hours
E_{tot}: average daily energy consumption in watt-hours
T_{aut}: number of autonomy days, representing the maximum system runtime with

energy consumption but without energy replenishment
V_{dc}: nominal voltage in volts
$DOD_{\max}$: maximum allowable depth of discharge for the battery, expressed as a percentage

In the context of the battery charging process in conjunction with the power supply of the weather station, an augmented solar panel dimension is necessitated. This augmentation takes into account a designated "oversupply coefficient" denoted as f_{o}, which serves to replenish the battery under adverse solar conditions and prevent its capacity from descending below the maximum discharge depth. The selection of an appropriate value for f_o hinges upon the prevailing local solar irradiance conditions, falling within the range of 1.3 to 2.0(39). For scenarios characterized by particularly critical solar irradiance, the selection of a higher coefficient is recommended. Additionally, the energy conversion efficiencies exhibited by the solar panel, battery, and regulator wield an influence over energy generation. Consequently, the determination of the solar panel's dimensions adheres to the guidelines outlined in (39):

$$P_{\mathrm{out}} = \frac{E_{\mathrm{tot}} \times f_{\mathrm{o}}}{H_{\mathrm{tilt}} \times \eta_{\mathrm{pvss}}} \tag{4.2}$$

where
P_{out}: generated power of the solar arrays, in watts
f_{o}: oversupply coefficient, dimensionless
H_{tilt}: average daily solar energy on a unit surface (m_2), in peak sun hours (PSH)
η_{pvss}: efficiency of the entire solar energy supply system, dimensionless, represented as $\eta_{\mathrm{pv-batt}} \times \eta_{\mathrm{reg}} \times \eta_{\mathrm{batt}}$
where $\eta_{\mathrm{pv-batt}}$: energy transmission efficiency from the solar panel module to the battery (accounting for cable loss)
η_{reg}: energy efficiency of the regulator
η_{batt}: energy efficiency of the battery module

In the context of each distinct application, a prerequisite pertains to the preliminary determination of system specifications. Subsequently, component selection ensues, aligning with the system's requisites, exemplified by the design parameter η_{pvss}. Notably, the parameter H_{tilt} is contingent upon the angular disposition, encompassing azimuth and tilt angles. The quantification of Peak Sun Hours (PSH) rests upon local solar irradiance and the specific installation angle. Consequently, the exploration of an optimal installation angle for solar panel deployment, coupled with the associated PSH, becomes imperative. This endeavor aims to culminate in an orientation that augments energy generation, notably during less irradiant periods such as inclement months.

4.1.2 Introduction of fundamental terms

4.1.2.1 Declination Angle (δ)

The Declination Angle (δ) constitutes a cyclical phenomenon attributed to Earth's axial tilt and its orbital motion around the sun. This angle, influenced by Earth's inclination of $23.45°$, ranges between $23.45°$ and $-23.45°$. Notably, during the summer solstice occurring on June 21 or 22, the declination angle (δ) attains its zenith at $23.45°$, subsequently dwindling until it reaches $0°$ on September 21 or 22. The latter signifies the spring equinox in the northern hemisphere and the autumn equinox in the southern hemisphere. This trend of reduction persists until the declination angle reaches its nadir of $-23.45°$ on December 21 or 22, marking the winter solstice. The consequence of this variation is a shorter daytime and prolonged nighttime in the northern hemisphere, while the southern hemisphere experiences an inverse scenario(40).

Mathematically, the declination angle (δ) can be expressed using Spencer's equation as outlined in (41):

$$\begin{split}\delta = (0.006918 - 0.399912\cos\Gamma + 0.070257\sin\Gamma - \\ 0.006758\cos 2\Gamma + 0.000907\sin 2\Gamma - \\ 0.002697\cos 3\Gamma + 0.00148\sin 3\Gamma)(\frac{180}{\pi})\end{split} \tag{4.3}$$

where Γ represents the day angle in radians, which can be defined using the following equation as stated in (40):

$$\Gamma = 2\pi(\frac{n-1}{365}) \tag{4.4}$$

here n corresponds to the sequential day number in the year, for instance, January 1st being denoted as 1, and February 1st as 32.

4.1.2.2 Hour Angle (ω)

The hour angle ω characterizes the angular discrepancy between the projected position of the sun on the celestial sphere and the solar noon. It reaches its zenith of 15° during the early morning, progressively diminishes as the day unfolds, resulting in 0° at solar noon, and ultimately reaches a nadir of -15° in the late afternoon. Mathematically, this can be expressed as(42):

$$\omega = 15(12 - ST) \tag{4.5}$$

where ST represents the local solar time:e:

$$ST = LT + \frac{ET}{60} + \frac{1}{15}[L_s - L_L] \tag{4.6}$$

where
LT: local standard time
L_{s}: standard meridian for the local zone
L_{L}: longitude in degrees
ET: equation of time defined by Tasdemiroglu(43):

$$ET = 9.87\sin 2B - 7.53\cos B - 1.5\cos B \tag{4.7}$$

$$B = \frac{360(n-81)}{365} \tag{4.8}$$

4.1.3 Solar irradiance on an inclined surface

Solar irradiance (G_β) on an inclined surface encompasses three key components: (i) direct solar irradiation (B_β), (ii) diffuse irradiation (D_β), and (iii) reflected irradiation from the ground to the tilted surface (R_β). These elements collectively contribute to the overall solar energy incident on the inclined plane, and their summation is mathematically expressed as follows (44):

$$G_\beta = B_\beta + D_\beta + R_\beta \tag{4.9}$$

where the diffuse component (D_β) is composed of three distinct constituents: (i) the isotropic diffusion component ($D_{\beta,\mathrm{iso}}$), (ii) the circumsolar diffuse component ($D_{\beta,\mathrm{cs}}$), and (iii) the horizon brightening component ($D_{\beta,\mathrm{hb}}$). With these elements considered, the expression for the solar irradiance (G_β) can be reformulated as follows (44):

$$G_\beta = B_\beta + (D_{\beta,\mathrm{iso}} + D_{\beta,\mathrm{cs}} + D_{\beta,\mathrm{hb}}) + R_\beta \tag{4.10}$$

4.1.3.1 Direct component B_β

In the northern hemisphere, the angle of incidence (θ) for solar radiation on an inclined solar panel is determined by two parameters: the azimuth angle (α) with respect to the south direction and the tilt angle (β) relative to the horizontal plane (42)(45):

$$\begin{aligned}\cos\theta = (\sin\phi\cos\beta - \cos\phi\sin\beta\cos\alpha)\sin\delta + (\cos\phi\cos\beta \\ + \sin\phi\sin\beta\cos\alpha)\cos\delta\cos\omega + \cos\delta\sin\beta\sin\alpha\sin\omega\end{aligned} \tag{4.11}$$

where ϕ signifies the latitude, and the azimuth angle (α) follows a clockwise direction.

Moreover, the solar zenith angle θ_z can be mathematically represented as described in (44):

$$\cos\theta_\mathrm{z} = \sin\phi \sin\delta + \cos\phi \cos\delta\cos\omega \tag{4.12}$$

By combining equations (4.11) and (4.12), the expression for direct solar irradiation on the inclined surface B_β can be succinctly presented, as detailed in (**?**):

$$B_\beta = B_{\mathrm{N}\cos\theta} = \frac{B}{\cos\theta_\mathrm{z}}\cos\theta = Br_\mathrm{b} \tag{4.13}$$

here B_N represents the direct beam and B signifies the direct horizontal solar irradiance, with $r_\mathrm{b} = \max(0, \cos\theta/\cos\theta_\mathrm{z})$.

4.1.3.2 Diffuse component D_β

The prevailing methodologies for estimating diffuse solar irradiance rely on the utilization of a diffusion transposition coefficient R_d. In this section, we will introduce three prominent models that embody this approach.

- Liu-Jordan model (LJ):
  The LJ-model postulates a uniform distribution of diffuse irradiance, wherein the circumsolar component $D_{\beta,\mathrm{cs}}$ and horizon brightening portion $D_{\beta,\mathrm{hb}}$ are disregarded. Consequently, this model assumes an isotropic character and can be mathematically formulated as follows(**?**):

  $$R_\mathrm{d} = \frac{1+\cos\beta}{2} \tag{4.14}$$

- Willmot model(Wi):
  The traditional isotropic model, based on the Wi model, incorporates the circumsolar component $D_{\beta,\mathrm{cs}}$ into its considerations. In this formulation,

an anisotropic reduction coefficient C_β is applied to account for the characteristics of the inclined surface. This model stands as a representative anisotropic approach and can be mathematically articulated as follows (46):

$$R_{\mathrm{d}} = \frac{B_{\mathrm{Nr_b}}}{S_0} + C_\beta(1 - \frac{B_{\mathrm{N}}}{S_0}) \tag{4.15}$$

where $C_\beta = 1.0115 - 0.20293\beta - 0.080823\beta^2$, with β expressed in radians, and S_0 represents the solar constant ($1367Wm^{-2}$).

- Klucher model(KL):
  The KL-model encompasses considerations for both the circumsolar component $D_{\beta,\mathrm{cs}}$ and the horizon brightening component $D_{\beta,\mathrm{hb}}$, thereby establishing itself as a comprehensive anisotropic model. To address the limitations inherent in isotropic models, which often underestimate the diffuse radiation component under clear sky conditions, an additional factor f_{K} is introduced to quantify the extent of cloud cover. This enhancement rectifies the model's performance, particularly in scenarios characterized by overcast skies (47):

$$R_{\mathrm{d}} = (\frac{1+\cos\beta}{2})(1 + f_{\mathrm{K}}\mathrm{cos}^2\theta\cos^3\theta_z)(1 + f_{\mathrm{K}}sin^3(\frac{\beta}{2})) \tag{4.16}$$

  where the factor f_{k} is defined as $1 - \left(\frac{D}{G}\right)^2$, where D represents the diffuse irradiance, and G signifies the total incoming irradiance onto the horizontal plane.

4.1.3.3 Ground-reflected irradiation R_β

To account for the irradiance reflected from the ground, a transposition factor denoted as R_{r} is incorporated:

$$R_\beta = \rho G R_{\mathrm{r}} \tag{4.17}$$

here the symbol ρ represents the ground albedo, which can be influenced, for instance, by variations in ground conditions (48) and can also alter over the course of the day. For the sake of simplification, a consistent value of 0.2 is often employed in calculations (49). The transposition factor R_r is mathematically expressed as per (40):

$$R_\mathrm{r} = \frac{1 - \cos\beta}{2} \tag{4.18}$$

4.2 Metadata and Algorithm Overview

4.2.1 Metadata

The DWD has strategically deployed 42 weather measurement stations throughout Germany. In the context of our algorithms, it is imperative to select the metadata from the nearest station, as it serves as the basis for evaluating PSH and determining the optimal inclination. These stations diligently capture hourly data pertaining to global and diffuse solar irradiance, which is meticulously archived in both *.txt and *.html formats. Within these files, parameters such as "FG_STRAHL" (representing the hourly sum of solar incoming irradiance), "FD_STRAHL" (indicating the hourly sum of diffuse irradiance), and "MESS_DATUM_WOZ" (denoting the local time) are encapsulated (50). Such comprehensive metadata empowers the computation of daily, monthly, and even yearly solar energy estimates for specified inclined surfaces. For the purpose of a case study, we have selected a station located at Schnarrenberg near Stuttgart, characterized by a latitude of $48.8°$ and a longitude of $9.2°$.

4.2.2 Introduction to the Algorithm

As previously stated, the parameter Peak Sun Hours (PSH), represented as H_tilt, is intricately linked to the installation angle. The quest for an optimal angle becomes crucial in achieving a harmonious compromise: augmenting solar irradiance during demanding months while maintaining the effectiveness of solar energy capture across other seasons. This pursuit has led to the development of an algorithm, the graphical depiction of which is showcased in Figure 4.1.

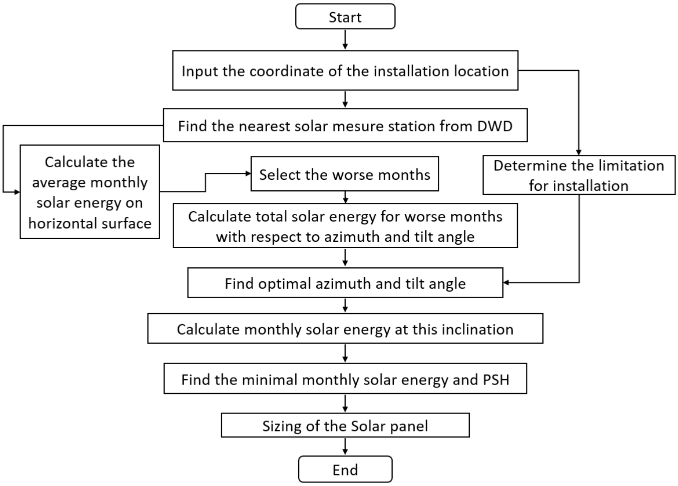

Figure 4.1: Flowchart depicting the algorithm for determining the optimal solar panel inclination and its related dimensions.
Source: Reprint from previous publication by author (2) ©2021 IEEE

The algorithm utilizes the GPS coordinates of the installation mast in Germany as input data. Concurrently, it requires historical solar irradiance data obtained from the nearest measurement station operated by the DWD. Prior to initiating the installation procedure, a comprehensive analysis of the environmental conditions surrounding the transmission tower is imperative. This assessment seeks to identify potential constraints, such as shading caused by vegetation. This information enables an informed determination of the ideal orientation for the solar panel.

The open metadata sourced from DWD furnishes historical data encompassing hourly global and diffuse solar irradiance on a horizontal surface. Consequently, it becomes feasible to compute the average monthly solar energy, which serves as a means to identify months characterized by insufficient radiation. This endeavor is vital to ensure the self-sustaining functionality of the system during the more challenging periods. Furthermore, an investigation into the cumulative solar energy during these months, with due regard to azimuth and tilt angle, is undertaken to ascertain the optimal inclination or tilt angle in conjunction with the previously determined azimuth angle. In pursuit of assessing the minimal Peak Sun Hours (PSH), the mean monthly solar energy on this inclined surface is calculated, concurrently evaluating any potential attenuation of solar energy during the remaining months. Notably, the code underpinning this study has been released as open-source [1].

4.3 Implementation and Results

For the analysis, the most recent available metadata spanning the years 2013 to 2017 is utilized. Varied inclinations corresponding to azimuth angles ranging from $0°$ to $360°$, with a resolution of $10°$, and tilt angles spanning from $0°$ to $90°$, with a resolution of $1°$, are subjected to analysis. This phase demands approximately 2 hours and is consequently the most time-intensive segment. The computations were executed on an i7-3632QM CPU 2.20GHz Intel processor. Following the selection of the optimal azimuth α and tilt angle β, subsequent calculations involving monthly solar energy as well as Peak Sun Hours (PSH) necessitated a mere 3 minutes to complete.

4.3.1 Optimal Inclination of Solar Panel

Before commencing the analysis, it is imperative to identify the months characterized by insufficient radiation. This enables the determination of the appropriate solar panel dimensions tailored to address these challenging periods. To achieve this, the average monthly global irradiance spanning the period from 2013 to 2017

---

[1] The program code can be found: git.scc.kit.edu/jw2907/self-sufficient-solar-power-supply-system

is computed. The histogram depicted in Figure 4.2 clearly highlights November, December, and January as months exhibiting notably reduced solar radiation. Consequently, devising an optimal inclination becomes paramount, ensuring the system's self-sustaining operation throughout these months.

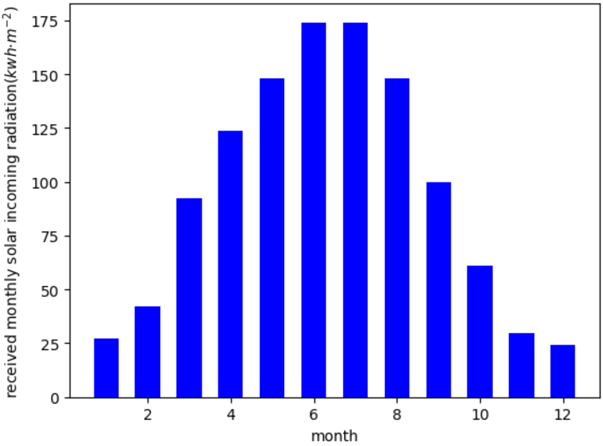

Figure 4.2: The data analysis of monthly solar global energy on a horizontal surface at the geographical coordinates of Stuttgart (Schnarrenberg) in Germany [$48.8°, 9.2°$] during the period from 2013 to 2017 indicates that the months of November, December, and January consistently exhibit the lowest levels of monthly solar radiation.
Source: Reprint from previous publication by author (2) ©2021 IEEE

As previously introduced, the KL-model proves to be the more suitable choice for estimating incoming solar energy and is thus integrated into our algorithm. This model accounts comprehensively for all diffuse components, encompassing anisotropic, circumsolar, and horizon brightening diffuses. Illustrated in Figure 4.3 is the overall incoming solar energy observed at Schnarrenberg, across varying tilt angles (β) and azimuth angles (α). This graphical representation depicts the cumulative annual energy reception during the months of November, December, and January, across diverse inclined surfaces. Evidently, optimal energy acquisition for these months necessitates a south-facing orientation, as the incoming energy at azimuth angles around 0° significantly outweighs the energy received at 180°. Furthermore, for each orientation, an optimal tilt angle can be ascertained to maximize energy capture during these periods of solar insufficiency.

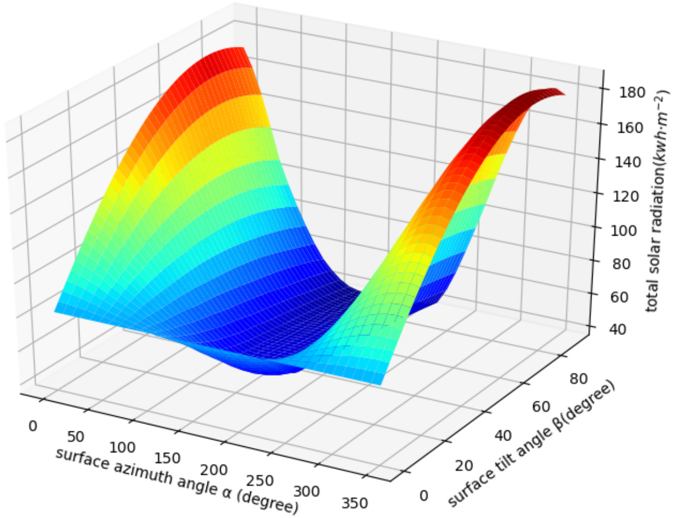

Figure 4.3: The cumulative annual solar energy influx during the months with lower solar radiation (November, December, and January) is depicted in relation to the azimuth and tilt angles of the solar panel at the Schnarrenberg location in Germany. Regions highlighted in red represent a significant accumulation of solar energy, while those shaded in blue indicate relatively lower energy levels.
Source: Reprint from previous publication by author (2) ©2021 IEEE

In Figure 4.4, the total annual energy accumulation during the months of lower solar radiation is illustrated according to variations in tilt angle (β) under the Kl-model, while the azimuth angle (α) remains fixed. Notably, a southern orientation yields the most efficient energy reception. When examining the trends of solar energy change for specific azimuth angles, namely, $\alpha = 0^\circ$, $\alpha = 30^\circ$, and $\alpha = 60^\circ$ with increasing tilt angle, a pattern emerges: energy initially rises until approximately 70°, subsequently declining. Interestingly, when solar panels are oriented toward the east (as indicated by the curves $\alpha = 90°$ and $\alpha = 120°$), solar energy diminishes with the escalation of tilt angle.

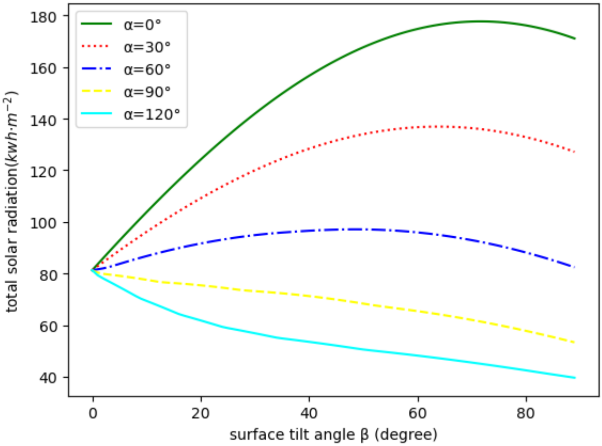

Figure 4.4: The cumulative annual solar energy sum during the months of lower solar radiation (November, December, and January) is presented with regard to the tilt angle (β), while the azimuth angle (α) remains constant.
Source: Reprint from previous publication by author (2) ©2021 IEEE

4.3.2 Peak Sun Hours

As previously indicated, the singular unknown parameter governing the solar panel dimensioning process is the Peak Sun Hours (H_{tilt}), contingent upon the orientation and tilt angle. In practical scenarios, achieving an ideal south orientation is not always feasible. Factors such as avoiding shadows cast by forests or other nearby structures might necessitate deviations. Nevertheless, for each specific azimuth angle, an optimal tilt angle can be determined. This approach ensures the system's endurance during months marked by reduced solar radiation. Given this premise, an assessment is conducted to ascertain whether this optimal inclination for the winter months might negatively impact solar energy capture during other periods.

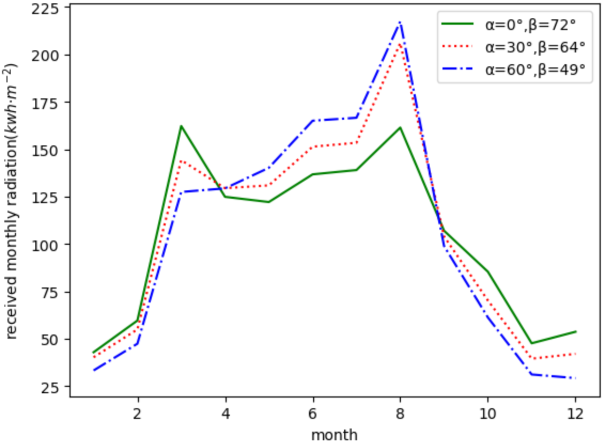

Figure 4.5: Average monthly solar energy across various inclined surfaces at Schnarrenberg, Germany. **Source**: Reprint from previous publication by author (2) ©2021 IEEE

For this assessment, three distinct inclinations have been chosen, facilitating the computation of average monthly incoming solar energy using DWD data spanning the years 2013 to 2017. Illustrated in Figure 4.5, the optimal tilt angle is selected for each azimuth angle. Remarkably, while the optimal inclination is established with regard to the winter months, namely, November, December, and January, he incoming solar energy on these inclined surfaces throughout the remaining months of the year is evidently not compromised.

The selection of PSH is aimed at aligning with the month characterized by the most limited solar radiation. This choice guarantees self-sufficient system operation during this particular period. Utilizing the findings depicted in Figure 4.5, the month with the lowest solar energy accumulation can be identified. Subsequently, by employing the open metadata from the most recent five years, the PSH value

Table 4.1: Minimum average daily Peak sun hours at Schnarrenberg
Source: Reprint from previous publication by author (2) ©2021 IEEE

$H_{tilt}(h)$	**Tilt and azimuth angle**		
Year	$\alpha = 0° \beta = 72°$	$\alpha = 30° \beta = 64°$	$\alpha = 60° \beta = 49°$
2013	0.74	0.74	1.11
2014	1.29	1.14	0.50
2015	1.23	1.15	1.26
2016	1.66	1.49	1.08
2017	2.08	1.93	0.75

(H_{tilt}) for each year is determined, as detailed in Table 4.1. While the principle suggests that the minimum value should be chosen for sizing the solar panel, discussions with our project partner led to an empirical realization that this approach is excessively conservative. Consequently, a decision was reached to adopt the average PSH value over the course of five years.

5 Semi-Autonomous Flight Assistance System for Installation Processes

In pursuit of enhanced work efficiency, heightened flexibility, and cost-effective airspace operations, Unmanned Aerial Vehicles (UAVs) have garnered widespread adoption across a spectrum of civil and industrial applications. This is particularly evident in scenarios where human assessments are arduous or time-intensive, such as geographic mapping and energy facility inspections. Within the framework of "PrognoNetz," a weather-dependent intelligent ampacity forecast system is under development, necessitating an extensive array of weather measurements spanning thousands of kilometers along overhead lines. Nonetheless, the installation and maintenance of this sensor network prove both time-consuming and resource-intensive, entailing technical personnel to scale electrical towers—a task fraught with risks and dangers. The incorporation of UAVs for this purpose offers a time-efficient and cost-effective solution, expediting the establishment of the sensor network.

However, the execution of installation tasks remains a challenge, primarily due to the UAV's susceptibility to rough hovering accuracy in the face of continuously shifting wind conditions. To enhance the stability of UAV operations, a computer-vision-based semi-autonomous flight assistance system has been developed. To achieve this, the UAV is outfitted with an onboard computer, gripper system, and depth cameras. This chapter will encompass the following aspects:

1. Prior to delving into the flight control system, the extrinsic calibration of the multi-cameras in the UAV coordinate system is carried out.

2. An autonomous navigation strategy is developed, facilitating GPS-based navigation to the installation mast, complemented by the integration of point-cloud-driven obstacle avoidance capabilities.
3. An approach algorithm is formulated, hinging on detection and pose estimation of the mounting position on the transmission tower. This algorithm aids in the installation of a cantilever.
4. A flight control algorithm is introduced, tailored for identifying the holder position on the cantilever. This serves the dual purpose of facilitating the installation and maintenance of a weather station.

5.1 Extrinsic Calibration of Multiple RGB-D Cameras and UAV with Non-overlapping Views

Depicted in Figure 5.1, the setup encompasses two vision sensors, specifically depth cameras, systematically affixed to the UAV. These cameras serve the dual purpose of environmental perception and object detection. One camera is oriented forward, serving for obstacle avoidance, and also to determine the depth and orientation of the mounting profile on the transmission tower: an essential factor in evaluating the cantilever installation. The second camera is angled downward, strategically situated to precisely identify the mounting position on the cantilever, designated for the installation of the weather station.

The selection of the Intel RealSense Depth Camera D415 is attributed to its superior depth perception capabilities. This camera model comprises an RGB sensor, a dual set of depth sensors, and an infrared projector, collectively enabling depth perception for every pixel in an image alongside RGB texture data. Moreover, the camera exhibits a compact design, lightweight construction, and

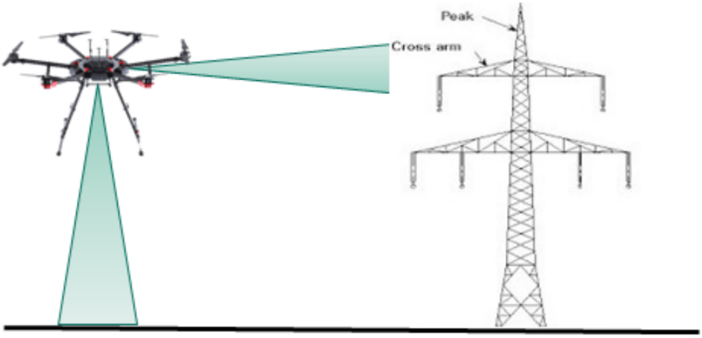

Figure 5.1: Project overview: two rig cameras, one facing forward to detect to desired mounting position and one facing down to control grippers.

cost-effectiveness. It is notably supported by a robust open-source SDK that accommodates diverse computer operating systems, such as Windows or Linux, and programming languages like C++ and Python.

The implementation of vision-based perception empowers autonomous flight, significantly aiding technical personnel throughout the installation and maintenance procedures. In order to achieve this, it becomes imperative to ascertain the relative position and orientation of mounting locations within the UAV coordinate system (UCS), thereby giving rise to the challenge of extrinsic calibration. This entails the initial observation of objects in the camera coordinate system and subsequently transforming them into the UCS. In essence, the task involves the extrinsic calibration of the rigid depth cameras to the UCS. It is imperative to highlight that, given the non-overlapping nature of the cameras' poses, it becomes essential to define the UAV coordinate system as the reference coordinate system. This facet accentuates the complexity inherent in this calibration undertaking.

Presently, studies on extrinsic calibration in scenarios lacking overlapping viewpoints are still undergoing investigation and remain non-universal in nature. In this section, a straightforward, resilient, and innovative framework will be presented, aiming to address the aforementioned challenge.

5.1.1 Related Work

The current algorithms designed to calibrate extrinsic parameters of cameras in scenarios without overlapping viewpoints can be broadly categorized into stationary and mobile methods. Stationary methods encompass extrinsic calibration algorithms tailored for static cameras or calibration targets. Conversely, mobile methods focus on calibrating moving object targets, incorporating trajectory-based or SLAM (Simultaneous Localization and Mapping) approaches.

A stationary extrinsic calibration method based on markers is introduced, wherein augmented reality (AR) markers are affixed to non-overlapping cameras. The transformation between each AR marker and its corresponding camera is established by incorporating an external camera. Consequently, the extrinsic parameters of the cameras are deduced through the marker transformations (51). Calibration patterns are strategically reflected by mirrors to ensure visibility to all cameras, thereby facilitating the extrinsic calibration of non-overlapping multi-cameras. This innovative approach leverages the utilization of reflected and overlapped patterns to achieve successful calibration (52)(53). Calibration patterns such as Graycode or lines are projected onto a wall or plane using a projector. The extrinsic calibration of non-overlapping multi-cameras is achieved by optimizing the pose of the plane and cameras within the projector coordinate system through bundle adjustment (54)(55).

During movement, mapping for each camera is established using visual Simultaneous Localization and Mapping (vSLAM) by capturing synchronized image sequences. The camera poses are subsequently determined within the merged mapping, where adjacent camera poses share the Field of View (FOV) across different frames (56)(57). Pose graph-based SLAM is implemented to estimate the camera trajectory with the aid of an additional monocular camera. This approach enables the determination of poses for non-overlapping cameras through visual odometry (58). Calibration patterns, exemplified by two stationary chessboards, are tracked during dynamic movement. Non-linear optimization and perspective-n-points techniques are harnessed to accurately determine and optimize the extrinsic parameters of cameras (59).

Within stationary approaches, the precise determination of the mirror or projector's position and orientation significantly impacts the calibration outcome. Concurrently, for certain dynamic methods, ensuring the synchronization of calibration sensors is imperative. Additionally, the mitigation of accumulated error and motion blur during SLAM or trajectory estimation presents considerable challenges, demanding stringent methodological requirements. Furthermore, it is noteworthy that the prior research endeavors are incapable of conducting extrinsic calibration for both rigid cameras and UAV configurations.

5.1.2 Methodology and Implementation

The algorithm proposed in this study utilizes the additional camera to generate overlapping with both depth cameras. Additionally, it employs the bundle adjustment technique to construct a 3D mapping of the calibration scenario. This mapping encompasses the spatial coordinates of all feature points while enhancing the accuracy of camera poses from various viewpoints. Specifically, this process involves determining the relative transformations $\mathrm{R_i}$ and $\overrightarrow{t_i}$ for both cameras and the UCS across each frame within the 3D structural framework. The primary objectives of the extrinsic calibration process are as follows, as depicted in Fig. 5.2:

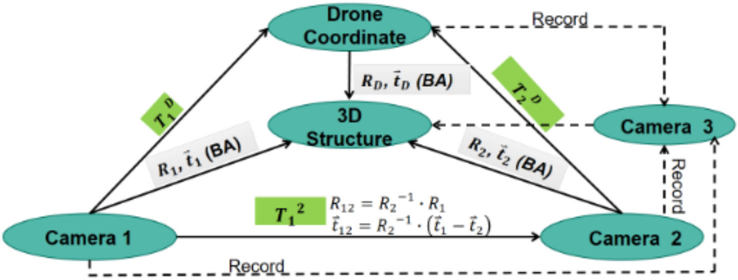

Figure 5.2: Overview of the Configuration
Source: Reprint from previous publication by author (3) ©2022 IEEE

1 Establish the extrinsic parameters T_1^2, which denote the transformation between two rigid depth cameras.

2 Define the UAV Coordinate System (UCS) and estimate the extrinsic parameters $\mathrm{T}_1^{\mathrm{D}}$ and $\mathrm{T}_2^{\mathrm{D}}$. These parameters delineate the transformations from the individual camera coordinate systems to the UCS.

5.1.2.1 Calibration Pattern and Data Processing

Before commencing calibration, the selection of appropriate calibration patterns is of paramount importance. Given the tight affixation of the depth cameras onto the UAV during flight, calibration can be undertaken under labor conditions with specified calibration patterns. The widely utilized checkerboard pattern is also incorporated in our study, owing to its extensive use in image processing for several decades. This pattern allows for custom-sized configurations and benefits from well-established toolboxes. However, the detection of feature points, such as corners, lacks inherent directionality, which introduces the challenge of establishing spatial relationships across different frames and cameras.

To tackle this challenge, a QR code is affixed to a specific corner of the checkerboard, as depicted in Figure 5.3. This strategic placement ensures that the detection process consistently commences from the point nearest to the QR code, followed by sequential enumeration from rows to columns. Additionally, the customized content encoded within this QR code is utilized to label and organize the numerals assigned to feature points originating from diverse cameras. This labeling aids in establishing the spatial relationships among these points. Subsequently, the 3D mapping is constructed by minimizing the projection errors in relation to the corresponding world coordinates.

As depicted in Figure 5.4, appropriately sized calibration patterns are positioned within the Field of View (FOV) of both the forward- and downward-facing cameras. Notably, these patterns do not overlap with each other. To address this intricate challenge, a transformation is made to convert the non-overlapping calibration into a traditional overlapping calibration by introducing an additional

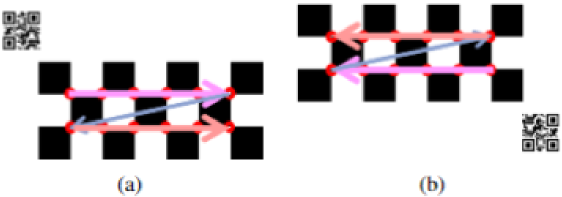

Figure 5.3: To overcome the directional challenge associated with the feature points on the calibration patterns, the corner detection process commences from the corner closest to the QR code and advances in a sequential manner along rows and subsequently columns.
Source: Reprint from previous publication by author (3) ©2022 IEEE

camera. This supplementary camera creates overlapping viewpoints with both the cameras and the UAV. Data is recorded in the form of bag format files while the UAV and cameras remain stationary. Simultaneously, the additional camera is moved continuously to facilitate data recording, ensuring that the patterns and calibration targets remain within its FOV for visibility. Leveraging the detection of feature points, their corresponding 3D depth coordinates are extracted from the respective 2D pixel positions on the RGB image. This alignment is achieved by invoking the specified function from the "pyrealsense2" library, as the RGB-D cameras undergo rectification and intrinsic calibration by the manufacturer.

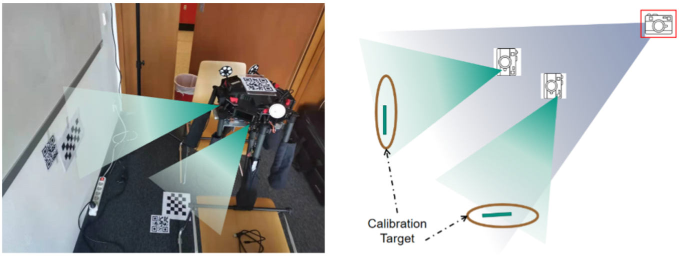

Figure 5.4: The setup of multi RGB-D cameras on the UAV with non-overlapping, the extrinsic calibration is transformed to overlapping calibration by adding an external camera.
Source: Reprint from previous publication by author (3) ©2022 IEEE

5.1.2.2 Three-dimensional Reconstruction: Bundle Adjustment Algorithm

The Bundle Adjustment algorithm is employed to optimize the 3D coordinates representing the scenario while concurrently refining the camera poses. This optimization process aims to minimize the re-projection error, as outlined in (60). The cost function is established using the squared Mahalanobis distance in the form of a covariance matrix. This function characterizes the pixel deviation between the re-projected and measured pixel locations of feature points on the image plane (61).

In this optimization procedure, the optimization parameters encompass the world coordinates of feature points (x_j, y_j, z_j) and the poses of respective cameras at various frames, including the Rotation matrix $\mathrm{R_i}$ and the translation vector $\overrightarrow{t_i}$. In this approach, the cost function is defined as the sum of the variance of Euclidean distance and is presented mathematically as follows:

$$\min_{\mathrm{a_{ij},w_j}} \sum_{\mathrm{i}}^{\mathrm{N}} \sum_{\mathrm{j}}^{\mathrm{M}} \mathrm{E}, \tag{5.1}$$

$$\mathrm{E} = \mathrm{v_{ij}} \left\| \mathrm{R_i} \cdot (\mathrm{x_{ij}}, \mathrm{y_{ij}}, \mathrm{z_{ij}})^{\mathrm{T}} + \overrightarrow{t_i} - (\mathrm{x_j}, \mathrm{y_j}, \mathrm{z_j})^{\mathrm{T}}) \right\|^2 \tag{5.2}$$

Here, N represents the total number of frames from both mounted and additional cameras, while M denotes the number of feature points in the calibration scenario. The coordinates of point j at frame i in the camera coordinate system are presented as (x_{ij}, y_{ij}, z_{ij}), and (x_j, y_j, z_j) denotes the 3D coordinates of point j in the reconstructed system.

The extrinsic parameters comprise the rotation matrix $\mathrm{R_i} \in \mathbb{R}^{3\times3}$, which is defined by three Euler angles (α, β, γ), and the translation vector $\overrightarrow{t_i} = [\mathrm{t_{xi}}, \mathrm{t_{yi}}, \mathrm{t_{zi}}]^{\mathrm{T}}$, representing the camera pose at frame i with respect to the reconstructed 3D mapping. The binary variable $\mathrm{v_{ij}}$ is equal to 1 if point j at frame i is observed, and 0 otherwise.

5.1.2.3 Determination of Extrinsic Parameters

In the context of the extrinsic calibration between the UAV and depth cameras, the establishment of the UCS holds crucial importance. In our methodology, all calibration targets remain stationary except for the additional camera. As a result, the determination of the vehicle's coordinate system is achieved through known flight control commands. For example, moving along the X-positive direction corresponds to the vehicle moving forward, while movement along the Y-positive direction corresponds to the vehicle banking right. To accomplish this, a QR code is employed and affixed to the center of the top surface of the UAV, as depicted in Figure 5.4.

As depicted in Figure 5.5, the external camera detects and captures the three corners of the QR code. The positive directions of the axes $\vec{OX}$ and $\vec{OY}$ are oriented perpendicular to each other, aligning precisely with the requirements of UAV flight control. Similarly, the determination of the z-axis follows the right-hand rule. Upon completing the 3D reconstruction, the world coordinates of the corners—namely, the Origin O, X, and Y are established. Thus, the UCS is defined as:

$$\vec{X_0} = \frac{\vec{OX}}{\left|\vec{OX}\right|}, \vec{Y_0} = \frac{\vec{OY}}{\left|\vec{OY}\right|} \tag{5.3}$$

$$\vec{Z_0} = \vec{X_0} \times \vec{Y_0} \tag{5.4}$$

Clearly, the origin coordinate O signifies the translation $\overrightarrow{t_D}$ from the UCS to the reconstructed mapping. Additionally, the rotation matrix $\mathrm{R_D}$ can be defined to align with the specifications of UAV control:

$$\vec{t_D} = (x_0, y_0, z_0)^T \tag{5.5}$$

$$R_D = (\frac{\vec{OX}}{\left|\vec{OX}\right|}, \frac{\vec{OY}}{\left|\vec{OY}\right|}, \frac{\vec{OZ}}{\left|\vec{OZ}\right|})^T \tag{5.6}$$

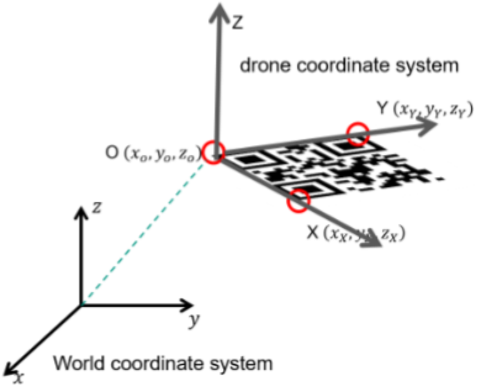

Figure 5.5: The QR code's corners define the Unified Coordinate System (UCS) on the UAV's upper part. Through 3D reconstruction, we obtain the world coordinates of these corners, enabling the calculation of the transformation between the UAV's and world coordinate systems.
Source: Reprint from previous publication by author (3) ©2022 IEEE

Upon applying the bundle adjustment, the optimized and refined camera poses in the reconstructed mapping are obtained. Consequently, the extrinsic parameters of both depth cameras, denoted as $\mathrm{T}_{\mathrm{i}}^{\mathrm{D}}$ (where $i = 1, 2$), can be deduced as follows. These parameters describe the transformation from the respective camera coordinate system to the UCS:

$$\mathrm{T}_{\mathrm{i}}^{\mathrm{D}} = \begin{bmatrix} R_D & \vec{t_D} \\ 0^T & 1 \end{bmatrix}_{4\times4}^{-1} \cdot \begin{bmatrix} \mathrm{R}_{\mathrm{i}} & \overrightarrow{t_i} \\ 0^T & 1 \end{bmatrix}_{4\times4} \tag{5.7}$$

Simultaneously, the transformation T_1^2 between the two depth cameras can also be determined. This transformation comprises the rotation matrix R_{12} and the translation vector $\overrightarrow{t_{12}}$ as follows:

$$R_{12} = {R_2}^{-1} \cdot R_1 \tag{5.8}$$

$$\vec{t_{12}} = R_2^{-1} \cdot (\vec{t_1} - \vec{t_2}) \tag{5.9}$$

With the cost function defined for this optimization problem and the extraction of extrinsic parameters completed, the proposed method will be subjected to evaluation through various experiments.

5.1.3 Experimental Evaluation and Results

The aforementioned extrinsic calibration method has been implemented and evaluated on a vehicle equipped with vision sensors. The computational time for this implementation is approximately 3 minutes on an Intel Core i7-8700K processor. Additionally, the approach has been tested using different camera rig configurations to assess its reliability, robustness, and redundancy against noise.

5.1.3.1 3D Scene Reconstruction: Bundle Adjustment

For the calibration procedure, a total of 20 frames were captured using the external camera while in motion, and 3 frames were captured using static calibration cameras. These frames were utilized to construct the 3D mapping of the environment, resulting in the detection of 38 globally associated feature points from the two calibration patterns and the QR-code on the UAV. The acquired spatial relationships are crucial and indicative of the effectiveness of the approach, as depicted in Figure 5.6.

As previously indicated, the feature points on the checkerboards are visible and recorded by the external camera. Consequently, the feature points captured by both depth cameras can be projected onto the image plane of the additional camera to assess the accuracy of the transformation. As depicted in Figure 5.7, the precise and correct re-projection of the red points substantiates the optimization and reliable calibration of the camera poses.

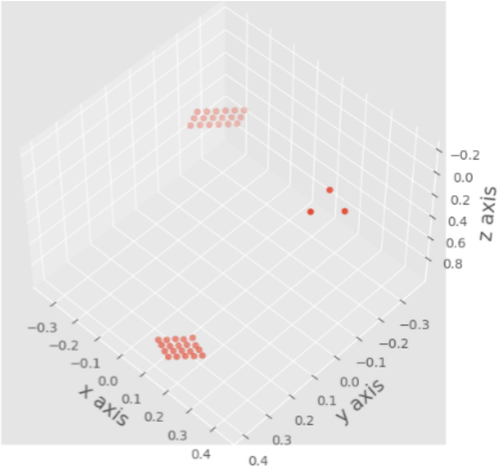

Figure 5.6: The 3D reconstruction outcome achieved through the bundle adjustment process is presented in meters.
Source: Reprint from previous publication by author (3) ©2022 IEEE

Furthermore, an error model is necessary to estimate and visualize the accuracy of the extrinsic parameters. Given the non-intuitive nature of representing reprojected deviations in pixels on the image plane, we opt for the use of backward projection error. In this context, the spatial discrepancy between the 3D reconstructed coordinates and their corresponding projected camera points is analyzed with respect to the extrinsic parameters.

The spatial distribution of backward projection error in meters is depicted in Figure 5.8. According to the specifications of the Realsense D415(62) product, the depth accuracy is within 2% at a depth perception of 2 meters during the data recording, corresponding to 40 mm. The accuracy and reliability of our algorithm are thus validated, with a mean Euclidean distance of projection error at 2.17 mm. Moreover, the standard deviation is approximately 1.96 mm, underscoring the accuracy of the estimated extrinsic parameters for determining camera poses across different frames and viewpoints. This accuracy is evident in the minimal

Figure 5.7: Reprojection of the identified corners of the calibration patterns from the RGB-D camera rig onto the image plane of the external camera.
Source: Reprint from previous publication by author (3) ©2022 IEEE

deviation of projected feature points at their desired spatial positions within the 3D mapping.

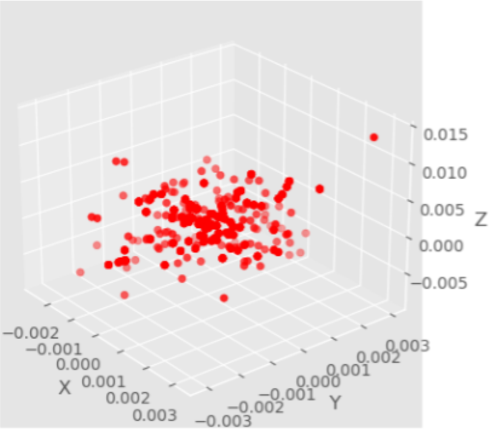

Figure 5.8: The distribution of the 3D calibration backward projection error in meters.
Source: Reprint from previous publication by author (3) ©2022 IEEE

5.1.3.2 Evaluation of the Approach

Various experiments are conducted without the utilization of UAV to assess the general feasibility of this calibration method.

5.1.3.2.1 Redundancy Analysis

In the redundancy analysis, the algorithm is subjected to testing across four distinct setups of multi-camera rig configurations. Illustrated in Figure 5.9, the investigation encompasses the following mounting orientations: parallel, orthogonal without overlapping field of view (FOV), opposite, and orthogonal with overlapping FOV. The resulting mean and standard deviation of the backward projection error are tabulated in Table 5.1. Evidently, the mean Euclidean deviations are approximately 2 mm, accompanied by a standard deviation of roughly 1.5 mm. This consistent performance across redundant experiments underscores the efficacy of our approach in addressing the calibration challenge, spanning both overlapping and non-overlapping camera setups.

Table 5.1: Results of 4 different setups
Source: Reprint from previous publication by author (3) ©2022 IEEE

Backward Projection Error	Mean	Standard Deviation
msetup a	1.777 mm	1.413 mm
msetup b	1.911 mm	1.556 mm
msetup c	2.512 mm	1.545 mm
msetup d	2.123 mm	1.518 mm
mean of setups	2.081 mm	1.508mm

Furthermore, the robustness against the noise during the movement of the external camera and data record is evaluated. A set of independent tests are executed on the fixed camera setup (a) in Figure 5.9. The positions of calibration patterns and viewpoints of the external camera are changed, to observe if the translation matrix

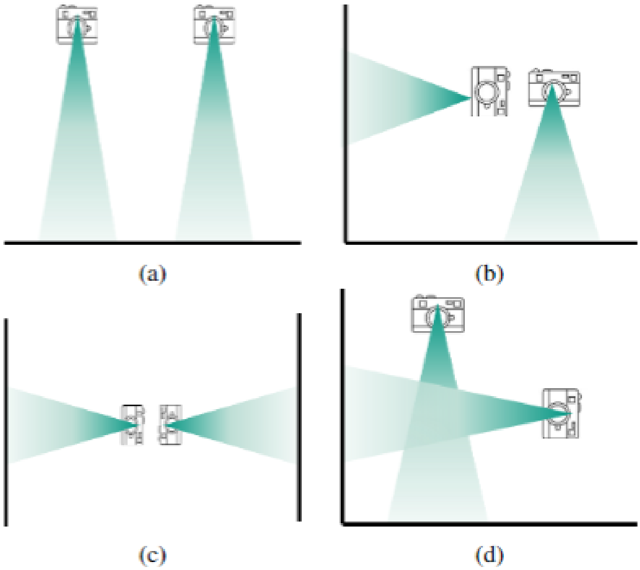

Figure 5.9: Four setups of two RGB-D cameras: (a) parallel, (b) orthogonal with non-overlapping FOV, (c) opposite, (d) orthogonal with overlapping FOV.
Source: Reprinted from previous publication by the author (3) ©2022 IEEE

T_{12} between camera rig deviates or not. The results are consistent, which means that our calibration algorithm is rough and stable against noise and motion blur.

5.1.3.2.2 Stability Analysis

During the course of experiments, observed variations in the calibration outcomes can be attributed to the utilization of differing numbers of frames from the external camera. This variability can be attributed to multiple factors, one of which is the inherent uncertainty associated with depth perception, as the accuracy of infrared-based depth measurements is contingent upon the reflective characteristics of surfaces and the prevailing environmental conditions. Additionally, the occurrence of motion blur resulting from the movement of the external camera represents another plausible contributing factor. As a consequence, it becomes imperative to investigate the impact of the number of frames employed on the calibration outcome. Furthermore, an exploration into the requisite number of frames needed to achieve consistent and reliable results is warranted.

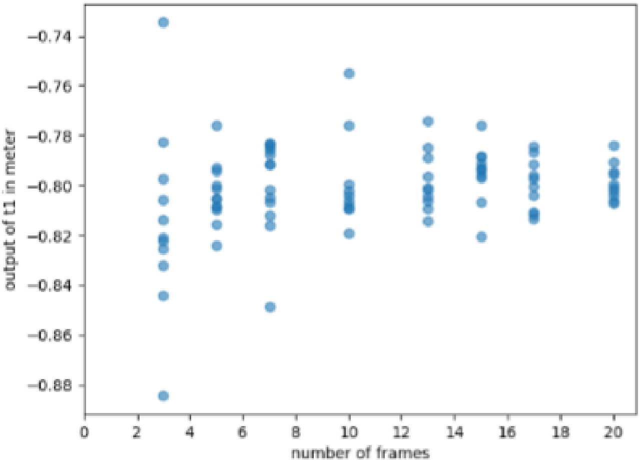

Figure 5.10: The effect of the number of frames from the external camera on calibration stability is depicted in Figure 5.10. Each blue point represents the t_1 value of the translation vector $\vec{t_{12}}\,(t_1, t_2, t_3)$ after an individual test using the specified number of frames.
Source: Reprint from previous publication by author (3) ©2022 IEEE

In the conducted stability analysis, a total of 10 independent tests were performed for varying numbers of frames, namely, 3, 5, 7, 10, 13, 15, 17, and 20 to assess their impact on calibration stability. The variable under investigation was the spatial displacement t_1 along the x-axis of the translation vector $\vec{t_{12}}\,(t_1, t_2, t_3)$. The outcomes of this investigation are illustrated in Figure 5.10, where individual blue data points represent the calibration results of t_1 obtained from each specific test employing the designated number of frames. Evidently, as the number of frames employed in the calibration process increases, the calibration outcomes converge and exhibit greater concentration around a specific value.

5.2 Autonomous UAV Navigation System for Target GPS Coordinates with Point Cloud-Based Obstacle Avoidance Capability

Given that certain transmission towers are situated in rugged terrains, such as mountains, river valleys, and dense forests, and coupled with the complexities associated with controlling UAV orientation (including rotation), challenges arise for pilots in accurately determining the direction of installation mast. Consequently, the task of manually installing or maintaining sensor networks remains demanding. Therefore, the involvement of UAVs offers a convenient solution, as technical personnel can oversee and manage UAV operations from suitable ground stations, allowing for remote control and inspection. To address the challenges posed by UAV flight control beyond direct line of sight, the development of an autonomous navigation system tailored to guide the UAV towards target GPS coordinates becomes instrumental in supporting pilots during operational tasks.

In this work, an autonomous navigation system with obstacle detection, avoidance, and path-finding ability is proposed for outdoor applications, owing to the fact that the ambient environment is previously unknown and long-range operation is necessary. The vehicle is aimed to orient itself toward the target location autonomously and continuously, even though the UAV may deviate from the target direction due to obstacle avoidance and the necessity to select a suitable flight direction and path. The corresponding work is divided into the following parts:

1. **Point Cloud-Based Detection and Classification:** This phase involves employing point cloud data for the identification and categorization of different objects.
2. **Collision Detection and Path-Finding:** The system incorporates mechanisms for detecting potential collisions and determining alternative flight paths considering various directions around and behind the nearest obstacle.

3. **Voting Mechanism for Flight Decisions:** A voting mechanism is implemented to make informed decisions regarding suitable flight paths based on a consensus among the system components.
4. **Experimental Evaluation:** The efficacy of the proposed system is assessed through a series of experiments conducted in both simulated and real-world scenarios.

5.2.1 Related Work

Autonomous navigation primarily comprises two distinct components: obstacle detection and path planning. Historically, these components have been extensively investigated as separate entities across various applications.

5.2.1.1 Obstacle Detection

An autonomous system for obstacle detection and avoidance is implemented on a quadrotor platform, which is equipped with a monocular camera (63, 64). To facilitate this capability, a Convolutional Neural Network (CNN) is employed to learn and estimate depth information from the input RGB image. This estimated depth information is then utilized for obstacle detection and collision avoidance through C-space expansion(65). Furthermore, a Faster Region-based Convolutional Neural Network (Faster R-CNN) is trained to detect and recognize tree trunks (66).

For similar objectives, a more efficient MobileNet-SSD CNN model, in contrast to the Faster R-CNN, is implemented for GPS-denied outdoor scenarios, utilizing the Single-Shot Multibox Detection (SSD) network architecture (67). In this context, a Scale-Invariant Feature Transform (SIFT) detector is employed to extract distinctive feature points from the image plane. Subsequently, the obstacle area ratio, comprising the distribution of these feature points, is compared with the UAV's position to ascertain the possibility of an impending collision in the designated flight direction (68).

The application of the DBSCAN (Density-Based Spatial Clustering of Applications with Noise) algorithm is employed to identify and categorize point clouds into distinct clusters or individual obstacles. These point clouds are acquired via millimeter-wave radar technology (69). Moreover, other researchers have also harnessed depth sensors for point cloud acquisition in the context of obstacle detection. For instance, depth cameras (70) and LiDAR systems (71) are employed for this purpose.

5.2.1.2 Path Planning

A control strategy has been devised to ensure collision avoidance with trees. The height of trees captured in images is utilized to estimate the distances between trees based on their image width, along with calculating their distances from the UAV. This approach aims to determine the most substantial free space available. Obstacles' spatial positioning relative to the UAV is categorized as either "critical" or "warning," influencing the control algorithm's behavior (64). Through the estimation of obstacle positions and areas in the image plane, the largest unobstructed area amidst obstacles is identified as the free space for collision avoidance (68). Similarly, edge information is harnessed for obstacle detection and characterization, enabling the perception of available free space for making informed flight decisions (72).

A safety zone comprised of multiple spheres with a uniform diameter is positioned in front of the UAV, enabling the detection of the nearest obstacle through point cloud analysis. An alternate path is sought by systematically scanning the surrounding space using an ellipse detector, facilitating the selection of an appropriate escape direction (73). Addressing the UAV's 3D navigation freedom, an adaptive path planner is employed in conjunction with conventional methods like D* Lite (74) or RRT (75).

5.2.2 Implementation

The implementation of autonomous flight control is partitioned into two distinct stages: the initial detection and classification of the point cloud into individual obstacles, often organized as clusters; and the subsequent assessment of the most optimal flight direction, encompassing both the vicinity and potential obstacles positioned behind the nearest detected obstacle. Additionally, a Graphical User Interface (GUI) is developed to provide real-time visualization of the ongoing detection outcomes, flight control determinations, and the current operational state of the UAV.

5.2.2.1 Simulation Environment Setup

For achieving flight automation, video-based control algorithms are being developed to detect mounting positions and avoid obstacles. Before conducting field tests, it is essential to initially assess and refine the algorithm within a simulation environment. This approach is crucial for identifying and mitigating potential issues and risks. Within the simulation, the high-voltage infrastructure, including transmission towers and power lines, along with surrounding objects such as trees and buildings, are replicated and simulated to scale.

As depicted in Figure 5.11, the simulations are conducted within the Sphinx environment, a component of the Gazebo platform. This environment facilitates the replication of flight dynamics and sensor data for the vehicle. ROS nodes are meticulously set up to mimic the behavior of the manufacturer's onboard node (onboard SDK-ROS). This configuration allows for the validation and visualization of flight control algorithms within the simulation. Importantly, these algorithms can subsequently be directly applied to the physical DJI M600 Pro platform. In this context, the virtual camera and LiDAR configurations in the simulation are replaced with actual depth cameras, along with their corresponding ROS topics. This alignment ensures that visual and depth data, including RGB images, depth images, and point clouds, are accessible in both the simulation and the physical environment.

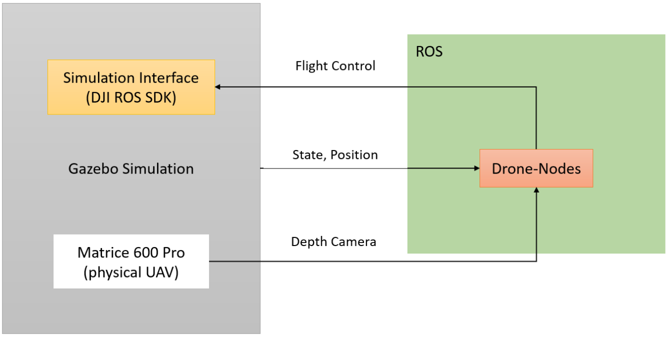

Figure 5.11: In Gazebo, the DJI Onboard SDK-ROS's Onboard Node is actively determining object positions and depths, whether from simulations or real depth cameras. It sends control commands to the drone via ROS, functional in both simulation and real drone scenarios.

In Figure 5.12, the graphical configuration of the simulation environment is depicted. It showcases the integration of real-scale high-voltage installations, the accurate 3D representation of the vehicle, and the presence of sensors such as 2D and 3D cameras/Lidar, IMU, and GPS on the vehicle. Additionally, a simulated flight controller is set up, allowing for manual operation of the physical UAV. This setup facilitates a semi-autonomous flight mode where manual and autonomous controls are interlinked. This configuration grants technical staff the ability to activate or deactivate the flight assistant system as needed, ensuring safety at all times.

5.2.2.2 GPS-based Navigation

Before the commencement of a mission, the designated target location is specified as GPS coordinates. Throughout the mission, the algorithm continuously assesses whether the UAV has achieved the target position and whether its current heading direction aligns with the target direction. To facilitate this assessment, the algorithm computes the included angle, which is essential for controlling the UAV's rotation around the yaw axis. The procedural depiction of this process is illustrated in Figure 5.13.

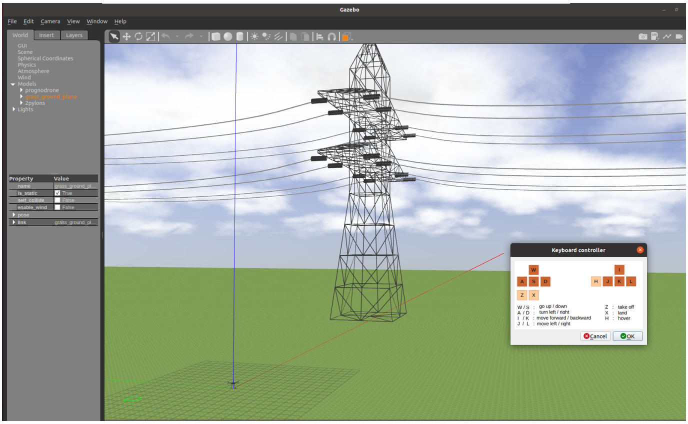

Property	Value
name	grass_ground_pl...
is_static	☑ True
self_collide	☐ False
enable_wind	☐ False
pose	
link	grass_ground_pl...

W / S : go up / down
A / D : turn left / right
I / K : move forward / backward
J / L : move left / right
Z : take off
X : land
H : hover

Figure 5.12: The simulation environment encompasses a comprehensive representation, including a 3D model of the vehicle, high-voltage power lines, transmission towers, as well as simulated 2D and 3D cameras/Lidar, IMU, GPS units, and remote controllers.

The prevailing GPS coordinates of the UAV can be acquired by subscribing to the relevant ROS topic, specifically which is disseminated by the onboard GPS module. Given the designated target location, the vector connecting the current position to the target can be mathematically represented as expressed in Equation 5.11, where x signifies the longitude and y symbolizes the latitude:

$$\nu_{\overrightarrow{drone2tar}} = (x_{target} - x_{drone}, y_{target} - y_{drone}) \tag{5.10}$$

The present heading direction of the UAV can be retrieved using the Subscriber function in ROS, specifically from the topic This topic transmits the rotation of the vehicle body in the geographic coordinate system as a quaternion message, using North as the reference direction. This information is provided by the calibrated electronic compass sensor onboard the UAV. Consequently, it is imperative to convert the quaternion representation to Euler angles. For instance, an orientation of 30° signifies that the UAV's heading is directed towards the northeast. The angle between the vectors $\nu_{\overrightarrow{drone2tar}}$ and $\nu_{\overrightarrow{heading}}$ can be derived using the inverse cosine function as follows:

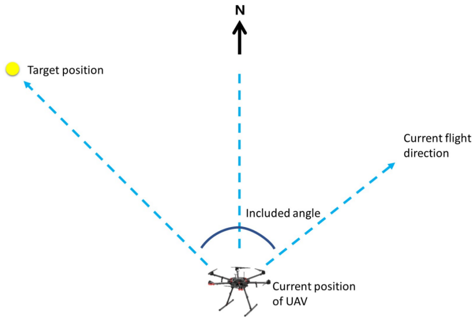

Figure 5.13: The determination of the required rotation angle is essential to align the UAV with the target location. This calculation is based on the UAV's current heading direction and the GPS coordinates of the target.
Source: Reprint from previous publication by author (5) ©2022 IEEE

$$cos\varphi = \frac{\nu_{drone\vec{2}tar} \cdot \nu_{hea\vec{d}ing}}{\left|\nu_{drone\vec{2}tar}\right| \cdot \left|\nu_{hea\vec{d}ing}\right|} \tag{5.11}$$

While Equation 5.11 provides the rotation angle, it does not specify the rotation direction, which remains a necessary determination. To address this, the cross product of the vectors resolves the issue of rotation direction, as depicted in Equation 5.12. Specifically, a positive sign denotes that the target is situated on the left side of the vehicle.

$$\nu_{drone\vec{2}tar} \times \nu_{hea\vec{d}ing} = x_{heading} \cdot y_{drone2tar} - x_{drone2tar} \cdot y_{heading} \tag{5.12}$$

5.2.2.3 Point Cloud-based Obstacle Classification

The point cloud processing pipeline for detecting and classifying different objects can be subdivided into the following sequential steps, as illustrated in Figure 5.14.

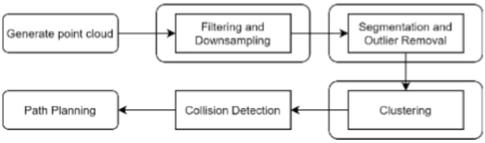

Figure 5.14: Workflow of the UAV obstacle avoidance system
Source: Reprint from previous publication by author (5) ©2022 IEEE

Given that the object classification is independent of texture features such as color, a regular uniform down-sampling approach is employed as a preprocessing step. Moreover, the point cloud's region of interest is defined along the x-, y-, and z-axes, and points falling outside this spatial range are excluded. This step contributes to reducing processing time and enhancing efficiency. Given the UAV's extensive ground-level operations, the detection and characterization of ground features is crucial. The ground is approximated as a flat plane mathematically, and the RANSAC (Random Sample Consensus) algorithm is employed for parameter estimation of the ground model and iterative removal of outliers (76). It is important to note that certain obstacles may also exhibit planar features, such as buildings or towers. In such cases, these points need to be retained rather than removed during the ground removal process.

To effectively cluster the entire point cloud and differentiate between various obstacles, the k-d tree method (77) is employed to assign point indices, enabling rapid identification of neighboring points. Subsequently, an algorithm based on Euclidean distance is utilized for range searches. It is necessary to establish clear criteria for defining these clusters, specifically the maximum distance range d_{th} . Clusters are defined based on the following criterion: for any point $\boldsymbol{p}_i$ in cluster O_i, if the distance to any point $\boldsymbol{p}j$ in cluster O_j is greater than dth (78), a cluster boundary is established:

$$min\left\|\boldsymbol{p}_i - \boldsymbol{p}_j\right\| \geq d_{th} \tag{5.13}$$

5.2.2.4 Flight Decision and Execution

During autonomous flight, a continuous detection process is employed to determine if obstacles are present within the current flight direction within a predefined distance range. This stage is referred to as the Pre-detector. Subsequently, the Mid-detector is utilized to explore and identify free space around the nearest obstacle in specific search directions. Finally, the Post-detector is employed to further detect obstacles behind the free space area defined by the mid-detector. As depicted in Figure 5.15, for each detector, a "safety volume," represented by a rectangular box, is positioned at a predetermined perception distance and direction. The length of this safety volume is customized and dependent on the depth perception capabilities of the sensors used.

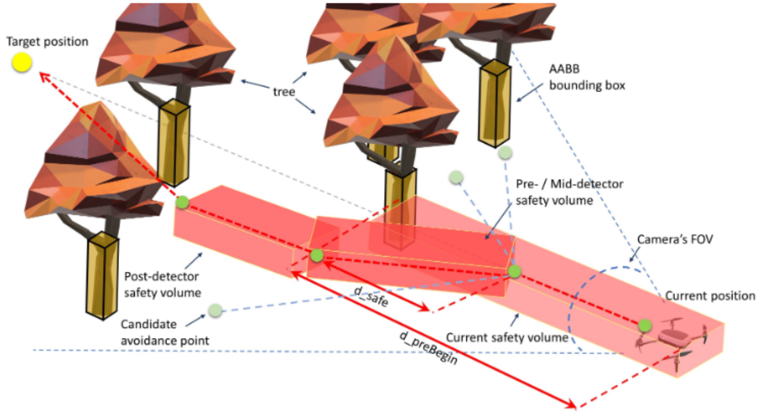

Figure 5.15: Flight decision involves a sequential process: Pre-detectors identify the nearest obstacle ahead; Mid-detector scans for free space around this obstacle; Post-detector then checks for obstacles behind the detected free space.
Source: Reprint from previous publication by author (5) ©2022 IEEE

5.2.2.4.1 Pre-detector

As previously mentioned, the Pre-detector is utilized to identify obstacles along the current flight direction. When the designated "safety volume" in front of the vehicle is obstructed, the algorithm directs the flight towards the closest point to the obstacle. This positioning enables the exploration of an escape space within a $60°$ range surrounding the nearest obstacle. This range is particularly crucial when the field of view (FOV) is significantly limited or obscured due to the vehicle's proximity to an obstacle. For clarity, several statements are introduced to elucidate the algorithm, as depicted in Figure 5.16:

- *d_safe*: the safe closest distance to the nearest obstacle. It is determined by the dimensions of the UAV and is crucial for collision avoidance.
- *d_minDistance*: the current distance to the nearest obstacle.
- *d_preBegin*: the length of the $predefined\ safety\ volume$
- *d_preEnd*: the minimum distance required within the camera's field of view to facilitate the detection of an escape space spanning a $60°$ range around the nearest obstacle. The value of d_{preEnd} is derived from the following formula (Equation 5.14):

$$d\_preEnd = d\_safe \cdot \tan \pi/3 \cdot \tan \pi/3 = 3d\_safe \tag{5.14}$$

When the UAV is situated at a distance corresponding to *d_minDistance*, signifying the presence of an obstacle within the *safety volume*, and the UAV remains considerably distant from the range defined by *d_preEnd*, the pre-detector phase becomes pivotal. This phase is focused on the identification and assessment of escape spaces encompassing a $60°$ angle around the obstacle, positioned at a distance of *d_safe*. This evaluation is carried out independently in four distinct directions: Up, Down, Left, and Right. The utilization of the flexible-collision-library/fcl (79) is integral to this process. It facilitates collision detection by translating and rotating the *safety volume* in the designated direction and distance. Consequently, the collision function is executed with individual obstacles represented as rectangular boxes. During this stage, the identification of the most spacious available

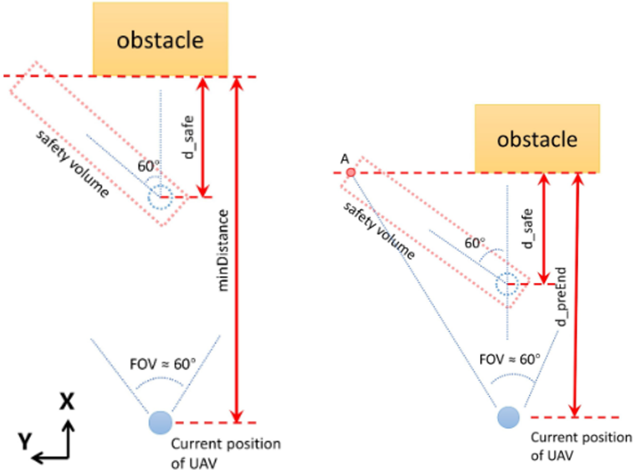

Figure 5.16: The operational range of the pre-detector is defined as *d_preBegin   d_preEnd*.
Source: Reprint from previous publication by author (5) ©2022 IEEE

escape spaces in the specified directions is carried out by assessing the 2D free area surrounding the bounding box of the obstacle in the front view. As the UAV approaches, a forward flight motion is initiated, while the decision-making process for path-finding at each frame is quantified in the decision array labeled as $vote$.

5.2.2.4.2 Mid-detector

The mid-detector is activated when the distance *d_minDistance* lies within the range defined by *d_preBegin* and *d_preEnd*. Similar to the pre-detector, the mid-detector assesses potential escape directions. In this case, it focuses on 30° detection directions located at a distance of *d_safe* in advance as the UAV approaches. The top view of the mid-detector's principle is depicted in Figure 5.17. However, within the *d_safe* distance, there is a possibility that the field of view (FOV) could be obstructed by the obstacle's dimensions, potentially compromising the assurance of collision avoidance. To address this, it is crucial to maintain a secure distance from obstacles and to ensure continuous obstacle perception as an integral part of the system's execution.

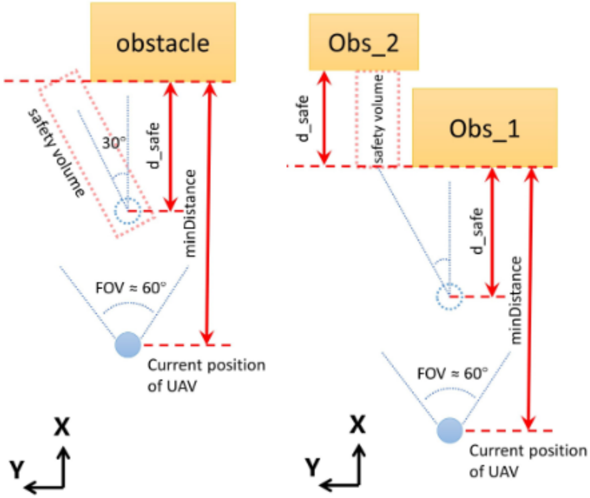

Figure 5.17: Top view of the detection principle: Illustration of the safety volume employed for collision detection by the Mid-detector (left) and the Post-detector (right).
Source: Reprint from previous publication by author (5) ©2022 IEEE

5.2.2.4.3 Post-detector

Following the execution of the pre- and mid-detector stages, potential flight directions can be identified. However, a scenario exists in which the vehicle might become immediately obstructed by an obstacle situated behind the identified free space, therefore a precautionary measure is taken to avoid such an occurrence. This is achieved through the utilization of the post-detector, which conducts supplementary collision detection activities beyond the designated free space. The detection principle is visually represented in the top view depicted in Figure

5.17. Notably, a decision is recorded in the $vote$ array exclusively when no collision is detected subsequent to the comprehensive evaluation conducted after the post-detector.

5.2.2.4.4 Decision-making

During the approach phase, decisions at each frame are recorded in the vote array. As depicted in Figure 5.18, an illustrative example showcases the decision "L30" receiving the highest vote count of 14. This signifies that the specific direction denoted by "L30" has been selected as the most viable flight path in 14 instances due to the absence of obstacles. In the provided table, the notations *L, R, U, D* signify four distinct searching directions. The numerical value following each letter denotes the angle of the search direction around the nearest obstacle. To ensure expeditious and real-time detection, the exploration of flight possibilities is confined to 30° and 60° directions.

L30	L60	R30	R60	U60	D60
14	3	0	2	0	0

Figure 5.18: An illustrative example of the *vote* array
Source: Reprint from previous publication by author (5) ©2022 IEEE

Once the vehicle is positioned at a distance corresponding to d_safe, the flight direction with the highest number of votes is selected as the final decision. The utilization of the $vote$ algorithm serves to mitigate the potential misjudgment arising from a single frame's assessment. Singular frame-based perception and decision-making are inherently less reliable, as the environment may undergo abrupt changes due to factors such as moving objects or motion sensor blur. Consequently, the implementation of the cumulative voting algorithm, which aggregates judgments over a defined period, effectively mitigates decision-making errors and amplifies reliability.

5.2.3 Experimental Results

Before conducting field tests, a series of preliminary experiments are conducted within the Gazebo simulation environment. During these experiments, the configuration of sensors and ROS topics is adjusted to mirror that of the physical vehicle. Once the feasibility is established through these initial tests, the algorithm is subsequently evaluated in real-world environments.

5.2.3.1 Evaluation in the Gazebo Simulator

In the simulated environment, the point cloud is synthesized within the Gazebo simulator using a virtual depth camera. This camera's extrinsic parameters, including its position and orientation relative to the UAV, can be configured and fine-tuned to mimic the setup of the physical vehicle. To facilitate processing, the camera's intrinsic parameters are determined, and its RGB and depth images, along with the corresponding point cloud data, are made accessible as ROS topics. These topics can be subscribed to within the C++ framework to facilitate the detection and classification procedures.

In light of the classification and detection objectives inherent to point cloud processing, along with the examination of feasibility and algorithmic robustness for obstacle avoidance, a diverse array of objects is introduced into the simulation environment. As an illustrative example, the Gazebo simulator is configured with a dense distribution of trees serving as obstacles. The visual depiction in Figure 5.19 showcases the Ros topics that have been subscribed and rendered, facilitating the assessment of autonomous flight. In the lower-left portion, the real-time image feed is displayed, while the middle window reveals the outcomes of the detection process and the trajectory search.

The results indicate successful individual detection of tree trunks, represented by distinct green bounding boxes, while the collision detection volume of the UAV is visually represented by a yellow box. Upon identification of an obstacle situated in the current flight direction, the UAV proceeds with forward motion until a distance

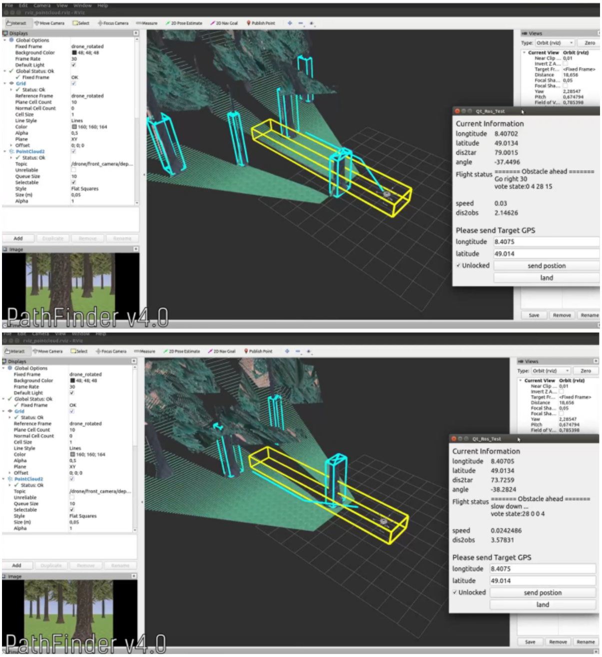

Global Options
Fixed Frame drone_rotated
Background Color 48; 48; 48
Frame Rate 30
Default Light ☑
Global Status: Ok
Fixed Frame OK
Grid ☑
Status: Ok
Reference Frame drone_rotated
Plane Cell Count 10
Normal Cell Count 0
Cell Size 1
Line Style Lines
Color 160; 160; 164
Alpha 0,5
Plane XY
Offset 0; 0; 0
PointCloud2 ☑
Status: Ok
Topic /drone/front_camera/dep...
Unreliable ☐
Queue Size 10
Selectable ☑
Style Flat Squares
Size (m) 0,05
Alpha 1

Type: Orbit (rviz) Zero
Current View Orbit (rviz)
Near Clip ... 0,01
Invert Z A... ☐
Target Fr... <Fixed Frame>
Distance 18,656
Focal Sha... 0,05
Focal Sha... ☐
Yaw 2,28547
Pitch 0,674794
Field of V... 0,785398

Current Information
longtitude 8.40702
latitude 49.0134
dis2tar 79.0015
angle -37.4496
Flight status ======= Obstacle ahead =======
Go right 30
vote state:0 4 28 15
speed 0.03
dis2obs 2.14626

Please send Target GPS
longtitude 8.4075
latitude 49.014
☑ Unlocked

Global Options
Fixed Frame drone_rotated
Background Color 48; 48; 48
Frame Rate 30
Default Light ☑
Global Status: Ok
Fixed Frame OK
Grid ☑
Status: Ok
Reference Frame drone_rotated
Plane Cell Count 10
Normal Cell Count 0
Cell Size 1
Line Style Lines
Color 160; 160; 164
Alpha 0,5
Plane XY
Offset 0; 0; 0
PointCloud2 ☑
Status: Ok
Topic /drone/front_camera/dep...
Unreliable ☐
Queue Size 10
Selectable ☑
Style Flat Squares
Size (m) 0,05
Alpha 1

Type: Orbit (rviz) Zero
Current View Orbit (rviz)
Near Clip ... 0,01
Invert Z A... ☐
Target Fr... <Fixed Frame>
Distance 18,656
Focal Sha... 0,05
Focal Sha... ☐
Yaw 2,28547
Pitch 0,674794
Field of V... 0,785398

Current Information
longtitude 8.40705
latitude 49.0134
dis2tar 73.7259
angle -38.2824
Flight status ======= Obstacle ahead =======
slow down ...
vote state:28 0 0 4
speed 0.0242486
dis2obs 3.57831

Please send Target GPS
longtitude 8.4075
latitude 49.014
☑ Unlocked

Figure 5.19: During the simulation tests, a lower-left viewer displays real-time imagery, allowing visual monitoring of the environment. In the middle viewer, detected and classified obstacles such as tree trunks are highlighted. The right viewer provides a graphical user interface (GUI) that enables real-time visualization and examination of the flight control system's status.
Source: Reprint from previous publication by author (5) ©2022 IEEE

of d_{safe} is attained. During this approaching phase, flight decisions are made based on the highest accumulated votes, illustrated as the green line. Concurrently, a Graphical User Interface (GUI) has been developed and is situated in the right corner of the visualization. This interface provides a comprehensive array of information, including the current and target GPS coordinates, the distance and angle to the target location, voting status, decision-making outcomes, and even the UAV's flight status. These data can be transmitted to a mobile device to facilitate visualization. This transmission is enabled by the connection between the on-board computer and the vehicle. The monitor of the on-board computer can be remotely displayed and the information can be transmitted to a ground station in real-time. A video showcasing this study has been published[1].

5.2.3.2 Field Test

For the field test, the DJI M600 Pro vehicle is equipped with an Intel Depth Camera D415, along with an on-board computer, the Manifold 2-C. The computer features an Intel Core i7-8550U CPU operating at 1.8GHz, complemented by 8 GB of DDR4 RAM. The real-time processing speed for the system is maintained at 10Hz.

In the field test environment, an L-shaped metal profile is strategically positioned as an obstacle. It is important to note that the point cloud generated by the depth camera can exhibit disturbances, such as noise stemming from motion blur of the camera or airborne dust particles caused by the UAV’s flight motion.

The results of the field test are depicted in Figure 5.20. A single obstacle, represented by a blue bounding box, is successfully detected. Additionally, the safety volume for the collision detector is depicted in yellow, while the white line illustrates the intended flight route. These visualizations are published as multi-geometry topics within the ROS environment, allowing them to be subscribed to and visualized using Rviz.

During the field test, the vehicle is initially manually positioned in front of the L-profile. Subsequently, the autonomous flight assistant is activated by toggling a specified flight mode. This authorization enables the on-board computer to assume control over flight operations and execute the algorithmic flight decisions, as elaborated in the subsequent section. As depicted in the results, when an obstacle is situated in front of the vehicle, the algorithm generates the decision represented by the white line indicating "go right in 30°". Upon execution, when

---

[1] A demonstration video of the Gazebo simulation and field tests conducted in this study can be accessed at the following link: `https://youtu.be/A0QP5m9vrW4`.

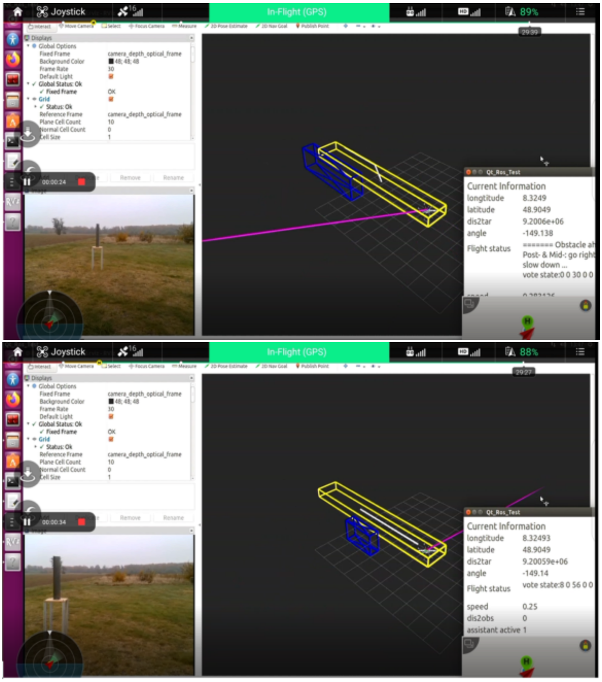

Displays
Global Options
Fixed Frame camera_depth_optical_frame
Background Color 48; 48; 48
Frame Rate 30
Global Status: Ok
Fixed Frame OK
Grid
Status: Ok
Reference Frame camera_depth_optical_frame
Plane Cell Count 10
Normal Cell Count 0
Cell Size 1

Current Information
longtitude 8.3249
latitude 48.9049
dis2tar 9.2006e+06
angle -149.138
Flight status ======= Obstacle ah
Post- & Mid-: go right
slow down ...
vote state:0 0 30 0 0

Current Information
longtitude 8.32493
latitude 48.9049
dis2tar 9.20059e+06
angle -149.14
Flight status vote state:8 0 56 0 0
speed 0.25
dis2obs 0
assistant active 1

Figure 5.20: Field-test results showcase the successful detection of a single L-shaped profile obstacle, highlighted by a dark blue bounding box. The accompanying yellow bounding box represents the safety volume utilized by the detector. A white line delineates the flight escape direction, indicating a course towards the right side, corresponding to the available free space around the obstacle.
Source: Reprint from previous publication by author (5) ©2022 IEEE

the obstacle is positioned on the left side, it is evident that the obstacle avoidance strategy has been successfully executed.

Furthermore, the algorithm's robustness is thoroughly evaluated within both simulation and real-world environments, encompassing various objects of true scale within Gazebo simulations. For instance, the presence of a transmission tower within the vehicle's field of view (FOV) is noteworthy. Despite the tower's substantial metallic sheet composition interspersed with gaps, it is categorized as a single, contiguous obstacle. During the field test, a similar scenario occurs with

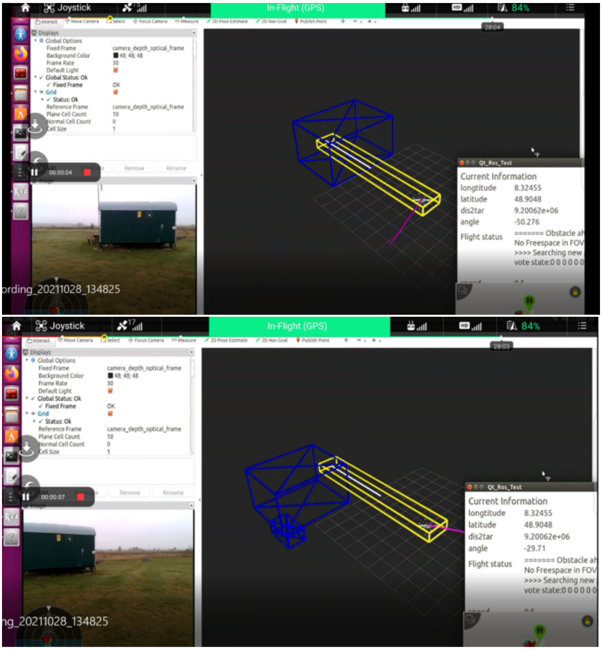

```
Displays
  Global Options
    Fixed Frame          camera_depth_optical_frame
    Background Color     48; 48; 48
    Frame Rate           30
    Default Light
  Global Status: Ok
    Fixed Frame          OK
  Grid
    Status: Ok
    Reference Frame      camera_depth_optical_frame
    Plane Cell Count     10
    Normal Cell Count    0
    Cell Size            1
```

```
Qt_Ros_Test
Current Information
longtitude      8.32455
latitude        48.9048
dis2tar         9.20062e+06
angle           -50.276
Flight status   ======= Obstacle ah
                No Freespace in FOV
                >>>> Searching new
                vote state:0 0 0 0 0 0
```

```
Qt_Ros_Test
Current Information
longtitude      8.32455
latitude        48.9048
dis2tar         9.20062e+06
angle           -29.71
Flight status   ======= Obstacle ah
                No Freespace in FOV
                >>>> Searching new
                vote state:0 0 0 0 0 0
```

Figure 5.21: In the field test scenario, a container serves as an obstacle, denoted by the blue bounding box in the visual representation. Owing to the substantial dimensions of the container, the existence of unoccupied free space within the FOV is conspicuously absent. In response to this challenge, the UAV system executes a yaw-rotation maneuver, strategically designed to ascertain the identification of a viable escape direction within the environment.
Source: Reprint from previous publication by author (5) ©2022 IEEE

the detection of a container, visualized through a blue bounding box in Figure 5.21. In this instance, due to the container's dimensions, a free space is not perceivable within the FOV. Consequently, the vehicle initiates a yaw-rotation decision, enabling the identification of a feasible escape direction. This choice is rational, given that executing lateral flight maneuvers in the absence of obstacle perception in that direction is inherently unwise.

5.3 UAV Flight Control Algorithm for Cantilever Installation on Transmission Towers via Depth Camera Utilization

In this section, we present a semi-autonomous flight control algorithm designed to assist pilots during the installation of cantilevers for weather stations onto transmission towers. The algorithm leverages depth camera capabilities to detect and estimate the pose of the mounting positions on the transmission tower, specifically targeting the mast's corner leg for installation purposes. This approach grants ground station operators the capability to activate or deactivate the autopilot process based on situational demands. Furthermore, a safety algorithm is introduced to ensure that the target remains within the FOV of the camera even as the vehicle undergoes movements and rotations during the approach. The proposed algorithm's efficacy is assessed through simulations in the Gazebo environment, where its performance aligns with the stipulated development requirements.

5.3.1 Related Work

Given the geometric properties of transmission towers and the mathematical attributes of mast corner legs, the employment of line features is a viable approach to represent mounting positions accurately. Prior to algorithm development, a comprehensive study of relevant methodologies is conducted to identify suitable algorithms for implementation.

The Hough transform, a universally applicable algorithm, was originally developed for extracting line features in image processing and remains prevalent today (80). Subsequently, the Fast Line Segment Detector (LSD) was introduced, utilizing the Local Gradient Method (81), and the Fast Line Detector (FLD) was devised, employing Canny edges and edge extension (82). In contrast to LSD, FLD offers enhanced speed and performance, particularly in man-made environments, demonstrating robustness against challenges such as occlusion, illumination variations, and diverse viewing poses. Despite extensive research in UAV control algorithms over time, only a limited number of autopilot algorithms have been developed with the specific objective of approaching transmission towers.

5.3.2 Image Processing

The primary objective of the algorithm is to extract and characterize the features of tower corner legs present in images captured by the depth camera mounted on the UAV. The input consists of aligned RGB images and point cloud data, which are used to perform line detection and subsequent image processing for the extraction of corner-leg line features. Subsequently, pose estimation is conducted to determine the relative position and orientation of the UAV in relation to the target installation corner leg.

Transmission towers represent unique detection targets that exhibit prominent line features within digital images. To address this, established line detection methodologies such as HoughLine, HoughLineP, LSD, and FLD are employed. Figure 5.22 displays the detection outcomes using images obtained from the Gazebo simulation environment. Notably, FLD showcases superior line detection performance accompanied by rapid detection speed. In contrast, the HoughLine algorithm exhibits limited sensitivity towards line segment lengths, rendering it suitable for continuous straight lines rather than fragmented line segments. Conversely, HoughLineP yields intermittent detection results, thereby compromising the continuity of line segments.

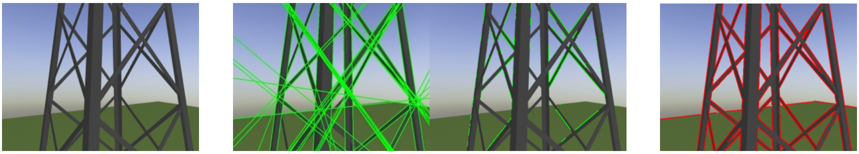

(a) Original **(b)** HoughLine **(c)** HoughLineP **(d)** FLD

Figure 5.22: Among the line detection algorithms considered, FLD stands out as the most proficient option due to its remarkable performance in terms of length sensitivity, continuity, and computational efficiency.
Source: Reprint from previous publication by author (4) ©2022 IEEE

While Fast Line Detector (FLD) demonstrates favorable line detection performance, intermittent line segments of the corner legs are observed. To address this, a strategy is employed to connect these segments by considering their gradient and pixel coordinates, provided their deviation adheres to a predefined threshold. However, it is essential to eliminate undesired features such as small horizontal and inclined brackets present on the mast. A mathematical approach is employed for discrimination based on gradient and length characteristics, effectively distinguishing these features from the corner legs.

(a) Line detection

(b) After gradient and length filtering

(c) Intersections at installation height

(d) Feature points for depth perception

Figure 5.23: Utilizing gradient and length filters facilitates the removal of unwanted segments, enabling the extraction of corner leg lines highlighted in yellow. The resulting intersection feature points play a crucial role in providing depth perception at the installation height. **Source**: Reprint from previous publication by author (4) ©2022 IEEE

Upon the completion of FLD line detection and the subsequent mending of fragmented lines, the outcomes are depicted in Figure 5.23 (a). The delineated yellow lines within Figure 5.23 (b) signify the identified characteristics of the mast's corner legs following the application of gradient and length filters. To facilitate the estimation of the mast's pose, it becomes imperative to acquire the depth information of the respective corner legs. For this purpose, a horizontal line is drawn across the image's midpoint, thereby minimizing the effects of camera distortion. The intersections, highlighted in green within Figure 5.23 (c), are poised for depth perception. The horizontally-aligned red points, portrayed in Figure 5.23 (d), correspond to the tower legs designated as A and B within the 3D model illustrated in Figure 5.25, as well as in the top view demonstration of Figure 5.26. Notably, each pixel's coordinate is indicative of a spatial point, a consequence of the RGB camera's prior calibration and alignment with the depth camera within the simulation environment.

5.3.3 Control Algorithms

The UAV is outfitted with a depth camera and an onboard computer, facilitating the detection and estimation of the pose of the target object. This processing takes place on the onboard computer, and subsequently, the relevant flight control commands are transmitted to the vehicle in real-time through a cable connection. The comprehensive control algorithm is partitioned into four distinct steps:

1. Pose initialization: This step involves determining the relative pose of the target mounting leg on the transmission tower in relation to the vehicle. This initialization is crucial for subsequent flight control actions aimed at reaching the proximity of the target, typically within one of the designated green areas depicted in Figure 5.24(a).

2. Rough adjustment: The objective of this phase is to guide the vehicle to a position near the target. Specifically, the vehicle is positioned at point O_1 and oriented towards the target leg, as demonstrated in Figure 5.24(b).

3. Approaching: In this step, the vehicle endeavors to approach the target along the delineated red flight trajectory O_1O_2, outlined in Figure 5.24(c). Additionally, robust target tracking mechanisms are implemented to mitigate flight deviations resulting from detection errors and wind disturbances.

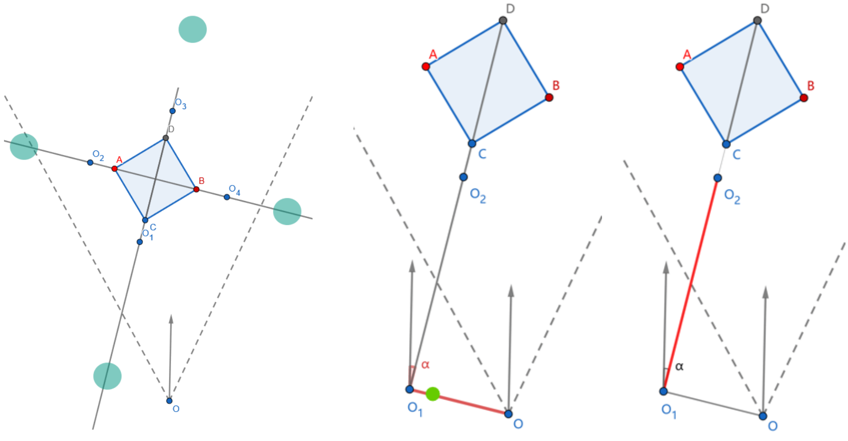

(a) Pose initialization **(b)** Rough adjustment **(c)** Approaching

Figure 5.24: Schematics of algorithm for different steps
Source: Reprint from previous publication by author (4) ©2022 IEEE

4. Fine adjustment: This stage entails precise pose estimation of the leg profile, leveraging available information about its dimensions and cross-sectional geometry. The acquired pose estimation facilitates accurate vehicle control, ensuring that the vehicle attains the intended pose.

5.3.3.1 Pose initialization

The precise calculation of the vehicle's pose concerning the mounting leg on the transmission tower holds paramount importance in devising suitable flight maneuvers. This evaluation is contingent upon their spatial geometric configuration, leading to the categorization of pose cases into three distinct scenarios:

1. In close proximity to the target corner leg.
2. Two corner legs are visible within the FOV of the camera.
3. Three corner legs situated within the field of view (FOV) of the camera.

Each of these cases is analyzed separately in the ensuing sections.

5.3.3.1.1 Pose Case 1 A simplified spatial model of the mast is presented in Figure 5.25. In this depiction, only the four legs are retained and visualized after undergoing image processing. The vehicle is situated in close proximity to target Leg C. Employing the camera coordinate system, with the origin O denoting the vehicle's current position, the camera's calibration and forward orientation are assumed(3). To streamline the pose calculation process, the top view of the legs' distribution is illustrated in Figure 5.26, where the solid perpendicular lines depict the x-z camera coordinates.

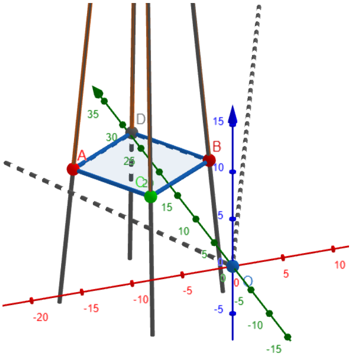

Figure 5.25: Pose case 1: UAV positioned in the vicinity of the target corner leg C
Source: Reprint from previous publication by author (4) ©2022 IEEE

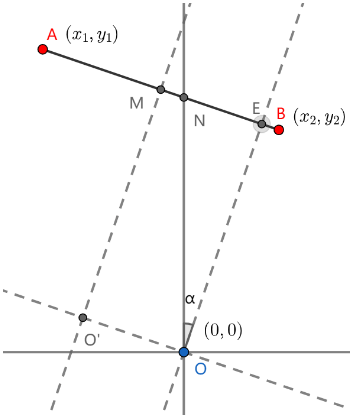

Figure 5.26: Top-view representation of the corner legs at the installation height.
Source: Reprint from previous publication by author (4) ©2022 IEEE

In the given scenario, the vehicle is positioned at point "O," which is in proximity to the target installation leg C, as depicted in Figure 5.25. Making use of the symmetric nature of the transmission tower, the leg C is projected onto the midpoint M of line segment AB within the camera's field of view. Furthermore, the dashed line originating from point $\boldsymbol{O'}$ illustrates the anticipated x-z plane of the camera coordinate system, corresponding to the UAV's strict orientation towards the target. Indeed, the yaw angle for flight control is denoted as α, while the vector $\overrightarrow{OO'}$ represents the direction and displacement of the UAV's motion.

In this context, the coordinates of the midpoint $\boldsymbol{M}$ on the x-z plane are given by:

$$M(\frac{x_1 + x_2}{2}, \frac{z_1 + z_2}{2}) \tag{5.15}$$

where (x_1, z_1) and (x_2, z_2) represent the spatial coordinates of mast legs A and B, respectively.

Mathematically, the line AB can be expressed as:

$$\frac{x - x_1}{x_2 - x_1} = \frac{z - z_1}{z_2 - z_1} \tag{5.16}$$

The perpendicular bisectors to segment AB are drawn from the origins $\boldsymbol{O}$ and $\boldsymbol{O'}$, intersecting at points M and E respectively. Since OO' is parallel to AB, the flight motion represented by vector $\boldsymbol{OO'}$ is equivalent to vector $\boldsymbol{EM}$, since the coordinates of point M are known and point E can be derived as the intersection of line AB described by equation 5.16 and line OE. Similarly, the equation to characterize line OE can be formulated as follows:

$$z = -\frac{z_2 - z_1}{x_2 - x_1}x \tag{5.17}$$

The intersection point E can be determined as follows:

$$x_E = \frac{\frac{z_1-z_2}{x_1-x_2} \cdot x_2 - z_2}{\frac{x_1-x_2}{z_1-z_2} + \frac{z_1-z_2}{x_1-x_2}} \tag{5.18}$$

$$= \frac{(z_1x_2 - z_2x_1)(z_1 - z_2)}{x_1^2 - 2x_1x_2 + x_2^2 + z_1^2 - 2z_1z_2 + z_2^2} \tag{5.19}$$

$$z_E = -\frac{x_2z_1 - x_1z_2 - 2x_2z_2}{x_1 - x_2 + \frac{(z_1-z_2)^2}{x_1-x_2}} \tag{5.20}$$

$$= -\frac{(x_2z_1 - x_1z_2 - 2x_2z_2)(x_1 - x_2)}{x_1^2 - 2x_2x_1 + x_2^2 + z_1^2 - 2z_1z_2 + z_2^2} \tag{5.21}$$

The direction and displacement of the vehicle can be denoted by the vector $\vec{OO'}$, which is derived as equal to the vector $\vec{EM}$:

$$x_{\vec{OO'}} = \frac{x_1 + x_2}{2} - \frac{-x_1z_2z_1 + x_1z_2^2 + x_2z_1^2 - z_2x_2z_1}{x_1^2 - 2x_1x_2 + x_2^2 + z_1^2 - 2z_1z_2 + z_2^2} \tag{5.22}$$

$$z_{\vec{OO'}} = \frac{z_1 + z_2}{2} + \frac{x_2z_1x_1 - x_2^2z_1 - x_1^2z_2 - x_2x_1z_2 + 2x_2^2z_2}{x_1^2 - 2x_2x_1 + x_2^2 + z_1^2 - 2z_1z_2 + z_2^2} \tag{5.23}$$

The rotational motion is characterized by the angle α:

$$\alpha = \angle NOE = \arctan(\frac{x_E}{z_E}) = \arctan(-\frac{\frac{\frac{z_1-z_2}{x_1-x_2} \cdot x_2 - z_2}{\frac{x_1-x_2}{z_1-z_2} + \frac{z_1-z_2}{x_1-x_2}}}{\frac{x_2z_1 - x_1z_2 - 2x_2z_2}{x_1 - x_2 + \frac{(z_1-z_2)^2}{x_1-x_2}}}) \tag{5.24}$$

which can be simplified to:

$$\alpha = \arctan(-\frac{-z_2x_1z_1 + z_2^2x_1 + z_1^2x_2 - z_2z_1x_2}{2z_2x_2^2 - z_2x_1x_2 + x_1z_1x_2 - z_1x_2^2 - z_2x_1^2}) \tag{5.25}$$

Considering the motion vector $\vec{OO'}$ and the yaw rotation angle $\angle NOE$, the real-time control commands are computed on the on-board computer and subsequently transmitted to the vehicle for execution. However, it is assumed that the UAV is already situated in the vicinity of the target location. The algorithm must be designed to address various scenarios, including situations where the target is lost during control. The ensuing section outlines the control algorithms in detail.

5.3.3.1.2 Pose Case 2

The UAV will initially rotate until the transmission tower is within its field of view (FOV). A distinctive configuration is depicted in Figure 5.27, where solely two corner legs are observable within the camera's FOV. Simultaneously, the lateral leg C or B is designated as the target mounting position. Notably, the yaw angle for the UAV's orientation, shifting from the current position $\boldsymbol{O}$ to the directed position at $\boldsymbol{O_1}$, approximates $\pm 45°$.

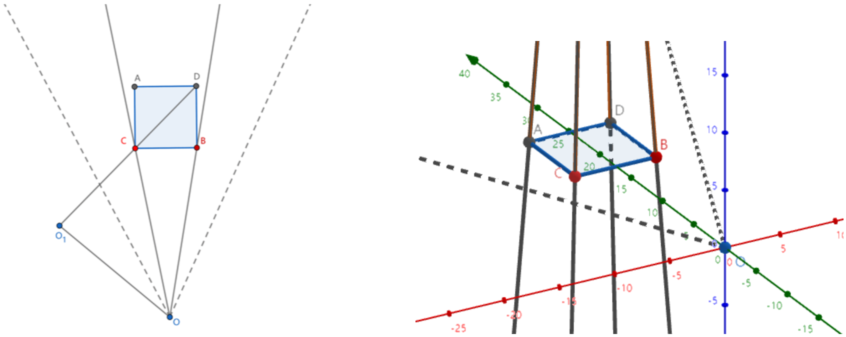

(a) Top view of Case 2 **(b)** 3D view of Case 1

Figure 5.27: Pose case 2: the detection of two mast legs within the field of view (FOV) of the UAV. In order to approach the target leg C or B, the requisite yaw angle adjustment approximates $\pm 45°$.
Source: Reprint from previous publication by author (4) ©2022 IEEE

5.3.3.1.3 Pose Case 3

A scenario is exemplified in Figure 5.28, where either side-lying leg A or B is designated as the target. This scenario introduces a unique challenge to the control algorithm, as it involves a yaw rotation angle approximation of $\pm 90^\circ$, requiring a specialized approach.

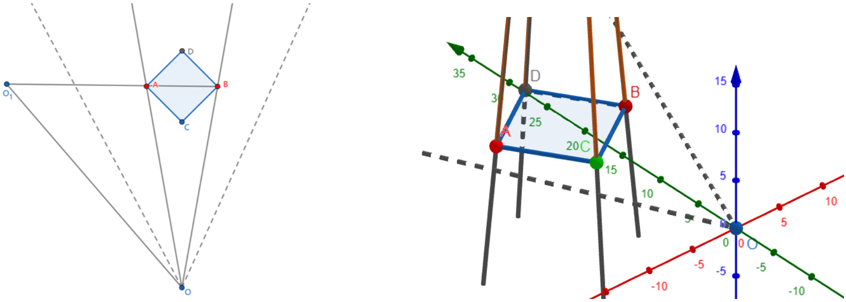

(a) Top view of Case 2

(b) 3D view of Case 2

Figure 5.28: Case 2 pertains to the detection of three mast legs within the UAV's field of view (FOV). When aiming to reach a laterally situated target leg A or B, the necessary yaw angle adjustment becomes approximately $\pm 90^\circ$.
Source: Reprint from previous publication by author (4) ©2022 IEEE

The flight control algorithm designed to address the specific scenarios is outlined in Algorithm 1. For the purpose of installation, a chosen corner leg serves as a reference, with its orientation indicated by the input angle θ_0, which may be represented in forms such as compass rose or azimuth angle. Furthermore, the orientation of the UAV denoted as θ can be acquired through the subscription of the ROS topic related to the integrated compass sensor on the UAV. This sensor is calibrated by the manufacturer in the context of the geographic coordinate system.

By assessing the input and the prevailing heading direction of the vehicle, the deviation $\Delta\theta$ yields the yaw command, while D symbolizes the distance to the nearest tower leg. The progression towards the target is then outlined within the pseudocode. Notably, the algorithm incorporates parameters for the motion speed along the x-, y-, and z-axes, as well as the rotational speed around the yaw axis. The execution time is also considered in the control algorithm.

Algorithm 1 Position Initialization
Source: Reprint from previous publication by author (4) ©2022 IEEE

```
Input: $\theta_0$: Orientation of the chosen leg on transmission tower
Output: Flight Control Command
$\Delta\theta = \theta - \theta_0$
while $\Delta\theta < -45°$ or $\Delta\theta > 45°$ do
    if Case = 2 then
        Command = Yaw $45°$ + Move $\frac{\sqrt{2}}{2}D$
        Execute Command...
    else {Case = 3}
        Command = Yaw $45°$ + Move $2D$ + Yaw $45°$
        Execute Command...
    end if
    Update $\theta$, based on ros topic compass sensor
    Update Case, based on position of mast nearest leg
    Update $D$, based on distance to nearest mast leg
    $\Delta\theta = \theta - \theta_0$
end while
Enter next step...
```

5.3.3.2 Rough adjustment

During the course of autonomous flight control, Algorithm 1 functions as a rough adjustment mechanism, enabling the vehicle to approximate the proximity of the installation leg. However, a challenge arises due to the inherent movement and rotation of the vehicle: the potential loss of the target. This occurs when the transmission tower or installation leg exits the FOV. Consequently, the continuity of detection is disrupted, leading to orientation ambiguity for pilot control. Such circumstances could compromise both the safety of manual control and the discernment of the surroundings, especially when the corner legs of the transmission tower exhibit a pronounced homogeneity.

Hence, an algorithm depicted in Flowchart 5.29 is devised to mitigate this challenge. The UAV's control actions are carried out either as a movement or yaw rotation, but these actions are not executed simultaneously. To that end, two

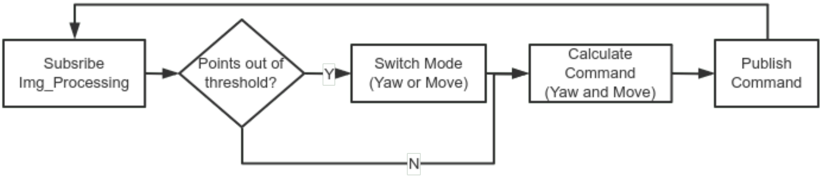

Figure 5.29: Implementing a rough adjustment strategy is crucial to address the challenge of target loss.
Source: Reprint from previous publication by author (4) ©2022 IEEE

motion patterns are distinguished: the yaw-first pattern and the move-first pattern, where the latter is set as the initial mode. To avert target loss in the FOV, vertical pixel thresholds are defined on the image plane, both on the left and right sides. Whenever any feature points fall outside of this pixel range, the mode switches to the yaw-first pattern until the feature points are back within the threshold range.

5.3.3.3 Approaching

Following the rough adjustment, the vehicle is positioned in proximity to the installation leg and is correctly oriented toward the target. Subsequently, the approach phase is initiated, involving flight control along the designated red route displayed in Figure 5.24(c). This flight path is selected based on the assumption that tower leg C in Figure 5.30 serves as the target and is being actively tracked. However, due to factors such as detection inaccuracies, discrepancies between expected and executed flight commands, and disturbances in the airflow, the vehicle might deviate from the intended flight path. Consequently, a similar challenge of target loss is encountered during this phase as well.

To mitigate the issue of target loss, a safety-oriented algorithm has been devised. This algorithm is designed to address situations in which feature points of the tower are detected at considerable distances or the designated corner leg is detected at close proximity, leading to their positioning outside the specified pixel range on the image plane. When such circumstances occur, the safety-related algorithm

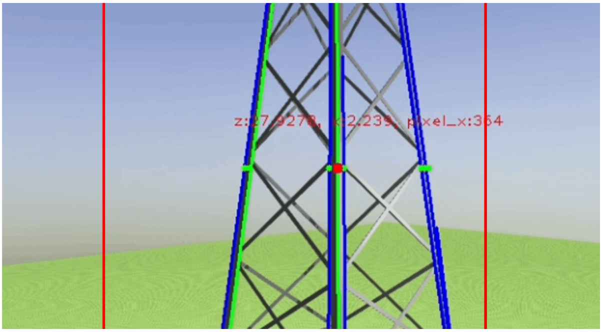

Figure 5.30: The establishment of thresholds on the image plane is intended to ensure that feature points of the target remain within predefined pixel boundaries. This is achieved by dynamically adjusting the yaw angle of the vehicle during its operation.
Source: Reprint from previous publication by author (4) ©2022 IEEE

is triggered. It involves lateral position adjustments to regain target tracking, along with a halt in the ongoing approach maneuver to accommodate the vehicle's pose adjustments. Pseudo-code 2 succinctly outlines the steps of this algorithm, with D_0 denoting the predetermined distance to the target, acting as a collision-avoidance threshold.

5.3.3.4 Fine adjustment

At the commencement of the "PrognoNetz" project, an exploration of transmission towers positioned along two high voltage lines was undertaken. The primary objective was to gather an understanding of the surrounding geographical conditions, as well as to familiarize with the varied cross-sectional shapes and dimensions of the tower legs. Within Germany, the commonly employed mast leg profiles encompass L-profiles and X-profiles. For the purposes of this study, the pose of the L-profile configuration is examined as an illustrative example. Visual representations of the structure from both the frontal and top perspectives are depicted in Figures 5.31 and 5.32.

Algorithm 2 Approaching.
Source: Reprint from previous publication by author (4) ©2022 IEEE

```
Input: $(x_C, z_C)$: the coordinates of target $C$;
Input: Required Distance $D_0$
Output: Command Execution
Initialization: Safety := True
while Distance $> D_0$ do
    if Safety then
        $Speed = 0.1 \times Distance$
        Execute approaching command
    else {Safety = False}
        Move laterally
        if Point C is in the center of image then
            Safety = True
        end if
    end if
    Detect point C
    if Point C out of threshold then
        Safety = False
    end if
    Update Distance
end while
Enter next step...
```

The fine adjustment phase is dedicated to pose estimation of the profile, enabling precise positioning of the vehicle at the designated distance and orientation from the target. Upon the UAV's proximity to the mounting leg becoming less than 3 meters, the edges of the profile can be detected. This is visually demonstrated by the delineation of the green and blue edges in Figure 5.31, while the top view in Figure 5.32 showcases the feature points C, C_1, and C_2. Given the known dimensions of the profile, flight control commands encompassing translation and yaw motion can be directly derived from equations 5.22, 5.23, and 5.25. It is worth noting that the execution of flight control involves setting the appropriate speed. The calculated relative pose is transmitted to the vehicle as input and executed through the application of a proportional controller. This choice is motivated by its capacity to enhance the resilience of the flight control process in the presence of measurement errors or deviations.

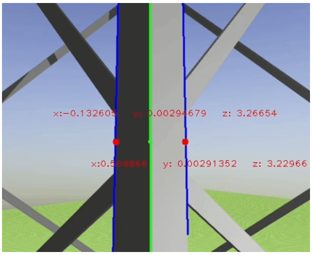

Figure 5.31: Detection of the tower leg profile edges at close proximity.
Source: Reprint from previous publication by author (4) ©2022 IEEE

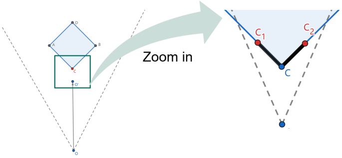

Figure 5.32: Top view of profile edges as points C, C_1, C_2, serve as pose estimation.
Source: Reprint from previous publication by author (4) ©2022 IEEE

5.3.4 Implementation and results

The implemented algorithm has undergone testing and validation within the Gazebo robotic simulation environment. This environment is equipped with realistic components such as a grassy terrain, appropriate lighting conditions, and true-to-scale high voltage infrastructure. The experimental setup utilized an Intel Core i7-8550U processor, achieving a processing speed of 25 frames per second for both image detection and flight command execution. To ensure a smooth flight control experience, a rate of 10 Hz was chosen for the algorithm's execution within the ROS framework. Furthermore, the depth perception capability was configured to 50 meters, resulting in dependable detection performance. It is worth noting that for practical deployment, calibrated Lidar and camera systems can be employed to achieve similar levels of performance.

The outcomes of the image processing within the simulation environment are visually displayed in Figure 5.33. The successful extraction and detection of the line features representing the mast corner legs are evident. Specifically, the side-lying corner legs are indicated as red points in Figure 5.33(a), playing a pivotal role in the phases of pose initialization and rough adjustment. During the approaching stage, the target leg is consistently tracked and identified as a red point in Figure 5.33(b) and (c). Additionally, Figure 5.33(d) illustrates the extraction of three edges delineating the mounting L-profile, a crucial step in achieving accurate pose estimation.

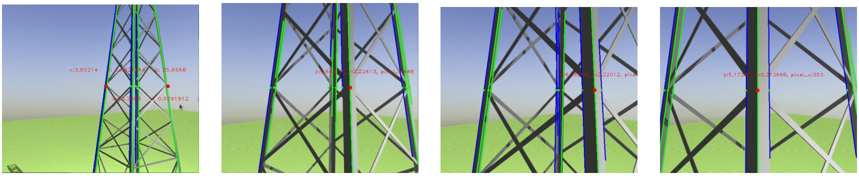

(a) Pose Initialization and rough adjustment **(b)** Approaching **(c)** Approaching **(d)** Fine Adjustment

Figure 5.33: Image processing is employed to detect the designated target, which could either be the transmission tower itself or its corner legs, at various stages of the control process. **Source**: Reprint from previous publication by author (4) ©2022 IEEE

A QT-based graphical user interface (GUI) has been developed and is depicted in the lower left section of Figure 5.34. This interface features four clickable buttons, designed to facilitate the input of the installation position onto the predetermined corner leg. Upon pressing the button corresponding to the left side-lying target leg, the relative pose is initialized. Notably, this scenario aligns with the special case of flight control illustrated in Figure 5.27. Following the execution of the designated rough adjustment control algorithm, the vehicle achieves proximity to the designated area while aligning itself with the target leg, as demonstrated in Figure 5.35. Notably, at this juncture, the nearest mast leg within the camera's field of view becomes the primary focus.

The vehicle effectively approached the designated target, with the continuous activation and successful execution of the algorithm to maintain the target within the FOV. As the vehicle drew closer to the target at a close distance, the fine adjustment algorithm engaged to precisely estimate the pose of the L-profile.

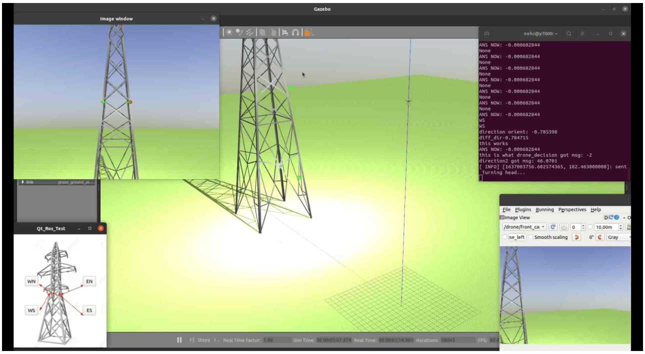

```
ANS NOW: -0.000682844
None
ANS NOW: -0.000682844
None
ANS NOW: -0.000682844
None
ANS NOW: -0.000682844
None
ANS NOW: -0.000682844
None
ANS NOW: -0.000682844
None
ANS NOW: -0.000682844
WS
WS
direction orient: -0.785398
diff_dir-0.784715
this works
ANS NOW: -0.000682844
this is what drone_decision got msg: -2
direction2 got msg: 46.0701
[ INFO] [1637003756.602574365, 182.463000000]: sent
 Turning head...
```

Figure 5.34: Pose Initialization: The choice of the mounting leg is initiated by pressing the button positioned in the lower-left corner of the GUI interface.
Source: Reprint from previous publication by author (4) ©2022 IEEE

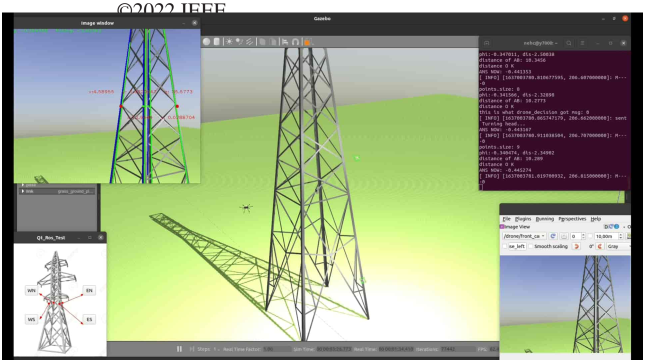

```
phi:-0.347011, dis-2.50038
distance of AB: 10.3456
distance O K
ANS NOW: -0.441353
[ INFO] [1637003780.810677595, 206.607000000]: M---
-0
points.size: 8
phi:-0.341566, dis-2.32898
distance of AB: 10.2773
distance O K
this is what drone_decision got msg: 0
[ INFO] [1637003780.865747179, 206.662000000]: sent
 Turning head...
ANS NOW: -0.443167
[ INFO] [1637003780.911038504, 206.707000000]: M---
-0
points.size: 9
phi:-0.340474, dis-2.34902
distance of AB: 10.289
distance O K
ANS NOW: -0.445274
[ INFO] [1637003781.019700932, 206.815000000]: M---
-0
```

Figure 5.35: Rough Adjustment: The UAV effectively approached the vicinity of the designated mounting corner leg, simultaneously aligning its orientation with the intended target.
Source: Reprint from previous publication by author (4) ©2022 IEEE

This adjustment ensured that the UAV remained at the requisite distance for the installation or replacement of sensors. The pose calculation was predicated on the spatial relationship of the three detected lines, as illustrated in Figure 5.37. During the simulation, the UAV demonstrated robust performance even under conditions of detection inaccuracies, or control deviations.

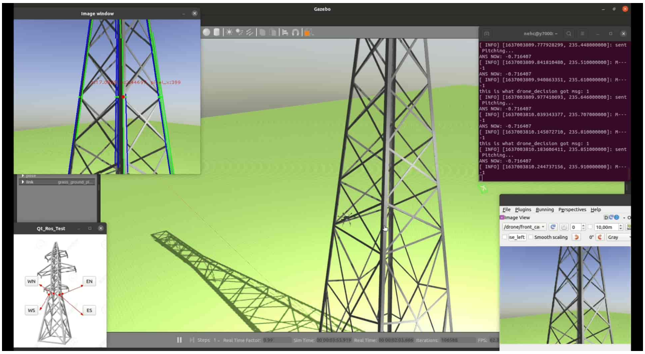

```
[ INFO] [1637003809.777928299, 235.448000000]: sent
 Pitching...
ANS NOW: -0.716407
[ INFO] [1637003809.841810480, 235.510000000]: M---
-1
ANS NOW: -0.716407
[ INFO] [1637003809.940863351, 235.610000000]: M---
-1
this is what drone_decision got msg: 1
[ INFO] [1637003809.977410693, 235.646000000]: sent
 Pitching...
ANS NOW: -0.716407
[ INFO] [1637003810.039343377, 235.707000000]: M---
-1
ANS NOW: -0.716407
[ INFO] [1637003810.145072710, 235.810000000]: M---
-1
this is what drone_decision got msg: 1
[ INFO] [1637003810.183606411, 235.851000000]: sent
 Pitching...
ANS NOW: -0.716407
[ INFO] [1637003810.244737156, 235.910000000]: M---
-1
```

Figure 5.36: Approaching: The red dot, signifying the target, remains within the FOV of the camera.
Source: Reprint from previous publication by author (4) ©2022 IEEE

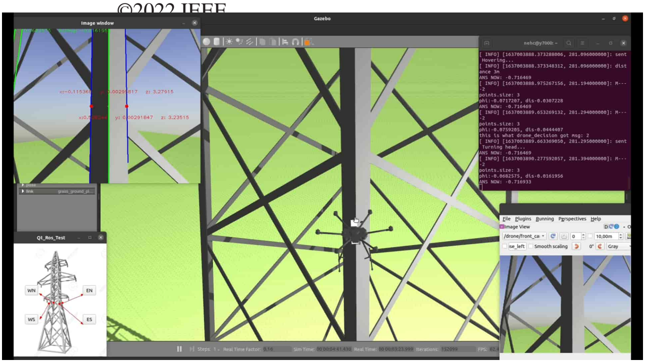

```
[ INFO] [1637003888.373288006, 281.096000000]: sent
 Hovering...
[ INFO] [1637003888.373348312, 281.096000000]: dist
ance 3m
ANS NOW: -0.716469
[ INFO] [1637003888.975267156, 281.194000000]: M---
-2
points.size: 3
phi:-0.0717207, dis-0.0307228
ANS NOW: -0.716469
[ INFO] [1637003889.653269132, 281.294000000]: M---
-2
points.size: 3
phi:-0.0759205, dis-0.0444407
this is what drone_decision got msg: 2
[ INFO] [1637003889.663369050, 281.295000000]: sent
 Turning head...
ANS NOW: -0.716469
[ INFO] [1637003890.277592057, 281.394000000]: M---
-2
points.size: 3
phi:-0.0682575, dis-0.0161956
ANS NOW: -0.716933
```

Figure 5.37: Fine adjustment: The mast leg profile's pose is determined based on the relationship between three detected lines.
Source: Reprint from previous publication by author (4) ©2022 IEEE

Despite the commendable performance of the algorithm within the simulation, its validation and potential optimization necessitate field tests. To this end, the selection of an appropriate depth sensor becomes imperative, one that can achieve the aforementioned depth perception capabilities of at least 50 meters, if not more. Among the recommended options are the Lidar and monocular camera. Prior to conducting the field experiments, meticulous calibration of these sensors is essential. This calibration process establishes a vital link between the pixel coordinates on the image plane and the corresponding points in the three-dimensional coordinate space.

5.4 Detection and UAV Flight Planning for Weather Station Installation on Cantilever

As discussed in the preceding section, the initial step involves the installation of the cantilever onto the transmission tower. This installation is crucial to mitigate the impact of turbulence generated by the tower's structure on wind measurements. The cantilever is equipped with a sensor holder for this purpose. It is worth noting that GPS-based positioning offers vertical and horizontal hovering accuracy within the range of ±0.5 meters and ±1.5 meters, respectively. This level of accuracy presents challenges for manual control when the vehicle needs to hover precisely in close proximity to the sensor-holder position, especially in adverse weather conditions where collisions may occur. Therefore, a semi-autonomous flight control algorithm has been developed. This algorithm enables continuous tracking and approach to the sensor-holder position, along with the capability to recover the target within the FOV of the observation system.

5.4.1 Related Work

Object detection plays an essential role in various robotics applications, such as autonomous driving and robotic arm grasping. This research field can be primarily categorized into two main branches: 2D object detection, which operates on image data, and 3D object detection, which works with point cloud data.

In the realm of 2D object detection, there exist robust scale- and rotation-invariant methods such as the Scale-Invariant Feature Transform (SIFT) (83), Speeded-Up Robust Features (SURF) (84), and Oriented FAST and Rotated BRIEF (ORB)

(85). These methods excel in providing distinctive descriptors for object recognition. It's worth noting that both SIFT and SURF algorithms are employed to extract descriptors from a source image, assuming a single perspective of the object. Comparatively, SURF has proven to be more efficient for real-time applications, while SIFT exhibits higher accuracy in pattern recognition (86). In the contemporary landscape of object detection, neural network-based methods such as the Single Shot Multibox Detector (SSD) (87), You Only Look Once (YOLO) (88), and Faster R-CNN (66) have gained popularity. These deep learning approaches have demonstrated remarkable performance in object detection tasks.

In the domain of 3D object detection, the utilization of end-to-end learnable architectures has become prominent. These architectures are employed for both 3D object detection and ground estimation, aiming to enhance representation by amalgamating information from diverse levels (89). For instance, the VoteNet, which relies on a synergy between deep point set networks and Hough voting, has been applied with significant success, achieving state-of-the-art 3D object detection results (90). Furthermore, a noteworthy contribution in 3D object detection is the Point-GNN, a graph neural network tailored for object shape prediction. This network employs an auto-registration mechanism to reduce translation variance and employs advanced detection techniques like box merging and scoring, further enhancing its object detection capabilities (91).

The current landscape of object detection research prominently features the utilization of neural network methods for both 2D and 3D object detection tasks. However, one of the key challenges in this domain lies in the acquisition of diverse and labeled datasets, a process that can be labor-intensive but essential for achieving high detection accuracy. Meanwhile, the development of installation procedures and semi-autonomous assistance systems is still in progress and not yet suitable for widespread commercial applications. This situation presents a significant obstacle when it comes to obtaining datasets in the specific context of high-voltage facilities. In response to these challenges, an alternative approach has been proposed. This approach is rooted in texture-based algorithms designed to guide and enhance the hovering stability of UAVs during installation and maintenance operations.

5.4.2 Algorithm

As previously elucidated, traditional neural network approaches are not employed for the detection task in this context. Instead, a texture-based algorithm is introduced, utilizing point cloud data as input and leveraging color features for detection. Figure 5.38 illustrates the algorithm, which is primarily divided into two main components: the activation of autonomous flight and the flight control mechanisms for approaching the sensor-holder position.

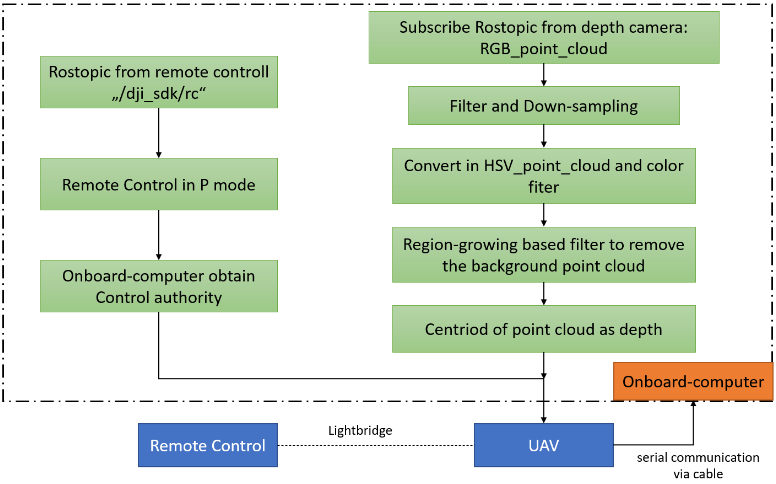

Figure 5.38: Flow chart: explanation of the algorithm

5.4.2.1 Activation of Autonomous Flight

As previously mentioned, the ground station pilot retains the authority to activate or deactivate autonomous flight as necessary. This design plays a pivotal role in ensuring safety. In cases where the algorithm does not perform as expected or environmental conditions change suddenly due to the presence of moving objects in the airspace, the pilot can manually intervene to regulate autonomous flight control.

The 6-channel flight control commands from the remote controller are transmitted to the vehicle via the "Lightbridge" and are published and subscribed to using the ROS topic $''/dji\_sdk/rc''$ on the onboard computer. This communication occurs through a UART interface. The parameter Axes[4] on $''/dji\_sdk/rc''$ indicates the Flight Mode status, which includes P/A/F modes. The switch associated with this parameter is utilized to activate autonomous flight when the pilot switches to the "P" mode.

During experimentation, it was observed that the onboard computer takes approximately 3 seconds to obtain control authority. Consequently, employing an iterative check and obtaining control authority in real time is not a viable approach. This is because the vehicle receives flight commands every 3 seconds, and adopting an iterative approach in this scenario would compromise safety and consistency.

To overcome the issue of the long duration required to obtain control permission of the onboard computer, the following algorithm (Algorithm 3) has been developed. This algorithm ensures a swift and consistent acquisition of control authority by detecting changes in flight mode. Specifically, control authority is requested when the mode switches from a Non-P mode to Mode P. Control authority will then be retained until the pilot switches the Flight Mode to A or F mode. This algorithm is implemented in all control algorithms to enable semi-autonomous flight control.

Algorithm 3 Activate the autonomous flight by using remote controller

```
Input: rostopic /dji_sdk/rc
Output: Onboard computer obtain or release flight control authority
Initialise and configuration the ros environment
Wait to subscribe the rostopic "/dji_sdk/rc"
if Flight Mode at time $t_{n-1} \neq$ Mode P, at time $t_n$ = Mode P then
    Onboard Computer obtain flight control authority
    Execute Flight Commands come from the onboard computer
else
    Onboard Computer release flight control authority
    Pilot at ground station obtain control authority
end if
Update /dji_sdk/rc
```

5.4.2.2 Point Cloud-Based Detection

In contemporary object detection, neural networks have gained popularity. As previously noted, acquiring a suitable dataset for training during the development phase is a challenging task. Furthermore, due to issues related to detection accuracy and the presence of similar geometric shapes in the background, there is a risk of incorrect and inconsistent detection, potentially leading to misguided flight control. Consequently, this work opts for the adoption of the traditional color-texture-based detection method. This method offers the advantage of swift and straightforward adjustment and reconfiguration, enhancing convenience in practical implementation.

In the typical workflow, once the depth camera node within the ROS package is initiated, various stream parameters such as resolution, frame rates, rostopic types, etc., can be optionally selected and configured within the "launch file." Subsequently, when subscribing to the RGB point cloud on the onboard computer, a need arises to handle the substantial volume of points, which can often reach six-digit numbers. To address this issue, a two-step process is applied to manage computational costs. Initially, the point cloud is filtered to retain only those points falling within a user-defined spatial range of interest. Subsequently, a uniform down-sampling operation is performed to preserve the color properties while reducing the overall data volume.

Following this, the RGB point cloud undergoes conversion to the HSV color space and subsequent filtering to retain points within the user-defined HSV range. This approach proves efficient and straightforward, particularly by modifying the H value to select the color, thus obviating the need to adjust the R, G, and B channels simultaneously. In this context, the cantilever is assumed to be constructed from metal material, while the sensor-holder is coated in white for environmental compatibility and adaptability. However, it's crucial to note that environmental interference and noise can only be partially filtered out through this method. As illustrated in Figure 5.39, the white background may persist. During field tests, this phenomenon becomes more prominent, especially in sunny weather conditions with strong illumination, where numerous bright spots on the background surface are also detected.

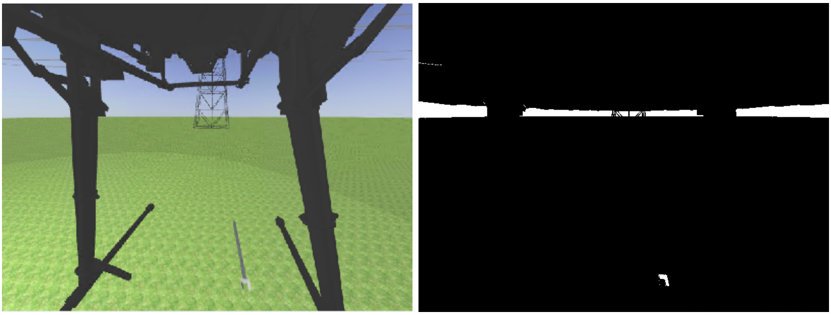

Figure 5.39: Despite the application of HSV (color) filtering, some disturbances originating from the surrounding environment remain visible in the images. On the right side of the images below, you can see the white regions that represent the areas of interest after filtering. These regions encompass not only the sensor-holder but also portions of the background.

To further extract the sensor-holder position, additional processing steps are necessary. Utilizing region growing segmentation, the entire point cloud is classified into distinct clusters. This step proves crucial in preventing noise or unwanted objects from being mistaken as the target for vehicle flight control. Given the gradual approach to the target, the number of target point cloud data points increases. Consequently, only the cluster exhibiting the maximum and continuously increasing number of point cloud data points is considered the target.

As previously introduced in prior work, the downward-facing depth camera has already undergone calibration in the UAV coordinate system (3). Consequently, the centroid of the point cloud data (in camera coordinates) has been successfully transformed into the UAV coordinate system. This transformed data is subsequently published as a flight control command and executed on the vehicle, provided that the remote controller is switched to P mode and the onboard computer has obtained control permission.

5.4.2.3 Flight Control

The flight control command obtained after processing the point cloud data corresponds to the spatial distance to the target. When executing this command on the vehicle, the speed of movement in the x, y, and z axes, as well as the rotation speed around the yaw axis, are set accordingly. In this control scheme, only a proportional controller is utilized to convert the spatial distance into speed. This approach enhances the algorithm's robustness against errors arising from object detection, depth measurement, and wind disturbances.

However, during the tests in both simulation and field environments, an issue arose during the autonomous approaching process. This issue was attributed to variations in speed along the x, y, and z axes, coupled with the influence of wind disturbances. As a result, the target would sometimes be lost from the FOV, leading to erratic flight control behavior. An illustrative example highlighting this issue is presented in Figure 5.40. It becomes evident that the relatively larger distance along the y-axis compared to the distance along the x-axis results in a correspondingly higher downward speed. This discrepancy in speed contributes to the loss of the target within the FOV. To mitigate this noticeable problem, it is proposed that when obtaining and converting the spatial distance to the target in the UAV-coordinate system, the x-distance should be made proportional to the z-distance. This adjustment ensures that the target remains consistently within the FOV, taking into account the inclination angle of the camera in the x-z plane as provided by previous calibration work (3).

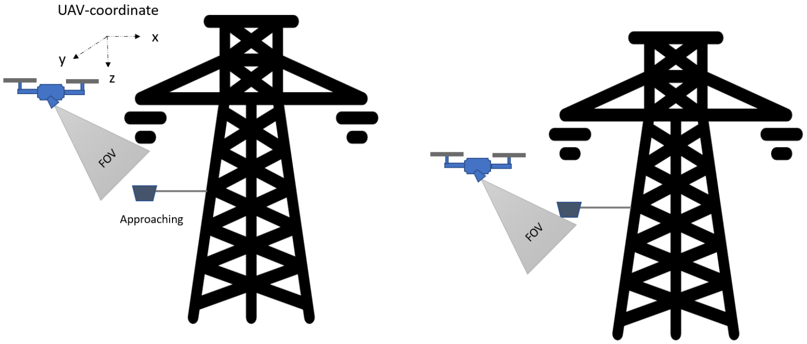

Figure 5.40: A challenge in flight control arises when the distance along the y-axis is relatively larger than the distance along the x-axis, resulting in a higher downward speed and, consequently, the loss of the target within the FOV.

Additionally, the relative orientation plays a crucial role in the installation and maintenance of the weather station since the autonomous flight control does not account for yaw rotation. To address this, the control command available in the Ros-topic ”$/dji_sdk/rc$” of the remote controller is utilized even during autonomous flight. Specifically, the parameter associated with yaw rotation can be executed, allowing the pilot to control the vehicle’s yaw rotation from the ground station. Moreover, for collision prevention and maintaining a safe distance from the target position, such as the sensor-holder, the algorithm empowers the pilot to adjust this distance using the remote control, as illustrated in Figure 5.41.

5.4.3 Filed Test

In Figure 5.41, the depth estimation to the white-coated prism-shaped sensor-holder is depicted alongside the required safe distance. The "Assistant active" indicator signifies whether autonomous operation is initiated by the pilot; in the images, a value of 1 indicates that the remote controller is in P mode. "Dist X" represents the distance to the mounting position for the weather station along the X-axis in the drone's coordinate system, while "Desired X" signifies the desired distance. This desired distance can be adjusted via the remote controller, allowing the pilot to increase or decrease the distance as needed. This control capability also extends to the Z-axis.

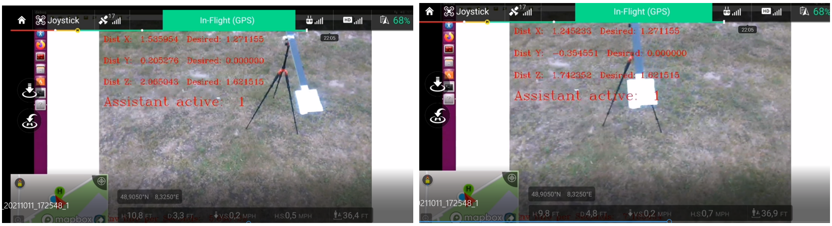

```
Dist X:  1.535954  Desired: 1.271155
Dist Y:  0.205276  Desired: 0.000000
Dist Z:  2.065043  Desired: 1.621515
Assistant active:  1
```

```
Dist X:  1.245233  Desired: 1.271155
Dist Y:  -0.354551  Desired: 0.000000
Dist Z:  1.742352  Desired: 1.621515
Assistant active:  1
```

Figure 5.41: The 3D depth estimation to the target position is displayed, and the required distance can be adjusted by the pilot.

The approaching process during the field tests is depicted in Figure 5.42. As observed, the vehicle can approach the mounting position for the sensor station in a targeted and stable manner, even under wind disturbance conditions. Notably, the hovering accuracy has been significantly enhanced. It's worth mentioning that wind speeds during the tests reached approximately 13 km/h, and the algorithm demonstrated excellent performance.

Figure 5.42: The vehicle approached the sensor-holder steadily and consistently during the autonomous operation.

6 Conclusion and Future Work

This dissertation has introduced a novel and systematic approach to the installation and maintenance of weather stations on transmission towers using unmanned aerial vehicles (UAVs). The primary goal of this approach is to provide localized weather data along transmission lines, facilitating the development of a weather-dependent monitoring system and transmission capacity forecasting system. This system plays a crucial role in mitigating or preventing grid congestion, aiding transmission system operators in effectively managing and integrating decentralized energy production from renewable sources into the electrical grid.

In the second chapter, the mechanical design for attaching weather stations is presented. Section 2.1 introduces existing traditional methods for collecting weather data at the height of transmission lines. Subsequently, Section 2.2 introduces the attachment concept for installing and maintaining weather stations on the corner legs of transmission towers. Furthermore, in consideration of the various dimensions and cross-section profiles of installation locations (i.e., mast corner legs), Section 2.3 presents the development of a self-adjustment function for sensor equipment, such as the cantilever. Section 2.4 illustrates a method for exploring lightweight construction options for the cantilever.

Regarding the application scenario and future work, it is imperative that the self-adjusted sensor equipment be constructed with lightweight materials and undergo wind tunnel testing. This testing will utilize local wind measurement data obtained from PrognoNetz or other open data sources to simulate fluid dynamic properties in the vicinity of transmission masts. This evaluation will help optimize the geometric shape and the overall life cycle of the equipment.

In the third chapter, we delve into the feasibility analysis of various gripper concepts designed for the carrying, releasing, and retrieving of sensor equipment. In Section 3.1, we introduce three common magnet-based gripper systems. We evaluate their feasibility and shortcomings based on labor and field tests. We initially tested the attachment of sensor equipment using a purely magnetic approach, which proved successful.

Building upon this, we have developed an improved and lighter servomotor-based gripper concept. This concept has been tested under laboratory conditions and has shown promise. Additionally, we propose future testing of the functionality of this concept, along with the complete attachment mechanism for sensor equipment, in a real-world field environment.

In the fourth chapter, we introduce a photovoltaic-based self-sufficient energy supply system. The primary objective of this system is to ensure the continuous operation of the remote weather sensing system, even during months with reduced solar radiation, and potentially during extended periods without access to external energy sources. To achieve this, we carefully size the energy reserve components, including the battery and solar panel, in accordance with the specific requirements of the application. Additionally, the dimensions of the solar array are determined based on factors such as orientation and tilt angle. Our goal is to design the system so that it can reliably sustain energy supply during radiation-adverse months without compromising energy supply during other seasons. To inform our design decisions, we make use of open data sources, such as historic local hourly irradiance data from Deutscher Wetterdienst (DWD).

In the fifth chapter, we introduce a semi-autonomous flight assistance system designed to enhance pilot operations. This system provides technical staff at the ground station with the capability to activate or deactivate visual detection and flight control using a remote control interface. It also improves the UAV’s hovering behavior, making it more resilient against wind disturbances.

In Section 5.1, we describe an extrinsic calibration method that transforms the coordinate system of RGB-D cameras without overlapping in the vehicle’s coordinate system. This transformation is essential for later flight control operations.

Additionally, we develop a GPS-based navigation system in Section 5.2 to support long-range operations while incorporating obstacle avoidance functionality. This system provides guidance to the pilot regarding the orientation and distance to the target location.

Section 5.3 outlines an algorithm for detecting and approaching the transmission tower and installation corner leg required for cantilever attachment. This algorithm assists the pilot in recognizing the orientation of the specified mast leg and facilitates target recovery in cases where the target is lost during the translation and rotation of the vehicle. For effective implementation of this algorithm, suitable depth sensors are necessary, and we plan to conduct field tests with appropriate sensor equipment, including extrinsically calibrated cameras and LiDAR. Furthermore, the calibration of the gripper system on the UAV with depth sensors and the vehicle is essential.

In the last section, Section 5.4, we present the detection and flight control approach for reaching the mounting position on the cantilever for the weather station. This approach is field-tested, and it includes methods to avoid losing track of the target.

As discussed, the distribution and maintenance of a sensor network spanning thousands of kilometers along transmission lines pose significant challenges in terms of operational time and the availability of technical staff. The traditional approach can be both time-intensive and insufficient. However, with the adoption of UAV technology, it becomes possible to reduce both the time and human resources required for these tasks, potentially achieving a cost reduction of at least 50%. This is particularly advantageous in locations with difficult accessibility.

In the framework of this dissertation, we have tested the fundamental concepts in both laboratory and field settings. The feasibility of this development has been thoroughly assessed and validated. We anticipate that these innovations will be implemented and realized in the near future, providing valuable support for the grid monitoring system.

List of Figures

List of Tables

List of Publications

Patent contributions

[1] N. Shen, W. Stork, G. Molinar, and M. Gerdes, “Ausleger zur anoednung an einem vertikalen halteprofiel, sowie montage-/demontagevorrichtung und verfahren hierfür,” Germany, Nov. 2022.

Journal articles

[1] S. Tang, Y. Zhu, F. Wang, and N. Shen, “Can marketization improve sustainable development in northeastern china? evidence from the perspective of coupling coordination degree model,” *Discrete Dynamics in Nature and Society*, vol. 2022, 2022.

[2] T. Finkbeiner, C. Manz, M. Raorane, C. Metzger, L. Schmidt-Speicher, N. Shen, R. Ahrens, J. Maisch, P. Nick, and A. Guber, “A modular microfluidic bioreactor to investigate plant cell–cell interactions,” *Protoplasma*, vol. 259, no. 1, pp. 173–186, 2022.

Conference contributions

[1] N. Shen, D. Li, and W. Stork, “3-d shape optimization of a sensor mounting arm using moga and mlf,” in *2020 12th International Conference on Advanced Computational Intelligence (ICACI)*. IEEE, 2020, pp. 602–608.

[2] N. Shen, J. Wu, G. Molinar, and W. Stork, “Data-based analysis of the optimal direction of a photovoltaic system for remote sensor nodes for a case study in germany,” in *2021 5th International Conference on Green Energy and Applications (ICGEA)*. IEEE, 2021, pp. 124–129.

[3] N. Shen, T. Wei, H. Hu, and W. Stork, “Extrinsic calibration of uav and multi rgb-d cameras with non-overlapping by using an external camera,” in *2022 IEEE/SICE International Symposium on System Integration (SII)*, 2022, pp. 232–237.

[4] N. Shen, C. Wencheng, W. Stork, and S. Tang, “Uav flight control algorithm based on detection and pose estimation of the mounting position for weather station on transmission tower using depth camera,” in *2022 IEEE/ 17th IEEE International Conference on Control Automation (IEEE ICCA 2022)*, June 2022.

[5] N. Shen, J. Cao, M. Zipp, and W. Stork, “Autonomous obstacle avoidance for uav based on point cloud,” in *2022 IEEE/ 2022 International Conference on Unmanned Aircraft Systems (ICUAS ’22)*, June 2022.

Bibliography

[1] S. Dröge, *The Paris Agreement 2015: turning point for the international climate regime*, ser. SWP Research Paper. Berlin: Stiftung Wissenschaft und Politik -SWP- Deutsches Institut für Internationale Politik und Sicherheit, 2016, vol. 4/2016.

[2] DW, “Germany closes half its remaining nuclear power plants,” 2021. [Online]. Available: https://www.dw.com/en/germany-closes-half-its-remaining-nuclear-power-plants/a-60302362

[3] Umwelt Bundesamt, “Energy target 2050:100% renewable electricity supply,” 2010. [Online]. Available: https://www.umweltbundesamt.de/sites/default/files/medien/378/publikationen/energieziel_2050_kurz.pdf

[4] G. F. M. for Economic Affairs and Energy(BMWi), “Our energy transition for an energy supply that is secure, clean, and affordable.” [Online]. Available: https://www.bmwi.de/Redaktion/EN/Dossier/energy-transition.html

[5] Germany Federal Ministry for Economic Affairs and Energy(BMWi). What exactly is “grid congestion”? [Online]. Available: https://www.bmwi-energiewende.de/EWD/Redaktion/EN/Newsletter/2018/03/Meldung/direkt-account.html

[6] A. v. S. Anders L. Eriksrud, Julian Hentschel, “Redispatch and Countertrade Costs,” p. 26, January 2020. [Online]. Available: https://thema.no/wp-content/uploads/THEMA-Report-2020-01-Redispatch-and-Countertrade-Costs-Impact-of-Germany-Bidding-Zones-3.pdf

[7] K. Appunn, “Re-dispatch costs in the German power grid,” 16.02.2016. [Online]. Available: https://www.cleanenergywire.org/factsheets/re-dispatch-costs-german-power-grid

[8] B. für Wirtschaft und Klimaschutz(BMWK), “Grid expansion: Grid expansion is an indispensable part of the energy transition.” [Online]. Available: https://www.bmwi.de/Redaktion/EN/Artikel/Energy/electricity-grids-of-the-future-02.html

[9] “Nova-Prinzip - Netzentwicklungsplan,” 2019. [Online]. Available: www.netzentwicklungsplan.de/de/node/489

[10] “NOVA PRINCIPE RESPONSIBILITY IN NETWORK CONSTRUCTION.” [Online]. Available: https://www.transnetbw.com/en/world-of-energy/nova-principle

[11] “Dynamic Line Rating (DLR).” [Online]. Available: https://www.entsoe.eu/Technopedia/techsheets/dynamic-line-rating-dlr

[12] E. J. Adlerman and K. K. Droegemeier, “The sensitivity of numerically simulated cyclic mesocyclogenesis to variations in model physical and computational parameters,” *Monthly weather review*, vol. 130, no. 11, pp. 2671–2691, 2002.

[13] L. R. Bernardet, L. D. Grasso, J. E. Nachamkin, C. A. Finley, and W. R. Cotton, “Simulating convective events using a high-resolution mesoscale model,” *Journal of Geophysical Research: Atmospheres*, vol. 105, no. D11, pp. 14 963–14 982, 2000.

[14] “Regional model ICON-D2.” [Online]. Available: https://www.dwd.de/EN/ourservices/nwp_forecast_data/nwp_forecast_data.html

[15] A. Michiorri, H. M. Nguyen, S. Alessandrini, J. B. Bremnes, S. Dierer, E. Ferrero, B. E. Nygaard, P. Pinson, N. Thomaidis, and S. Uski, “Forecasting for dynamic line rating,” *Renewable and Sustainable Energy Reviews*, no. 52, pp. 1713–1730, 2015.

[16] I. Albizu, E. Fernández, R. Alberdi, M. T. Bedialauneta, and A. J. Mazón, "Adaptive static line rating for systems with htls conductors," *IEEE Transactions on Power Delivery*, vol. 33, no. 6, pp. 2849–2855, 2018.

[17] F. Eriksen, "Costs of stabilising German power grid fall again in 2019." [Online]. Available: cleanenergywire.org/news/costs-stabilising-german-power-grid-fall-again-2019

[18] D. Wetterdienst, "Profile Measurements at Towers and Masts ." [Online]. Available: https://www.dwd.de/EN/research/observing_atmosphere/lindenberg_column/boundery_layer/profilmasten.html

[19] "Wind energy generation systems - part 12-1: Power performance measurements of electricity producing wind turbines," 2017.

[20] K. Shea and I. F. Smith, "Improving full-scale transmission tower design through topology and shape optimization," *Journal of structural engineering*, vol. 132, no. 5, pp. 781–790, 2006.

[21] G. Karadere, Y. Düzcan, and A. R. Yıldız, "Light-weight design of automobile suspension components using topology and shape optimization techniques," *Materials Testing*, vol. 62, no. 5, pp. 454–464, 2020.

[22] R. Yang, "A three-dimensional shape optimization system—shop3d," *Computers & structures*, vol. 31, no. 6, pp. 881–890, 1989.

[23] H. Lian, P. Kerfriden, and S. Bordas, "Shape optimization directly from cad: An isogeometric boundary element approach using t-splines," *Computer Methods in Applied Mechanics and Engineering*, vol. 317, pp. 1–41, 2017.

[24] A. Madrane, H. An, J. Leng, M. Schaenzer, M. Q. Pham, G. Bourgeois, A. Shanian, and D. Pasini, "Shape optimization of inclined hole for enhanced film-cooling performance using discrete adjoint method," *International Journal of Thermal Sciences*, vol. 158, p. 106542, 2020.

[25] W. Chen, Y. Chen, and C. Wang, "Optimization of processing parameters for beam blank continuous casting using moga combined with fem," 2013.

[26] D. Svozil, V. Kvasnicka, and J. Pospichal, "Introduction to multi-layer feed-forward neural networks," *Chemometrics and intelligent laboratory systems*, vol. 39, no. 1, pp. 43–62, 1997.

[27] S. Wang, G. Jian, J. Xiao, J. Wen, and Z. Zhang, "Optimization investigation on configuration parameters of spiral-wound heat exchanger using genetic aggregation response surface and multi-objective genetic algorithm," *Applied Thermal Engineering*, vol. 119, pp. 603–609, 2017.

[28] G. Grebenişan and N. Salem, "The multi-objective genetic algorithm optimization, of a superplastic forming process, using ansys®," in *MATEC Web of Conferences*, vol. 126. EDP Sciences, 2017, p. 03003.

[29] R. K. Rathore, A. Sarda, and R. Chandrakar, "An approach to optimize ann meta model with multi objective genetic algorithm for multi-disciplinary shape optimization," *International Journal of Soft Computing and Engineering (IJSCE) ISSN*, pp. 2231–2307, 2012.

[30] S. Lotfan, R. A. Ghiasi, M. Fallah, and M. Sadeghi, "Ann-based modeling and reducing dual-fuel engine's challenging emissions by multi-objective evolutionary algorithm nsga-ii," *Applied Energy*, vol. 175, pp. 91–99, 2016.

[31] I. o. P. E. KIT Germany, "Lecture: Lightweight engineering design."

[32] M. supermarkets, "7 things to consider when choosing an aluminum grade," January 2015. [Online]. Available: https://www.metalsupermarkets.com/7-things-consider-choosing-aluminum-grade/

[33] Q. Xin, "Durability and reliability in diesel engine system design," *Diesel Engine System Design*, pp. 113–202, 2013.

[34] O. Kayabasi and B. Ekici, "The effects of static, dynamic and fatigue behavior on three-dimensional shape optimization of hip prosthesis by finite element method," *Materials & design*, vol. 28, no. 8, pp. 2269–2277, 2007.

[35] Resnick and Halliday, "Fundamental Relationships," 1968. [Online]. Available: https://web.archive.org/web/20100709205321/http://geophysics.ou.edu/solid_earth/notes/mag_basic/mag_basic.html

[36] T. D. P. SHOP, “DJI MATRICE 600 PRO SPECIFICATIONS.” [Online]. Available: https://www.thedroneproshop.com/blogs/product-info/dji-matrice-600-pro-specifications

[37] U. Guelph, “Torque and Rotational Motion Tutorial.” [Online]. Available: https://www.physics.uoguelph.ca/torque-and-rotational-motion-tutorial

[38] “Friction - friction coefficients and calculator friction theory with calculator and friction coefficients for combinations of materials like ice, aluminum, steel, graphite and many more.” [Online]. Available: https://www.engineeringtoolbox.com/friction-coefficients-d_778.html

[39] S. A. International, “As 4509.2-2002 stand-alone power systems - system design guidelines,” 2002.

[40] S. A. Mousavi Maleki, H. Hizam, and C. Gomes, “Estimation of hourly, daily and monthly global solar radiation on inclined surfaces: Models re-visited,” *Energies*, vol. 10, no. 1, p. 134, 2017.

[41] J. Spencer, “Fourier series reprensentation of the position of the sun,” *Search*, vol. 2, no. 5, p. 172, 1971.

[42] M. Iqbal, *An introduction to solar radiation.* Elsevier, 2012.

[43] E. Tasdemiroglu, “Solar energy utilization technical and economic aspects,” *Ankara, Turkey: Middle East Technical University*, 1988.

[44] C. Demain, M. Journée, and C. Bertrand, “Evaluation of different models to estimate the global solar radiation on inclined surfaces,” *Renewable energy*, vol. 50, pp. 710–721, 2013.

[45] E. COFFARI, “The sun and the celestial vault,” in *Solar energy engineering*. Elsevier, 1977, pp. 5–36.

[46] C. J. Willmott, “On the climatic optimization of the tilt and azimuth of flat-plate solar collectors,” *Solar Energy*, vol. 28, no. 3, pp. 205–216, 1982.

[47] T. M. Klucher, “Evaluation of models to predict insolation on tilted surfaces,” *Solar energy*, vol. 23, no. 2, pp. 111–114, 1979.

[48] C. Gueymard, “An anisotropic solar irradiance model for tilted surfaces and its comparison with selected engineering algorithms,” *Solar energy*, vol. 38, no. 5, pp. 367–386, 1987.

[49] C. A. Gueymard, “Direct and indirect uncertainties in the prediction of tilted irradiance for solar engineering applications,” *Solar Energy*, vol. 83, no. 3, pp. 432–444, 2009.

[50] “Hourly station observations of solar incoming (total/diffuse) and longwave downward radiation for germany.” [Online]. Available: https://opendata.dwd.de/test/CDC/observations_germany/climate/hourly/solar/

[51] F. Zhao, T. Tamaki, T. Kurita, B. Raytchev, and K. Kaneda, “Marker-based non-overlapping camera calibration methods with additional support camera views,” *Image and Vision Computing*, vol. 70, pp. 46–54, 2018.

[52] Y. Xu, F. Gao, Z. Zhang, and X. Jiang, “A calibration method for non-overlapping cameras based on mirrored absolute phase target,” *The International Journal of Advanced Manufacturing Technology*, vol. 104, no. 1, pp. 9–15, 2019.

[53] K. Takahashi and S. Nobuhara, “Structure of multiple mirror system from kaleidoscopic projections of single 3d point,” *IEEE Transactions on Pattern Analysis and Machine Intelligence*, 2021.

[54] I. Van Crombrugge, R. Penne, and S. Vanlanduit, “Extrinsic camera calibration for non-overlapping cameras with gray code projection,” *Optics and Lasers in Engineering*, vol. 134, p. 106305, 2020.

[55] ——, “Extrinsic camera calibration with line-laser projection,” *Sensors*, vol. 21, no. 4, p. 1091, 2021.

[56] G. Carrera, A. Angeli, and A. J. Davison, “Slam-based automatic extrinsic calibration of a multi-camera rig,” in *2011 IEEE International Conference on Robotics and Automation*. IEEE, 2011, pp. 2652–2659.

[57] K. Nishiguchi, H. Uchiyama, K. Hayakawa, J. Adachi, D. Thomas, A. Shimada, and R.-I. Taniguchi, “On-the-fly extrinsic calibration of non-overlapping in-vehicle cameras based on visual slam under 90-degree backing-up parking,” in *2020 IEEE Intelligent Vehicles Symposium (IV)*. IEEE, 2020, pp. 2021–2028.

[58] K. Koide and E. Menegatti, “Non-overlapping rgb-d camera network calibration with monocular visual odometry,” in *2020 IEEE/RSJ International Conference on Intelligent Robots and Systems (IROS)*. IEEE, 2020, pp. 9005–9011.

[59] T. Yang, Q. Zhao, X. Wang, and D. Huang, “Accurate calibration approach for non-overlapping multi-camera system,” *Optics & Laser Technology*, vol. 110, pp. 78–86, 2019.

[60] B. Triggs, P. F. McLauchlan, R. I. Hartley, and A. W. Fitzgibbon, “Bundle adjustment—a modern synthesis,” in *International workshop on vision algorithms*. Springer, 1999, pp. 298–372.

[61] K. Ni, D. Steedly, and F. Dellaert, “Out-of-core bundle adjustment for large-scale 3d reconstruction,” in *2007 IEEE 11th International Conference on Computer Vision*. IEEE, 2007, pp. 1–8.

[62] intel REALSENSEh, “Depth camera D415.” [Online]. Available: https://www.intelrealsense.com/

[63] Z. Zhang, M. Xiong, and H. Xiong, “Monocular depth estimation for uav obstacle avoidance,” in *2019 4th International Conference on Cloud Computing and Internet of Things (CCIOT)*. IEEE, 2019, pp. 43–47.

[64] H. Lee, H. Ho, and Y. Zhou, “Deep learning-based monocular obstacle avoidance for unmanned aerial vehicle navigation in tree plantations,” *Journal of Intelligent & Robotic Systems*, vol. 101, no. 1, pp. 1–18, 2021.

[65] L. Matthies, R. Brockers, Y. Kuwata, and S. Weiss, “Stereo vision-based obstacle avoidance for micro air vehicles using disparity space,” in *2014 IEEE*

international conference on robotics and automation (ICRA). IEEE, 2014, pp. 3242–3249.

[66] S. Ren, K. He, R. Girshick, and J. Sun, “Faster r-cnn: Towards real-time object detection with region proposal networks,” *Advances in neural information processing systems*, vol. 28, 2015.

[67] D. S. Levkovits-Scherer, I. Cruz-Vega, and J. Martinez-Carranza, “Real-time monocular vision-based uav obstacle detection and collision avoidance in gps-denied outdoor environments using cnn mobilenet-ssd,” in *Mexican International Conference on Artificial Intelligence*. Springer, 2019, pp. 613–621.

[68] A. Al-Kaff, F. García, D. Martín, A. De La Escalera, and J. M. Armingol, “Obstacle detection and avoidance system based on monocular camera and size expansion algorithm for uavs,” *Sensors*, vol. 17, no. 5, p. 1061, 2017.

[69] H. Yu, F. Zhang, P. Huang, C. Wang, and L. Yuanhao, “Autonomous obstacle avoidance for uav based on fusion of radar and monocular camera,” in *2020 IEEE/RSJ International Conference on Intelligent Robots and Systems (IROS)*. IEEE, 2020, pp. 5954–5961.

[70] F. Azevedo, J. S. Cardoso, A. Ferreira, T. Fernandes, M. Moreira, and L. Campos, “Efficient reactive obstacle avoidance using spirals for escape,” *Drones*, vol. 5, no. 2, p. 51, 2021.

[71] X. Li, S. Du, G. Li, and H. Li, “Integrate point-cloud segmentation with 3d lidar scan-matching for mobile robot localization and mapping,” *Sensors*, vol. 20, no. 1, p. 237, 2019.

[72] J. N. Yasin, M.-H. Haghbayan, J. Heikkonen, H. Tenhunen, and J. Plosila, “Formation maintenance and collision avoidance in a swarm of drones,” in *Proceedings of the 2019 3rd International Symposium on Computer Science and Intelligent Control*, 2019, pp. 1–6.

[73] F. Azevedo, A. Oliveira, A. Dias, J. Almeida, M. Moreira, T. Santos, A. Ferreira, A. Martins, and E. Silva, “Collision avoidance for safe structure inspection with multirotor uav,” in *2017 European Conference on Mobile Robots (ECMR)*. IEEE, 2017, pp. 1–7.

[74] S. Koenig and M. Likhachev, “Fast replanning for navigation in unknown terrain,” *IEEE Transactions on Robotics*, vol. 21, no. 3, pp. 354–363, 2005.

[75] J. J. Kuffner and S. M. LaValle, “Rrt-connect: An efficient approach to single-query path planning,” in *Proceedings 2000 ICRA. Millennium Conference. IEEE International Conference on Robotics and Automation. Symposia Proceedings (Cat. No. 00CH37065)*, vol. 2. IEEE, 2000, pp. 995–1001.

[76] M. A. Fischler and R. C. Bolles, “Random sample consensus: a paradigm for model fitting with applications to image analysis and automated cartography,” *Communications of the ACM*, vol. 24, no. 6, pp. 381–395, 1981.

[77] J. L. Bentley, “Multidimensional binary search trees used for associative searching,” *Commun. ACM*, p. 509–517, sep 1975. [Online]. Available: https://doi.org/10.1145/361002.361007

[78] R. B. Rusu, “Semantic 3d object maps for everyday manipulation in human living environments,” *KI-Künstliche Intelligenz*, vol. 24, no. 4, pp. 345–348, 2010.

[79] “Flexible Collision Library/FCL.” [Online]. Available: https://github.com/flexible-collision-library/fcl

[80] R. O. Duda and P. E. Hart, “Use of the hough transformation to detect lines and curves in pictures,” *Communications of the ACM*, vol. 15, no. 1, pp. 11–15, 1972.

[81] R. G. Von Gioi, J. Jakubowicz, J.-M. Morel, and G. Randall, “Lsd: A fast line segment detector with a false detection control,” *IEEE transactions on pattern analysis and machine intelligence*, vol. 32, no. 4, pp. 722–732, 2008.

[82] J. H. Lee, S. Lee, G. Zhang, J. Lim, W. K. Chung, and I. H. Suh, “Outdoor place recognition in urban environments using straight lines,” in *2014 IEEE International Conference on Robotics and Automation (ICRA)*. IEEE, 2014, pp. 5550–5557.

[83] D. G. Lowe, “Distinctive image features from scale-invariant keypoints,” *International journal of computer vision*, vol. 60, no. 2, pp. 91–110, 2004.

[84] H. Bay, T. Tuytelaars, and L. V. Gool, “Surf: Speeded up robust features,” in *European conference on computer vision*. Springer, 2006, pp. 404–417.

[85] E. Rublee, V. Rabaud, K. Konolige, and G. Bradski, “Orb: An efficient alternative to sift or surf,” in *2011 International conference on computer vision*. Ieee, 2011, pp. 2564–2571.

[86] Q.-V. Tran, S.-F. Su, V.-T. Nguyen, V. N. Truong, and M.-C. Chen, “Real-time object recognition and camera pose estimation.”

[87] W. Liu, D. Anguelov, D. Erhan, C. Szegedy, S. Reed, C.-Y. Fu, and A. C. Berg, “Ssd: Single shot multibox detector,” in *European conference on computer vision*. Springer, 2016, pp. 21–37.

[88] J. Redmon, S. Divvala, R. Girshick, and A. Farhadi, “You only look once: Unified, real-time object detection,” in *Proceedings of the IEEE conference on computer vision and pattern recognition*, 2016, pp. 779–788.

[89] M. Liang, B. Yang, Y. Chen, R. Hu, and R. Urtasun, “Multi-task multi-sensor fusion for 3d object detection,” in *Proceedings of the IEEE/CVF Conference on Computer Vision and Pattern Recognition*, 2019, pp. 7345–7353.

[90] C. R. Qi, O. Litany, K. He, and L. J. Guibas, “Deep hough voting for 3d object detection in point clouds,” in *proceedings of the IEEE/CVF International Conference on Computer Vision*, 2019, pp. 9277–9286.

[91] W. Shi and R. Rajkumar, “Point-gnn: Graph neural network for 3d object detection in a point cloud,” in *Proceedings of the IEEE/CVF conference on computer vision and pattern recognition*, 2020, pp. 1711–1719.

[92] “Carbon Dioxide Emissions From Electricity.” [Online]. Available: https://www.world-nuclear.org/information-library/energy-and-the-environment/carbon-dioxide-emissions-from-electricity.aspx